

Ordered Micro-/Nanostructure Based Humidity Sensor for Fuel Cell Application

by

Yun Wang

A thesis
presented to the University of Waterloo
in fulfillment of the
thesis requirement for the degree of
Doctor of Philosophy
in
Systems Design Engineering

Waterloo, Ontario, Canada, 2010

© Yun Wang 2010

I hereby declare that I am the sole author of this thesis. This is a true copy of the thesis, including any required final revisions, as accepted by my examiners.

I understand that my thesis may be made electronically available to the public.

Abstract

Humidity sensors are one of the most widely used sensors in commercial and industrial applications for environmental monitoring and controlling. Although related technology have been studied intensively, humidity sensing in harsh environments still remains a challenge. The inability of current humidity sensors to operate in high temperature environments is generally due to the degradation of the sensing films caused by high temperature, high humidity level, and/or contaminations. Our goal is the design and fabrication of a humidity sensor that is capable of working under high temperatures and in a condensing environment. The targeted application of this sensor is in the polymer electrolyte membrane (PEM) fuel cell, where humidity control is crucial for performance optimization.

In this work, ordered macroporous silicon is thoroughly studied as a humidity sensing layer. In addition to the advantages of traditional porous silicon for gas sensing (high resistance to high temperature and good compatibility with current IC fabrication process), the ordered macroporous silicon used in these experiment has uniform pore size, pore shape and distribution. All the vertical aligned pores can be opened to the environment at both ends, which can significantly increase the efficiency of gas diffusion and adsorption. Moreover, this special structure opens the door to uniform surface modifications for sensing enhancement.

Both ordered macroporous silicon based heterostructure and self-supporting membrane are fabricated and investigated as a humidity sensor. Heterostructure sensors with different thin film surface coatings including bare Si, thermally grown SiO_2 , atom layer deposited ZnO, HfO_2 , and Ta_2O_5 are characterized. Post micro-fabrication is achieved on this ordered porous structure without affecting the material and its sensing properties. It has been proven that the ordered macroporous silicon with Ta_2O_5 surface coating shows the best

sensing property due to its ultra-hydrophilic surface. The sensor shows high sensitivity, fast response times, small hysteresis, and extraordinary stability and repeatability under high temperatures and in condensing environment. It demonstrates great potential and advantages over existing commercial humidity sensors in the fuel cell application field.

In addition to ordered macroporous silicon, well aligned 1D ZnO nanorods/nanowires -another widely used nanostructure in gas sensing- is also investigated as humidity sensing materials. Both vertically and laterally aligned nanorods/nanowires are fabricated and tested against humidity changes. The sensors shows increasing resistance to increasing relative humidity, which is contrary to most published works so far. Possible mechanisms have been proposed in this thesis and future work has been suggested for further study.

To the best of our knowledge, this work is first to use ordered macroporous silicon and well aligned 1D ZnO nanorods/nanowires for humidity sensing.

Acknowledgements

I owe my biggest thanks to my thesis supervisor Professor John T.W. Yeow, who gave me the opportunity to pursue my Ph.D degree in this beautiful country and exciting lab. I have learned a great deal from him. Even in his busiest time, he tries his best to help and answer the questions I have. He always provided me valuable suggestions and kept the development of the project on the right track. He is open-minded and encourages any new ideas. I would like to thank him for all his encouragement and support throughout my Ph.D study with him.

I am in debt to Andreas Langner and Professor Frank Müller from Max Planck Institute for their huge contributions to this project. Without their support, this project could not be accomplished. All their help and advice are extremely appreciated. My thanks also go to Professor Liang-Yih Chen from National Taiwan University of Science and Technology for his collaboration and valuable advice. It has been a great pleasure working with him.

I would like to thank all my thesis committee members Professor Eihab Abdel-Rahman, Professor Maud Gorbet, Professor Xianguo Li, and Professor Freddy Kleitz for being my committee and for giving me valuable directions and suggestions.

My thanks also go to my master supervisor Dong Xu and Bingchu Cai for their continuous support on my Ph.D work, and all the technicians at the Research Institute of Micro/Nano Science and Technology at Shanghai Jiao Tong University for their help during my fabrication work there. I would like to thank Henry Lee and Yimin Zhou from the Emerging Communications Technology Institute at University of Toronto for all of their help and valuable discussions they have provided.

I also owe my thanks to all of my lab mates and friends for sharing all these years with

me. I am sorry that there are too many to list all but you are all on the list. I had a great time working and having fun together with them. Special thanks go to Seungwoo Park, who has been very helpful to me on this project, and Jiazhi Ma who has been sharing all the joys and tears with me.

I would like to acknowledge the service and help provided by all the staffs in the Department of Systems Design Engineering and University of Waterloo. I had a wonderful and memorable time here. I enjoyed the campus life very much and I think our staff are always trying their best to help the students.

My special thanks go to my parents, who has been loving me and supporting me with all their heart and soul for so many years. It was their wisdom, love and faith in me that made me the person I am today. I am so grateful and fortunate to have them behind me, letting me be myself and follow my dreams. I am deeply in debt to their love and will love them the same way all through my life.

Finally, I would like to thank my significant other Brien for always being there for me. It was him accompanying me through out this long journey. His love made me stronger and his warm smile lit up the dim days for me. He always had his faith in me and encouraged me to keep going forward. He was always the first one to read and edit my papers. And he was always the first one to celebrate any of my accomplishments. He was my first audience in any presentation and the one who drove me around when I was stressed. He was great contribution to this thesis. Life without him would never be this colorful and full of laughter.

Dedication

To my parents and my beloved Brien.

Contents

List of Tables	xi
List of Figures	xv
1 Introduction	1
1.1 Fuel cells and water management in fuel cells	4
1.1.1 Working principle of fuel cells	4
1.1.2 Classification of fuel cell	5
1.1.3 Water management in PEMFCs	7
1.2 Gas adsorption on solid surface	9
1.2.1 Physical adsorption	10
1.2.2 Chemical adsorption	10
1.2.3 Capillary condensation	11
1.3 Humidity sensing technology	12
1.3.1 Humidity sensing material	13
1.3.2 Transduction technique of humidity sensors	15
1.4 Humidity sensor with ordered porous structures	18
2 Porous Silicon	21
2.1 Formation of porous silicon	21
2.2 Property and application of porous silicon	22
2.2.1 Electrical property of porous silicon	22

2.2.2	Photoluminescence of porous silicon	23
2.2.3	Application of porous silicon	23
2.3	Porous silicon based gas/humidity sensor	24
2.4	Ordered macroporous silicon	27
3	Ordered Macroporous Silicon with and without Thin Film Surface Coating for Humidity Sensing	30
3.1	Fabrication of the ordered macroporous silicon	31
3.2	Measurement setup	33
3.2.1	Experiment setup	33
3.2.2	Humidity generation and measurement at high temperature	35
3.3	Ordered macroporous silicon without surface coating	36
3.3.1	Testing structure and terminology	36
3.3.2	Resistance response of ordered macroporous silicon without surface coating	39
3.4	Surface modification of ordered macroporous silicon	42
3.5	Humidity sensor with HfO ₂ modified ordered macroporous silicon	44
3.5.1	Resistance response of HfO ₂ modified ordered macroporous silicon	44
3.5.2	Capacitive response of HfO ₂ modified ordered macroporous silicon	46
3.6	Conclusion	48
4	Humidity Sensor Based on Ordered Macroporous Silicon with Ta₂O₅ Thin Film Coating	50
4.1	Sensor fabrication	50
4.2	Humidity sensing at room temperature	53
4.2.1	Sensitivity	53
4.2.2	Response time	55
4.2.3	High humidity level and flooding sensing	62
4.2.4	Stability and hysteresis	63
4.3	High temperature sensing	64
4.4	Discussions	66

4.4.1	The sensing mechanisms	66
4.4.2	Parasitic resistance and capacitance	69
4.4.3	Sensing enhancement by thin film coating	71
4.5	Conclusions	72
5	Vertically Aligned ZnO Nanorods for Humidity Sensing	74
5.1	Introduction	75
5.1.1	Synthesis methods of aligned nanostructures	76
5.1.2	Gas sensing mechanisms with metal oxide nanostructures	78
5.2	Synthesis of ZnO nanorods	79
5.3	Characterization of the ZnO nanorods	81
5.4	Humidity sensing results and discussions	84
5.5	Conclusions	92
6	Laterally Aligned ZnO Nanowires for Humidity Sensing	93
6.1	Fabrication of the sensor	93
6.2	Humidity sensing characterization	96
6.3	Discussions	99
6.4	Conclusions	106
7	Contributions and Future work	108
7.1	Contributions	108
7.2	Future work	111
7.2.1	Ordered macroporous silicon humidity sensor	111
7.2.2	Aligned ZnO nanowires for humidity sensing	114
	Permissions	116
	Bibliography	137

List of Tables

1.1	Classification of fuel cells	6
3.1	Pore parameters of three different macroporous silicon heterostructure samples.	43
4.1	Comparison of the water contact angle and <i>PCV</i> (%) of ordered macroporous silicon humidity sensor with different surface coatings.	72
5.1	ZnO nanorods samples prepared with varying the growing parameters	80
6.1	Comparison Table	101

List of Figures

1.1	A typical fuel cell configuration [7]	5
1.2	Schematic of a PEMFC and its operating process	7
1.3	Electrodes geometry for capacitive humidity sensors [5]	16
1.4	(a) TEM image of calcined-SBA-16 view from [111] direction [35]; (b) SEM images of pure MCM-41 [36]; (c) an array of approximately 100 nm porous anodic alumina (PAA) channels perfectly organized in a hexagonal arrangement; (d) PAA channels with square arrangement [37]; (e) SEM image of anodic aluminum oxide (AAO) with electrode layer on top [38]; (f) SEM images of the ordered high areas ratio silicon microchannel plate (MCP) [39].	19
2.1	Dynamic response of PS gas sensor of different porosities to NO ₂ at room temperature and 20% RH; the insert shows the sensor structure [44]	24
2.2	(a) A PS based FET sensor for isopropanol sensing [45]; (b) A PS capacitor with sandwich structure for acetone and ethanol sensing [46].	25
2.3	(a) Capacitance and (b) resistance of a TCPS humidity sensor as a function of relative humidity at three different temperatures. Measurements were done using 120 Hz frequency [52].	26
2.4	(a) Schematic of the sensor structure; (b) Sensitivity of the sensor in combination with the electronics [53].	27
2.5	SEM micrograph of an ordered macroporous array etched on n-type silicon; the insert is a square pattern of pits produced by standard lithography [53].	28
3.1	Schematic diagram of etching setup	32
3.2	(a) Profile SEM image of a 3D ordered macroporous silicon with square pores; (b) A SEM image of the backside of a self-supporting membrane with ordered structures.	33

3.3	(a) A schematic, and (b) a picture of the experiment setup; the insert is a picture of the testing chamber.	34
3.4	Saturation water vapor pressure as a function of temperature [60].	36
3.5	Grosvenor psychrometric chart (medium temperature) for the air-water system at standard atmospheric pressure [19]	37
3.6	Schematic diagram of testing structure for ordered macroporous silicon heterostructure and self-supporting membrane: side view and top view	37
3.7	<i>PRV</i> -RH curves of the heterostructure and self-supporting membrane. . .	40
3.8	Repeatability test between dry air and saturated air, each step is maintained for 10-12 minutes: (a) heterostructure; (b) self-supporting membrane. . . .	41
3.9	Resistance sensing characteristic of HfO ₂ modified heterostructure : (a) T200; (b) S100, S200 and T200.	44
3.10	Dynamic response of T200 between dry air and saturated air	45
3.11	(a) Capacitance sensitivity characteristic of S100 (100 μ m pore length) and S200 (200 μ m pore length); (b) Linear fit of <i>PCV</i> -RH curve of S200.	47
3.12	Dynamic response of S200 between dry air and saturated air.	47
3.13	Comparison of response time to RH change between S100 and reference sensor: (a) increase of RH, (b) decrease of RH.	48
4.1	(a) SEM image of an ordered macroporous silicon with square pores (4 μ m in diameter), the insert is a SEM image of the 3D structure on silicon substrate (with 97 μ m pore length); (b) A microscope image of the Al electrodes on top of the macroporous silicon; the insert (up-left) is a view of the interdigitated electrodes of the sensor; the insert (lower-right) is a image of the fabricated sensor.	51
4.2	Comparison of the PR thickness-spin rate curves of AZP4330 on different surfaces, the data for smooth surface is from the product data sheet.	52
4.3	Comparison of the porous area coverage by PR under different spin rate: (a) partially covered surface, (b) fully covered surface.	53
4.4	(a) <i>PCV</i> -RH curve and (b) C-RH curve at different measurement frequencies.	54
4.5	(a) Dynamic capacitance response between extra dry and saturated air at different test frequencies, (b) Normalized dynamic capacitance response between extra dry and saturated air at different test frequencies.	56

4.6	(a) Normalized dynamic impedance response between extra dry and saturated air at different measuring frequencies. (b) Normalized dynamic capacitance response between extra dry and saturated air at different test frequencies (sensor with 1 μm pore size).	58
4.7	Capacitance response at different measurement voltage (1 V, 50 mV and 250 mV) at 1 kHz.	59
4.8	(a) Dynamic capacitive response to RH changes between 0% and 38%, (b) dynamic capacitive response to RH changes between 0% and 73%.	59
4.9	(a) Dynamic response of the sensor to different RH% levels at 200 kHz; (b)Corresponding dyanmic response of the reference sensor; (c) the relationship of the response time from 0% to certain RH level to <i>PCV</i> under 200 kHz.	61
4.10	(a) The C-RH curve between 80%-100% RH at 200 kHz; (b) Dynamic response of the sensor to flooding condition.	62
4.11	(a) The capacitance-RH curve with step up and step down RH changes at 200 kHz; (b) The capacitance-RH curve with step up and step down RH changes at 100 Hz, 1 kHz and 100 kHz.	64
4.12	The sensor's capacitance dependency on temperature at 0% RH at 200 kHz.	65
4.13	(a) Capacitance-RH curve at 40 °C, 60 °C, 80 °C at 200 kHz; (b) <i>PCV</i> -RH curve at 40 °C, 60 °C, 80 °C at 200 kHz.	65
4.14	The structure of ordered macroporous silicon with metal oxides thin film coating on the surface.	66
4.15	(a) Impedance-RH curve at different testing frequency at 1 V; (b) Resistance-RH curve of both 4 μm and 1 μm pore size sensor at 1 V DC.	70
4.16	Measurement of water contact angle of (a) Ta_2O_5 thin film coated silicon surface, (b) bare silicon surface. The measurement is taken at non-porous area of the sensors in a 3D micro-stage system with horizontally aligned microscope	71
5.1	ZnO seed layer deposited on ITO/glass substrate with (a) dense surface morphology, and (b) cracked surface morphology. The cracked surface was caused by rapidly temperature ramp in anneal process.	81
5.2	X-ray diffraction spectroscopy of the ZnO nanorods that are grown on an annealed seed layer substrate	82
5.3	SEM images of prepared ZnO nanorods, (a) and (b) sample 1; (c) sample 2; (d) sample 3; (e) and (f) sample 4; (g) and (h) sample 5; (i) and (j) sample 6 e	83

5.4	Comparison of the different samples' resistance variation between 0% and 100% RH (the results are from fresh samples in the first round test of each sample)	85
5.5	Resistance variation-RH of sample 1 at first several round of test	86
5.6	(a) the Resistance-RH curve of sample 1 for several rounds of test, (b) the corresponding <i>PRV</i> -RH curve.	87
5.7	(Dynamic resistance response to change RH of sample 1's for test in different days, (a) day 1, (b) day 2.	88
5.8	The percentage resistance variation degradation over time of three units from sample 6	90
5.9	Dynamic response of Sample 6 (#3) to RH change cycles between 0% and 100%	91
5.10	Comparison of the response time of sample 6 - #3 with the reference humidity sensor	91
6.1	(a)-(b) tile-view and cross-sectional images of ZnO nanowires grown on ITO substrates with a seed layer; ZnO nanowires assembled via DEP force with (c)f=100kHz and $V_{p-p} = 8V$, and (d) f=1 MHz and $V_{p-p} = 8V$ in pure ethanol with 10 drops; (e)f=100kHz and $V_{p-p} = 8V$, and (f) f=1 MHz and $V_{p-p} = 8V$ in ethanol and water mixture with 50 drops. (Scale bars: (a)-(d), 10 μm ; insets of (c)-(f), 200 nm).	95
6.2	A picture of the as fabricated humidity sensor.	96
6.3	Resistance-RH curves with increasing and decreasing RH steps.	97
6.4	(a) Response time of the sensor at both increasing and decreasing RH ; (b) Dynamic response of the resistance of sensor to cycling changing RH between extra dry air and saturated air.	98
6.5	Insertion mechanism of oxygen atoms on the surface and inside the lattice of a MO_{1-x} type oxide	103
6.6	A simple picture showing the influence of absorption water and oxygen molecules on the surface of ZnO nanowires.	106
7.1	Preferable locations of humidity sensors in a single PEMFC.	112

Chapter 1

Introduction

The growing awareness of global environment issue has promoted the search for new and environmental friendly energy sources worldwide. Fuel cells are one of the most promising alternatives to standard energy source. As a result, fuel cells have been intensively studied and developed, especially on their application for transportation and portable power. The advantages of fuel cells include their high efficiency, virtually pollution free and quiet operation. The working principle of fuel cells is an electrochemically reaction combining fuel (hydrogen) and oxidant (oxygen) gases through electrodes in an ion conducting electrolyte [1]. In addition to electricity, water and heat are byproducts of this reaction, which raises the issue of water management in fuel cells, especially for polymer electrolyte membrane fuel cells (PEMFCs). PEMFCs efficiency is highly dependent on the operating conditions, including temperature, humidity and air flow rate. To obtain the optimal performance and minimize losses, the parameter identification, monitoring, and controlling play an important role in the design and operation of fuel cell systems. Therefore, a great deal of research has been devoted to the water management problem of PEMFCs. How-

ever, most of the research have been on modeling, simulation and parameter estimation based on computing [2, 3, 4]. The development of micro- or nano-technology provides the opportunity to integrate a micro humidity sensing system into the fuel cell stack for real-time monitoring and controlling of the system without affecting the operation.

Humidity sensors have widespread applications in many areas -such as the food processing, semiconductor, and pharmaceutical industries- where humidity is monitored and controlled to ensure product quality. The use of humidity sensors in the commercial and domestic sectors is also very important. For example preventing expensive equipment in extreme humidity conditions from damages and malfunctions or monitoring indoor air quality to ensure human comfort.

With the development of micro/nanostructured materials and fabrication technology, the miniaturization of sensing elements has been the main focus of related research, especially the integration of multi-functional elements on one chip with signal conditioning circuits. Generally, the requirements that humidity sensors should meet for a wide range of application are: (i) good sensitivity and accuracy over a wide range of temperature and humidity; (ii) good repeatability and low hysteresis; (iii) fast response and recovery time; (iv) resistance to contaminants and long-term stability; (v) selectivity to other gas molecules; and (vi) cost effectiveness. The presence of these characteristics is particularly important for industrial monitoring and controlling.

Commonly used humidity sensing materials include moisture absorbing polymers, polyimide, poly-electrolytes, porous ceramic (metal oxides), and porous silicon/polysilicon/silica [5]. The mechanism of humidity sensors are based on water vapor adsorption on the sensing films, which causes a detectable property change of the material. Various techniques such as capacitance, resistance, mass and optical sensing has been developed for humidity sen-

sors [6].

So far, water vapor sensing polymers are the most widely used material in commercial humidity sensors. However, the primary problem with polymer sensors is their inability to work in high humidity level (condensing environment) and high temperature conditions. Sintered ceramic is another common humidity sensing material which generally requires thermal energy to regenerate the sensing film due to chemisorption of the water molecules (chemical reaction of water vapor with the metal oxides). Porous silicon (PS) has drawn considerable interest as a potential gas/vapor sensing material due to its large surface area and ultra high surface-to-volume ratio. Their porous structure is ideal for gas molecule diffusion and adsorption to the sensing surface. In addition, its stability at high temperatures and compatibility with conventional IC fabrication processes make it a promising material to build a smart sensor. As such, the sensing properties of PS to various gases/vapors including organic vapor, pollution gas and humidity have been widely investigated by different groups.

The motivation of this work is to design and fabricate a micro humidity sensor that can be integrated into the PEMFC to monitor the inside humidity. To date, most of PEMFCs work at near 100% relative humidity (RH) level and 60 – 90 °C. Therefore, it is important to use a sensing material that has good resistance to condensing environments under long-term operation. Based on the literature review of different materials, ordered macroporous silicon is selected as the humidity sensing layer. In addition to the advantages of PS for gas sensing (high resistance to high temperature and good compatibility with current IC fabrication process), the ordered macroporous silicon used in this experiment has uniform pore size, pore shape and distribution. All the vertical aligned pores can be opened to the environment at both ends, which can increase the efficiency of gas diffusion

and adsorption. In addition, surface modification can be achieved with this structure. This is the first time that ordered macroporous silicon is studied for its humidity sensing property and applications in fuel cell stacks.

In this Chapter, a background introduction of this research is presented. First, the motivation for research on fuel cells and the water management problem within PEMFC stacks is addressed. Secondly, the mechanism of gas molecule adsorption on solid surface is reviewed. Lastly, the state-of-art humidity sensor technology, including sensing materials and commonly used sensor architectures are introduced.

1.1 Fuel cells and water management in fuel cells

1.1.1 Working principle of fuel cells

A fuel cell is an energy conversion device that generates electricity and heat by electrochemically combining a gaseous fuel (hydrogen) and an oxidant gas (oxygen from the air) through electrodes and across an ion conducting electrolyte. During this process, water is formed at the exhaust.

Generally, a fuel cell consists of two electrodes sandwiched around an electrolyte. Hydrogen fuel is fed into the anode of the fuel cell and oxygen, from the air, enters the cell through the cathode. The hydrogen, under the action of the catalyst, splits into protons (hydrogen ions) and electrons, which take different paths towards the cathode. The proton passes through the electrolyte and the electron create a separate current that can be used before reaching the cathode to be reunited with the hydrogen and oxygen, forming a pure water molecule and heat, as shown in the Figure 1.1. The catalyst is usually coated on the

anode and cathode. It can be a platinum coating as in PEMFC or nickel and oxide for the solid oxide fuel cells. The chemical reactions at anode and cathode are as follows:

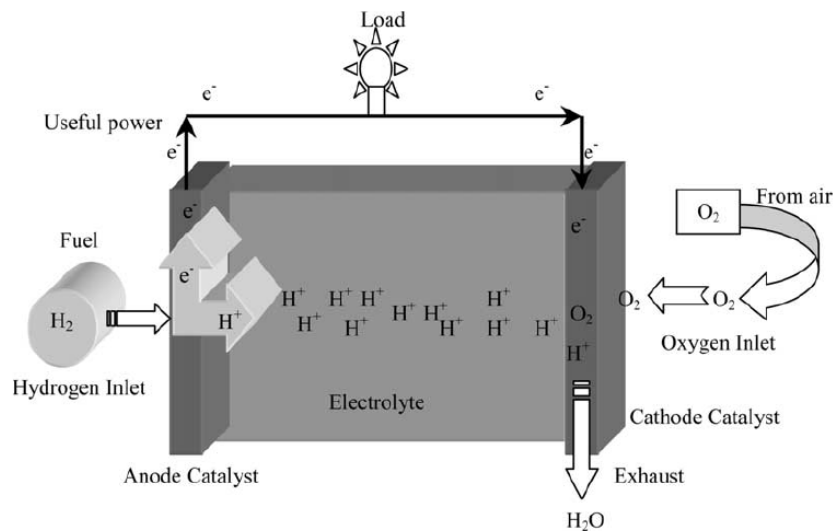
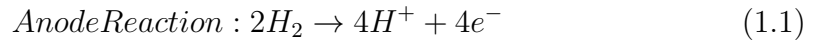


Figure 1.1: A typical fuel cell configuration [7]

1.1.2 Classification of fuel cell

The fuel cells are sorted by their operating temperature and their classification is generally done according to the nature of the electrolyte used [7]. There are several types of fuel cell technologies being developed for different applications, each having their own advantages and disadvantages. Table 1.1 lists several types of fuel cells. By far, the greatest research interest throughout the world has focused on polymer electrolyte (or proton-exchange)

membrane (PEM) fuel cells, which have the biggest potential for cars and mass transportation applications if they can be made cost competitive.

Table 1.1: Classification of fuel cells

Types	Electrolyte	Operating T(°C)	Advantages
Polymer electrolyte membrane (PEMFC)	Polymer, proton exchange membrane	60-90	High power density, rapid startup and small size
Solid oxide (SOFC)	Stabilised zirconia and doped perovskite	600-1000	High power density and potential for internal fuel processing
Alkaline (AFC)	Potassium hydroxide (KOH)	60-200	Reliable and high power output
Phosphoric acid (PAFC)	Phosphoric acid	160-210	Most developed system for terrestrial applications
Direct methanol (DMFC)	Methanol	60-200	Simple storage and fabrication
Molten carbonate (MCFC)	Molten salt	630-650	Intrinsically efficient and CO insensitive

1.1.3 Water management in PEMFCs

A single PEMFC consists of a membrane electrode assembly (MEA), flow field plates, current collectors and end plates. The MEA is a proton conducting membrane sandwiched between two electrodes. The electrodes are made of two gas diffusion layers (GDL) with a layer of platinum catalysts on the surface adjacent to the polymer electrolyte membrane. The GDLs ensure effective diffusion of the reactant gases to the catalyst layer. The flow field plates have flow channels that guide the reactant gases throughout the whole active area [8, 9]. Figure 1.2 shows a schematic of a single PEMFC and the processes happening during the operation [10].

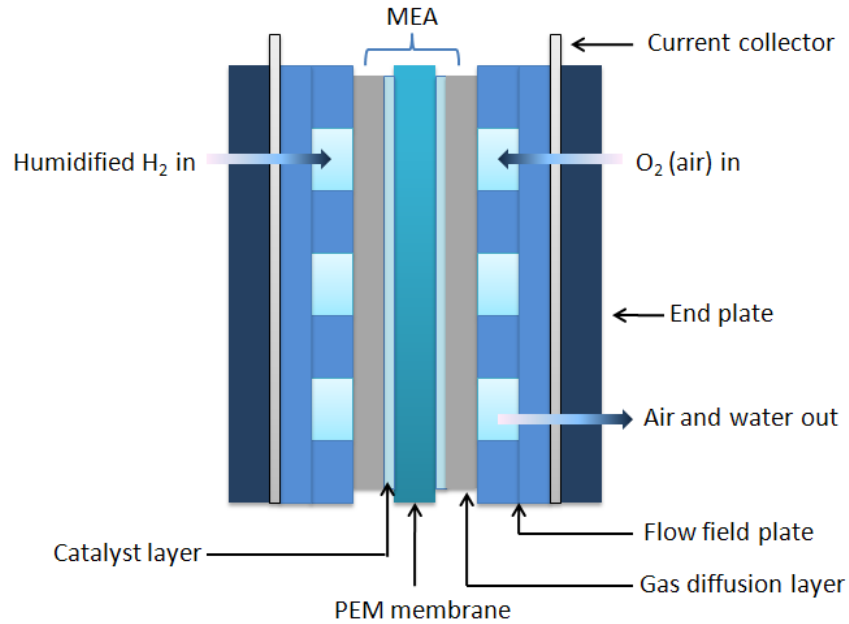


Figure 1.2: Schematic of a PEMFC and its operating process

The water management problem rises from the nature of the PEM, the GDL and the catalyst layer (CL) [11, 12]. The proton conductive membrane is essentially a solidified polymer matrix backbone with sulfonic acid groups attached to it. The membrane is elec-

tronic insulating and has very low gas permeabilities. However, it has excellent hydrogen ion conductivity via the dissociation of the sulfonic acid in the presence of water. Dehydration of the membrane will decrease the membrane's proton conductivity, leading to a decrease in net power and local hot spots [13]. Severe drying can also result in irreversible membrane degradation. Therefore, a high water content in the electrolyte membrane has to be maintained to achieve maximum performance and extended life. Generally, both of the hydrogen and oxygen (air) are highly humidified before entering the cell.

On the other hand, the water produced at the cathode CL must be transported away immediately through the GDL and into the flow field channel, and then exhausted out of the system. Otherwise, the accumulation of the excess water can block the flow channel and the pores of the CL and GDL. This will prevent the fuel and oxygen transportation, thus reducing the catalyst active sites. This is called "flooding" and can significantly decrease the efficiency of the PEMFCs. Therefore, the fuel cell must be operated under a certain condition where water removal is well balanced with water supply to maintain the saturation of the PEM and prevent flooding. This is referred to as water management and is fairly complex. The main function is to maintain a water balance and achieve desired humidity conditions inside the fuel cell stack. It involves the dynamic control of the temperature, gas flow rate, and water removal rate to match the varying operating condition within the fuel cell.

There are several approaches to study the water distribution and water management in PEMFCs. One is the visualization of liquid water distributions under different operating conditions by various imaging techniques. However, this technique is only limited to laboratory study rather than real world application due to the requirement of external and expensive imaging systems. There are also numerous studies devoted to developing

theoretical models to describe the water transportation and water management in PEM-FCs. Various flow field plates designs have also been studied for optimization of water and gas transportation. However, none of the above can achieve real time monitoring and controlling of the fuel cell's operating condition.

So far, there have been very few attempts at integrating humidity sensors into the fuel cell stack. The difficulty is not only caused by the structure and dimension of the fuel cell where there is limited space for sensor installation, but also due to the lack of miniaturized humidity sensors that can operate under high temperatures and saturation (even flooding) environments without degradation. This is the motivation for our research in the design and fabrication of an advanced humidity sensor to overcome this challenge.

1.2 Gas adsorption on solid surface

For most gas/vapor sensors, the sensing mechanism is generally related to the gas/vapor molecule adsorption and interaction with the sensing layer's surface. When a gas (or adsorbate) is allowed to come to equilibrium with a solid or liquid (or adsorbent) surface, the concentration of gas molecules is always greater in the immediate vicinity of the surface than in the free gas phase, regardless of the nature of the gas or surface. The process by which this surface excess is formed is termed adsorption [14]. Adsorption processes are generally classified as physical or chemical, depending on the nature of the interaction forces involved.

1.2.1 Physical adsorption

Physical adsorption, also termed as van der Waals adsorption, is caused by molecular interaction forces. It is a general phenomenon that occurs in any gas-solid system under suitable conditions of temperature and pressure. The formation of physically adsorbed layers having several molecular diameters in thickness is frequently found. These layers behave in many respects like two-dimensional liquids. The heat of physical adsorption is of the same order of magnitude as the heat of liquifaction of the adsorbate. Since physical adsorption is a reversible process, the removal of the adsorbed layers can be achieved by reducing the vapor pressure at the same temperature at which the adsorption takes place. With highly porous structures or finely powdered adsorbents, diffusion of the gas into the adsorbent mass is often slow, particularly at low pressure, which limits the whole process time.

1.2.2 Chemical adsorption

Compared to physical adsorption, chemical adsorption or chemisorption, involves transfer of electrons between the adsorbent and the adsorbed gas molecules. The process involves the formation of a chemical bond. This can be verified by that the heat of chemisorption is always of the same order as that of the corresponding bulk chemical reactions. Depending on the environment's thermodynamic conditions, the chemical bond can be reversible or irreversible. In contrast with physical adsorption, chemisorption can only occur if the gas is able to form a chemical bond with the surface atoms. The adsorption is complete once a monomolecular layer is build up, although physical adsorption may also occur on top of the chemisorbed monolayer. If irreversible chemical bond forms during the

chemisorptions, the removal of the chemisorbed layer requires high energy (usually thermal energy) to regenerate the sensing film. Chemisorption constitute the basis of a resistive or potentiometric sensor's working mechanism, because only chemical adsorption can be the cause of an electric disturbance [15].

1.2.3 Capillary condensation

Since many water vapor sensing materials have microporous structures, capillary condensation plays an important role in humidity sensing mechanism. The presence of open porous structure permits water condensation in the capillary pores. This is physical adsorption, therefore no chemical reaction and charge transfer involved. The quantity of condensed water depends on the available pore sizes and their distribution. It is possible to evaluate the pore radius at which capillary condensation occurs at a certain temperature and humidity level by using the Kelvin equation [16]:

$$r_K = \frac{2\gamma M_w \cos\theta}{\rho R T \ln\left(\frac{p_s}{p_w}\right)} \quad (1.3)$$

where r_K is called Kelvin radius, γ is the surface tension, M_w is the molar mass of the adsorbate, θ is the contact angle, ρ is the density of water, R is the universal gas constant, T is the temperature, p_s and p_w are the water vapor pressure at saturation and water vapor pressure, respectively. Given that the definition of relative humidity (RH) is [17]:

$$RH = \frac{P_w}{p_s} \times 100\% \quad (1.4)$$

r_k can be calculated under a given temperature and RH. The capillary condensation will

occur in all pores that are smaller than Kelvin radius. For example, water will condense in capillary pores with radius less than about 3nm at 70% RH at 25 °C, and 86nm at 99% RH. For porous structure with uniform pore size and distribution, a sudden increase is always observed in the adsorption isotherms, indicating the start of capillary condensation. Capillary condensation generally contributes to the capacitance change of the porous sensing layer, where the air in the voids is replaced by the condensed water. Since water has a much higher permittivity than air (80 times) for films with micro- or meso-structures and abundant void fractions, the sensitivity of the device can be very high. However, capillary condensation is considered to be the main cause of hysteresis of gas/vapor sensors, which highly limits the sensor's recovery time

1.3 Humidity sensing technology

Hygrometry is in fact “a branch of applied physics in which the multitude of techniques is an indication of the complexity of the problem, and of the fact that no one solution will meet all requirements at all times and in all places” [18]. Depending on which aspect is emphasized, the water vapor content in the atmosphere can be defined by absolute humidity, the relative humidity, dry-/wet-bulb temperature or the dew-point temperature [19]. These parameters can be characterized by mechanical (mass change/volume change/mechanical deformation), electrical (resistive/capacitive/oscillation), optical or temperature measurement. Various instruments have been developed based on these measurement methods, including hydrometers based on hygroscopic materials, psychrometer, dew-point hygrometer and infrared hygrometers.

Various water vapor sensing materials and sensor structures has been studied and de-

veloped to meet different system requirements. Each has its own advantages and shortcomings. In this Section, we will focus on thin-film humidity sensor related technology and give a brief introduction to the state-of-art sensing materials and mechanism.

1.3.1 Humidity sensing material

The sensing material is the key to understand the design and operation of humidity sensors. Commonly used humidity sensing materials include moisture absorbing polymers, polyimide, poly-electrolytes, porous ceramic (metal oxides), and porous silicon/polysilicon. The adsorption of water molecular on these materials surface will change their properties, which can be mechanical, electrical or optical properties. We will highlight organic polymers and humidity sensing ceramics, which are the most investigated sensing materials for humidity sensors. As the focus of our work, the humidity sensing properties of porous silicon will be detailed in Chapter 2.

Organic polymer

Water adsorbing polymers can be used as the sensing elements in several ways [20]. For nonconductive polymers, their dielectric constants will change due to water uptake. The original dielectric constant of the polymer film will turn into the value of a mixture of adsorbed water and the polymer, which can be calculated from Looyenaga's equation [21] as:

$$\epsilon = \left(v_2 \left(\epsilon_w^{\frac{1}{3}} - \epsilon_p^{\frac{1}{3}} \right) + \epsilon_p^{\frac{1}{3}} \right)^3 \quad (1.5)$$

where ϵ_p is the dielectric constant of the polymer, ϵ_w is the dielectric constant of water,

and v_2 is the fractional volume of water diffused into the polymer. Most polymer humidity sensors are based on this mechanism.

The adsorption of water can also cause the swelling of the polymer, which will result in the mass or dimension change of the sensing film. These can be detected by surface acoustic wave (SAW) humidity sensors or piezoelectric cantilever with multi-layered structure. For conductive polymers, the conductance change caused by water adsorption is usually measured by a pair of electrodes patterned on the sensing film.

The advantages of polymer based humidity sensors are their fast response, resistance to contaminants, good repeatability and low hysteresis. However, the serious shortcoming with polymer sensors is their incapability to work at high RH level (condensing environment) and high temperature [22]. For example, the Honeywell HIH sensors, based on their data sheet, the maximum operation temperature is 85 °C, 65 °C when RH is above 80%, and 50 °C at saturate condition. This highly confines their application in extreme and harsh environment.

Ceramic

Ceramics, essentially metal oxides, have been used in humidity sensors in the forms of porous sintered bodies and ceramic thin films [23]. The bulk porous ceramics are usually prepared by sintering a mixture of metal oxide powders. With the development of micromachining and on-chip integration technology, metal oxide thin films can also be deposited on desired substrates by vacuum evaporation, sputtering or chemical vapor deposition (CVD). Commonly investigated metal oxides include Al_2O_3 , ZnO , TiO_2 , and their compounds with other metal ions, for example $\text{MgCr}_2\text{O}_4 - \text{TiO}_2$ [24] and $\text{ZnCr}_2\text{O}_4 - \text{LiZnVO}_4$ [25].

The electrical properties of ceramics change because of the chemisorption of water vapor on the available sites of the oxides surface, mainly at the grain boundaries. The reaction is related to the dissociation of the water molecule and the formation of one proton and a hydroxyl ions. When temperature is lower than 100 °C, physical adsorption of subsequent layers on the first hydroxyl layer also accounts for the property changes. For porous ceramic with microporous structures, capillary condensation is another factor to be considered as the sensing mechanism at high RH level.

The advantages of ceramics include their ultra high surface-to-volume ratio, their mechanical strength and their thermal and physical stability. However, due to the chemisorption reaction, ceramic humidity sensors need periodic regeneration by heat cleaning to recover their humidity sensitive properties. The main purpose is to remove the stable chemisorbed OH^- on the surface of the porous structure or grain boundaries. This usually requires a temperature up to 400 – 500 °C. More over, adsorption of impurities such as dust and dirt may cause irreversible changes to the sensing layer, as they act the same way as chemisorbed water. This makes ceramics less resistant than polymers to surface contamination.

1.3.2 Transduction technique of humidity sensors

Capacitive humidity sensor

Capacitive sensors are based on the dielectric constant change of the sensing layer caused by the adsorption of water molecules. This change can be caused by the swelling of the polymer film, or capillary condensation in porous structures as introduced above. One typical sensor structure is the sensing layer sandwiched by two electrodes with the top one

being an ultra thin or porous metal film for the diffusion of water vapor. Capacitance can also be measured by patterned top electrode geometries, such as interdigitated electrodes (IDE) or spiral on top of the sensing layer. These electrodes allow the vapor to diffuse freely into the dielectric and give a faster response. However, the field distribution is not as uniform as thin film electrodes. An intermediate solution is making the top electrode into small meshes. Figure 1.3 shows different electrodes geometries for capacitive sensors. Among these structures, IDE is the most widely used structure in gas/humidity sensors.

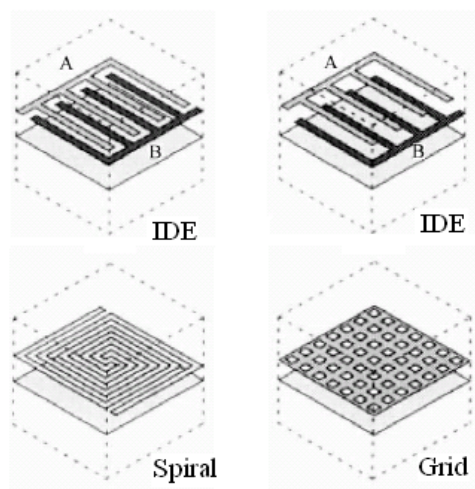


Figure 1.3: Electrodes geometry for capacitive humidity sensors [5]

Resistive humidity sensor

Resistive humidity sensors transduce air humidity into an impedance change, which can be measured by current, voltage or resistance. The design of resistive sensors is usually comparable to capacitive sensors, for example with IDE electrodes on top or bottom of the sensing film. Both polymer and porous ceramic can be built into resistive humidity sensors. For polymers, it's usually the proton conductive ones, such as NafionTM [26]. For ceramics,

the resistance changes are caused by the chemical reaction between water molecule and the surface atoms, which can be electronic type or ionic type.

Gravimetric humidity sensor

The gravimetric humidity sensors are based on the mass change of the sensing film due to the water vapor uptake. In a vibrating mechanical structure, which is already vibrating at its natural frequency, the increase of mass will result in a resonance frequency shift in proportion to the added mass. Bulk acoustic wave (BAW) or quartz crystal microbalances (QCMs) and surface acoustic wave (SAW) sensors are all based on this principle. QCMs generally consist of a quartz disk sandwiched between two thin film electrodes that are coated with water vapor adsorbing polymer films. Therefore, QCM devices utilize the longitudinal standing waves along the thickness of the bulk material. In contrast, SAW devices resonate as a standing wave within a thin surface layer of a piezoelectric substrate. Two IDEs are located at each end of the substrate, one as a transmitter and the other as receiver. The polymer film is patterned between these two IDEs and water adsorption will affect the transit time of the acoustic wave - thus the output frequency, amplitude or phase. Gravimetric humidity sensors usually show a better sensitivity and accuracy than other sensors at very low RH.

Optical humidity sensor

Relative humidity can be measured by optical methods in several ways. One widely used apparatus is the fiber-optical sensors. Light is generated from an optical source, passes through a fiber and received by an optical detector. The fiber is coated with water vapour adsorbing layer. The frequency, transmitted power, or wavelength of the received light can

be changed as function of vapour adsorption. The sensing property can be enhanced by functional coatings on the surface of the fiber [27, 28]. Another sensor is nondispersive infrared (NDIR) detector, which usually consists of an IR light source, optical filters and IR detector. It measures the absorption of infrared (IR) radiation by water vapor within an optically enclosed chamber. Chilled mirror hygrometer is another water vapor sensor which is especially appropriate to measure the dew point. The advantages of optical humidity sensors include ease of miniaturization, operation in harsh environment, and potential for remote sensing. However, their main drawbacks are susceptibility to contamination and the complexity of the entire system.

Among these humidity affected variables, capacitance and resistance/conductance are the most widely implemented due to their simplicity for fabrication and detection.

1.4 Humidity sensor with ordered porous structures

Recently, with the development of synthesis technologies, more and more attention has been attracted to the field of highly-ordered microstructures, mainly being mesoporous ($2\text{nm} < d < 50\text{nm}$) and macroporous ($d > 50\text{nm}$) thin films due to their great potential for electrochemical analysis [29, 30]. Porous materials, both organic and inorganic, have proved their advantages in various chemical, electrocatalysis and biochemical applications. To optimize their characteristics (electrical or optical), special care during the fabrication process has been taken to obtain well-ordered structures with a narrow distribution of open pores and highly accessible surface areas. In this section we will summarize several published works on humidity sensing with ordered mesoporous or macroporous structures [31, 32, 33, 34].

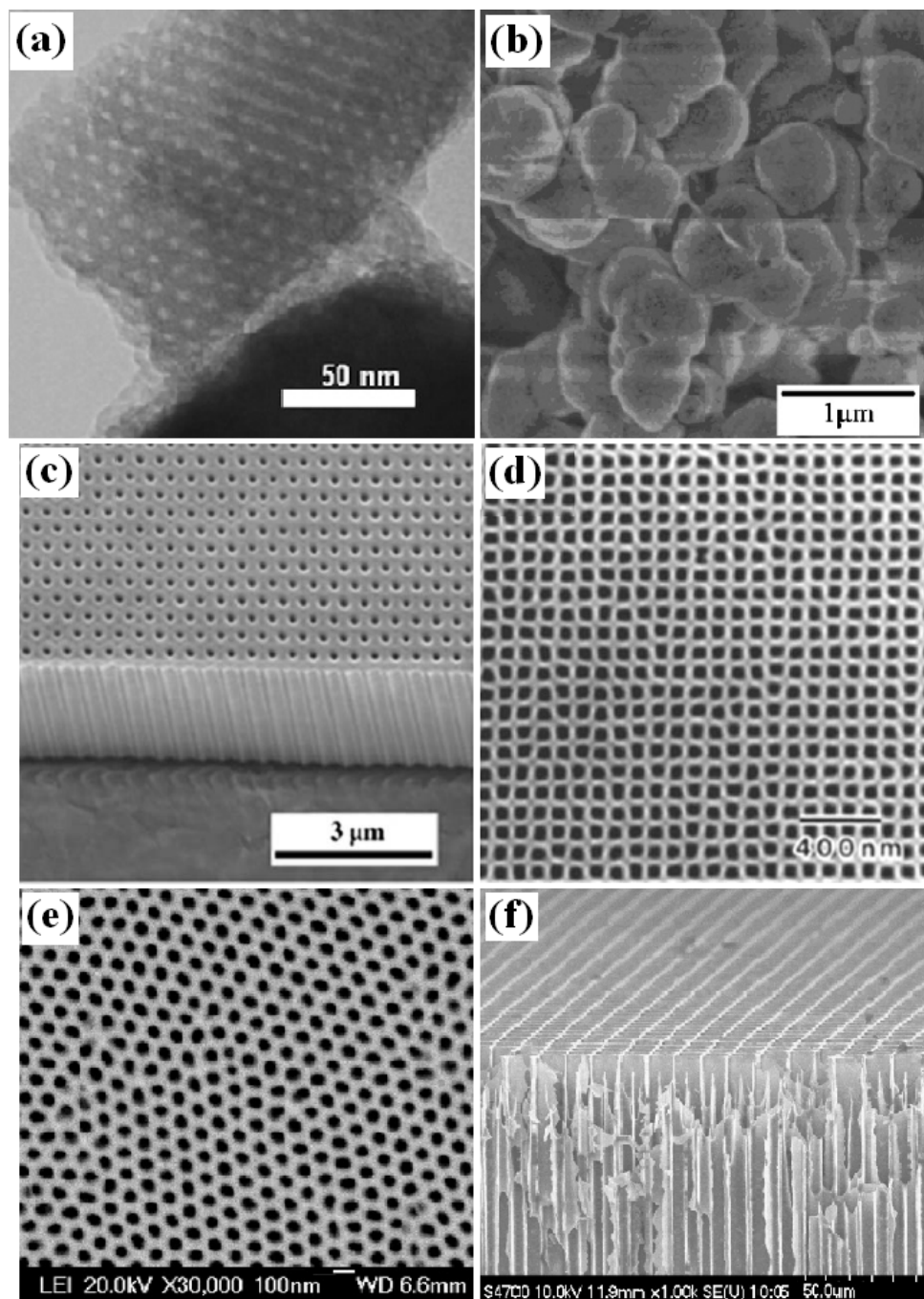


Figure 1.4: (a) TEM image of calcined-SBA-16 view from [111] direction [35]; (b) SEM images of pure MCM-41 [36]; (c) an array of approximately 100 nm porous anodic alumina (PAA) channels perfectly organized in a hexagonal arrangement; (d) PAA channels with square arrangement [37]; (e) SEM image of anodic aluminum oxide (AAO) with electrode layer on top [38]; (f) SEM images of the ordered high areas ratio silicon microchannel plate (MCP) [39].

Figure 1.4 shows various highly-ordered mesoporous or macroporous structures. Metal oxides, silicon and silica are all commonly used materials for the formation of ordered structures. Figure 1.4(a) shows a TEM image of Li-doped 3D periodic mesoporous silica SBA-16. The sample is prepared from inorganic salts and shows three orders of magnitude impedance response to relative humidity change from 0% to 95% [35]. Figure 1.4(b) shows another common mesoporous silica MCM-41 from the family of M41S. Wang et al. [36] investigated its humidity sensing behavior with and without Li dopant. The Li-doped sensor shows high sensitivity between 0% RH and 95% RH and linearity improvement. Anodic aluminum oxide (AAO) or anodic alumina is another intensively studied ordered porous material which can be tailored to various mesoporous structures. Figure 1.4(c)-(e) shows three different morphologies of the AAO. The samples have well defined pore shape and size and show a good uniformity over large area. A humidity capacitive sensor is built on the sample shown in Figure 1.4(e). The electrode pattern can be fabricated on top of the thin film either by lithography or physical mask. With an integrated heater, the sensor shows good sensitivity with very small hysteresis [38]. Figure 1.4(f) shows a nickel coated silicon microchannel plate fabricated by electrochemical etching. The structure has a macropore of 5 μm and the channel length of 200 μm . Interdigitated electrode was screen printed on top of the structure and its capacitance was tested to RH changes. The sensor shows a high sensitivity with a small hysteresis.

From the examples above we can see that highly-ordered mesoporous and macroporous structures show great advantages in terms of morphology controlling and tailoring. This will allow the modification and optimization of the sensor's properties and performance. With further development of fabrication technology, highly-ordered porous structure will show huge potential and application on various chemical sensing systems.

Chapter 2

Porous Silicon

Porous silicon (PS), as one of the most important porous materials, has been studied intensively in terms of gas molecules adsorption and desorption on the surface. In this chapter, the formation, property and applications of PS are summarized. And the state-of-art PS based gas/humidity sensors that have been developed by other groups are discussed.

2.1 Formation of porous silicon

The fabrication of porous silicon is an electrochemical anodization process of doped silicon in hydrofluoric acid (HF). The etching setup usually consists of an electrochemical cell and electrical connections. The cell includes a counter electrode and working electrode, which is the silicon sample. Both are immersed into the HF solution. For fabrications of PS on n-type Si substrate, illumination during anodization is required. The pore formation is basically the dissolution of silicon in HF but with remarkable difference in the dissolution rate between pore tip and pore wall. Therefore, it is a continuous passivation of the pore

walls and passivity breakdown at the pore tips. Due to different formation mechanisms, porous silicon is classified by the pore diameter into microporous ($d < 2\text{nm}$), mesoporous ($2\text{nm} < d < 50\text{nm}$) and macroporous ($d > 50\text{nm}$) [40]. In addition to pore size, porosity, and specific surface area are usually used to evaluate the porous structure.

2.2 Property and application of porous silicon

2.2.1 Electrical property of porous silicon

The conductivity for PS depends on the size of the conducting filaments making up the structure. For microporous silicon, it shows very high resistivity in dry air at room temperature, ranging from 10^7 to $10^{14} \Omega \text{ cm}$. When exposed to humid air or polar vapors, the resistivity decreased by two or three orders of magnitude. This is usually interpreted by the condensation of water vapor in the porous structure. For mesoporous silicon, the high value of resistivity is believed to be caused by the constrictions of conductive pathways produced by charged surface traps. Upon exposure to polar vapor, these charged surface traps can be screened, which will result in the decrease of resistivity. For macroporous silicon, the pore spacing is much larger, so that the effect of the surface depletion layer becomes negligible and the conductivity is determined by the geometry of the sample only.

The capacitance of PS is usually measured with a metal/PS/Si sandwich structure. The value is found to be dependent to the porosity and the measuring frequency. Upon exposure to humidity, the capacitance of PS increases due to the formation of water molecule layers on the surface or the water condensation.

2.2.2 Photoluminescence of porous silicon

Photoluminescence (PL) in the visible light range is a very important property of PS, which has been the motivation for most PS related research. The PL is usually excited by a wavelength shorter than the emission wavelength. The characteristics of the PL change as the wavelength of emission changes from ultraviolet (UV) to infrared (IR). These discrete set of wavelengths are grouped into three bands, called the “red”, “blue” and “IR” band respectively. The PL characteristic is strongly dependent on the anodization variables, including the current density, bias voltage, and the electrical properties of the substrate. This indicates that the visible light emission is closely related to the dimension and the morphology of the PS [41]. The PL from PS is usually measured with PL spectra and studied in terms of the PL intensity and peak wavelength. It was observed that, upon exposure to polar gas molecules, the PL intensity decreases significantly. This PL quenching effect from gas adsorption has been studied widely for gas sensing applications [42].

2.2.3 Application of porous silicon

Due to its special structural, electrical and optical properties, PS has a wide range of applications. Structurally, it can be used as a sacrificial layer in MEMS fabrications, especially ordered macroporous silicon with straight pores. It can be used as a template to form other materials with the same geometric precision. Electrical applications include cold cathodes and capacitors, while optical applications include light-emitting diodes (LEDs), short-pass filters, waveguides or photonic crystals. In the next Section, we will highlight its application for gas/humidity sensing, which is the focus of this thesis.

2.3 Porous silicon based gas/humidity sensor

The hollow structure, ultra high surface area and volume-to-surface ratio of PS makes it a good candidate for chemical vapor sensing. Gas/vapor sensors based on changes in dielectric constant, resistance or PL intensity/quenching of PS upon absorption of chemical species, especially polar molecules, such as H_2O , NO , NO_2 , NH_3 , alcohols and methanol have been widely studied and developed. The sensing mechanism is usually interpreted as the surface charge change by polar molecules or gas/vapor condensation in nano-size pores [43]. Compared to PL quenching, the electrical method is more practical for both commercial and industrial applications. Here we will give some examples of PS based gas/vapor sensors, especially humidity sensors that have been developed by other groups.

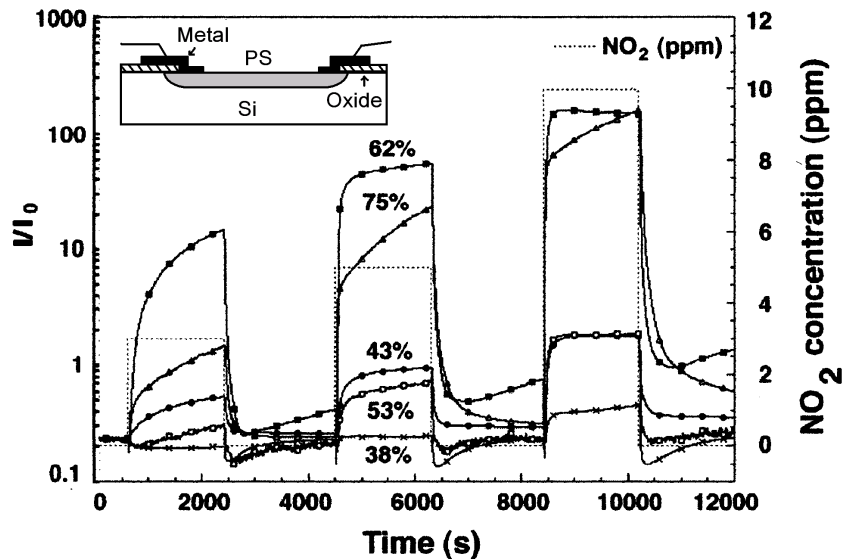


Figure 2.1: Dynamic response of PS gas sensor of different porosities to NO_2 at room temperature and 20% RH; the insert shows the sensor structure [44]

Figure 2.1 shows a typical resistive PS based gas sensor. The PS layer is 20-30 μm thick [44]. With a sputtered oxide layer on the frame, the metal contacts were only de-

posited on top of the PS area, and the resistivity was measured between these two terminals. A significant increase of the PS conductivity was observed upon exposure to low concentration of NO_2 and the effect of porosity on sensitivity was showed. However, the same structure didn't show any response to non-polar gases like CO and CH_4 . The ambient humidity showed a noticeable effect on the sensor's sensitivity. Figure 2.2 (a) and (b) shows two different sensor structures for organic vapor sensing [45, 46]. Good sensitivity and repeatability were obtained, indicating the wide range application of PS on gas sensing systems.

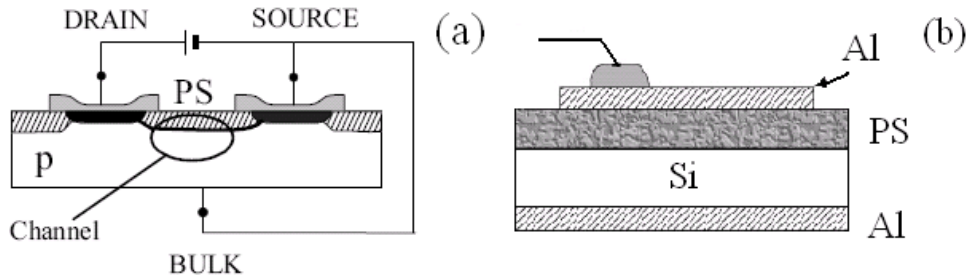


Figure 2.2: (a) A PS based FET sensor for isopropanol sensing [45]; (b) A PS capacitor with sandwich structure for acetone and ethanol sensing [46].

Tremendous research has been devoted to the PS based humidity sensors as well [47, 48, 49]. Anderson et al. [50] reported the capacitance sensitivity of PS to RH firstly. A 440% increase in capacitance in response to a humidity change from 0% to 100% has been observed in a PS sensor with Al contact on top. The change in the effective permittivity was attributed to condensation of water in the porous structure. However, capillary condensation is a major cause of slow recovery and hysteresis in humidity sensors. Generally, small pores or complicated connectivity between the pores may increase hysteresis [51]. Mikko Bjrkqvist et al. [52] developed a thermally carbonized PS (TCPS) humidity sensor with the same structure shown in Figure 2.1, and demonstrated that by enlarging the pore

size and operating the sensor a few degrees above room temperature the hysteresis can be significantly reduced. They also investigated the temperature dependence of the sensor's sensitivity. As shown in Figure 2.3, the capacitance and resistance change of the sensor as a function of RH at different temperatures has been measured. It was found that the capacitance of the sensor in dry air is almost constant at various temperatures, whereas in higher RH, the temperature dependence becomes evident. The capacitance sensitivity increases under higher temperatures, while the resistance variation of the sensor is less dependent on RH as temperature increases. This indicated the potential of PS humidity sensor to work under elevated temperatures with high sensitivity.

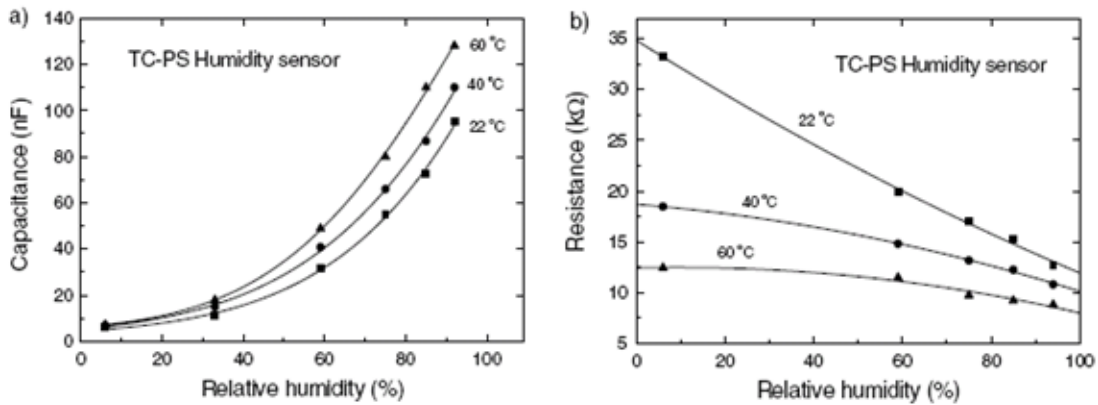


Figure 2.3: (a) Capacitance and (b) resistance of a TCPS humidity sensor as a function of relative humidity at three different temperatures. Measurements were done using 120 Hz frequency [52].

Jayoti Das et al. [53] developed a novel hygrometer combining a PS dielectric humidity sensor with a phase detection electronic circuit (PDC). The humidity sensor has been fabricated on a PS membrane structure with IDE on top and a built-in planar micro hot plate for restoration, as shown in Figure 2.4 (a). The PDC has been developed to measure and monitor the capacitive changes. It has been shown that, with auto ranging and offset compensation built-in the PDC, the sensing behavior was improved significantly. The

hygrometer exhibited a linear response over a wide range of RH, and very small hysteresis, as shown in Figure 2.4 (b). The response time was less than a few seconds. The PDC is compatible to silicon processing technology, therefore can also be integrated onto the sensor chip.

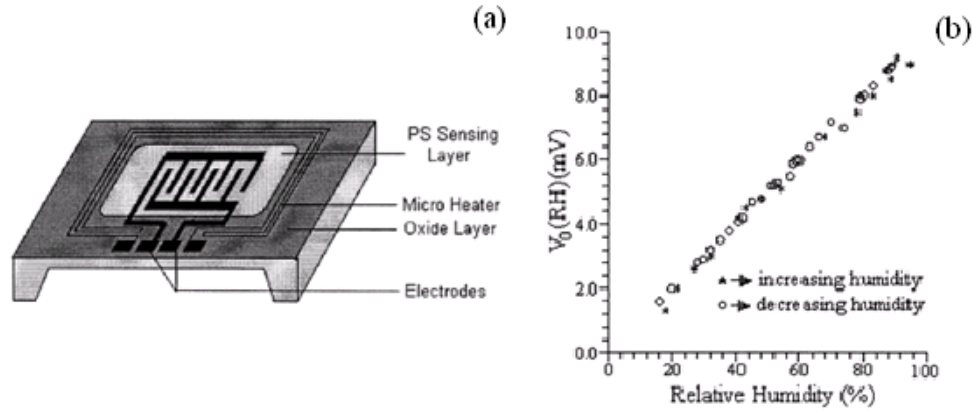


Figure 2.4: (a) Schematic of the sensor structure; (b) Sensitivity of the sensor in combination with the electronics [53].

2.4 Ordered macroporous silicon

The first formation of ordered macroporous silicon by electrochemical etching was reported by V. Lehmann in 1990 [54]. Using lithographic pre-patterning, the nucleation spots of the pores can be defined at the surface of the n-type silicon, followed by photo-electrochemical dissolution to obtain two-dimensional or three-dimensional ordered porous structure [55], as shown in Figure 2.5. This ordered structure can have a pore-to-pore distance of $1.5 \mu\text{m}$ to $6 \mu\text{m}$ and a pore diameter of about half the pore-to-pore distance.

The length of the pore can be controlled by the etch time and reach $200 \mu\text{m}$ without any degradation in the ordering and uniformity. By wet etching substrate bulk silicon,

a ordered macroporous silicon membrane can be obtained with both ends of the pores open to the environment. Due to different pore formation mechanism, the flexibility of pore array design on low doped p-type silicon is less than that for macropore formation on n-type substrates [56].

Recently, M. Archer et al. [57] developed a macroporous silicon electrical sensor for real-time, label free DNA hybridization detection. The macroporous silicon (1-2 μm) was fabricated on p-type silicon and had straight and smooth pore walls without interconnection. In addition to the advantages of traditional porous silicon for gas sensing (good stability, high resistance to high temperature and good compatibility with current IC fabrication process), ordered macroporous silicon has the following advantages:

- Uniform pore size, shape and distribution
- Vertically aligned pores that can open to the environment on both ends, which can significantly increase the diffusion efficiency of gas molecules into the pore surface
- Easier for diffusion of water vapor and other agents than interconnected pores;

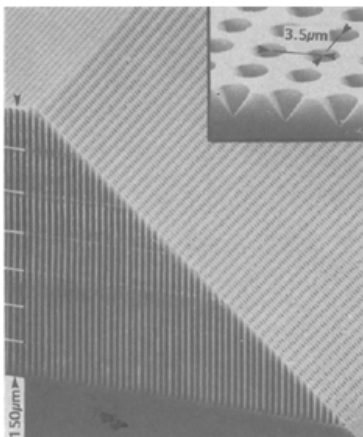


Figure 2.5: SEM micrograph of an ordered macroporous array etched on n-type silicon; the insert is a square pattern of pits produced by standard lithography [53].

- Controllable parameters for performance optimization;
- Uniform growth or deposition of thin film coatings for surface modification can be achieved;
- The ordered structure without any pore interconnections allows better understanding of the gas molecule interaction with PS surface and chemical adsorption characteristic.

Based on the above advantages, ordered macroporous silicon is used as the humidity sensing layer in this work. This is the first time that the humidity sensing characteristic of ordered macroporous silicon is investigated.

Chapter 3

Ordered Macroporous Silicon with and without Thin Film Surface Coating for Humidity Sensing

In our experiment, three generations of ordered macroporous silicon humidity sensors are fabricated on n-type silicon. For the first generation, the resistive sensitivity of both heterostructure (ordered macroporous silicon/n-Si substrate) and self-supporting membrane is measured. For the second generation of the devices, ordered macroporous silicon with different porosity, surface area and surface coatings are fabricated. Al electrodes are deposited onto the macroporous silicon surface with a physical mask by evaporation. Both of their resistive and capacitive sensing properties to RH change are characterized. For the third generation of the devices, interdigitated electrodes (IDEs) pattern is fabricated on top of the ordered macroporous silicon by microfabrication techniques and another new metal oxide coating is investigated. In this chapter, we will report the related experiment for the

first two generations of the sensors. The details of third generation will be introduced in the next chapter.

3.1 Fabrication of the ordered macroporous silicon

The ordered macroporous silicon is prepared by electrochemical etching of (100)-oriented n-type Si in hydrofluoric acid under backside illumination. Lithography and subsequently etching in KOH is used to define the nucleation spots of pores on the surface of the silicon wafer. The wafer is cleaved into small pieces with a dimension of about 23 mm \times 23 mm to fit into the etch setup, as showed in Figure 3.1. A piece of patterned silicon is clamped in a PVC cell, which is 20 mm in diameter. The front side is exposed to aqueous HF (5%) for etching, while the backside is illuminated to create electronic holes via light absorption in the silicon. The pore diameter is controlled by the backside illumination intensity. A voltage is applied between the silicon wafer and counter electrode in the HF acid to protect the pore wall against electrochemical dissolution. Simultaneously, the HF solution is continuously pumped to avoid a loss in concentration and to remove hydrogen bubbles sticking to the surface.

To evaluate the role of the porous matrix as the sensing layer, a self-supporting membrane is fabricated and tested under the same environment. To obtain the self-supporting membrane, the etched sample is first oxidized for 2 hours at 900 °C. The surface of the pore is then covered with an oxide layer which is about 20 nm. Then the backside of the sample is etched away in KOH solution up to the bottom of the pores. This results in both ends of the pores exposed to the air. The oxide layer is then removed by a quick-dip into wet etchant. Figure 3.2 shows a 3D view of the ordered macroporous structure with perfectly

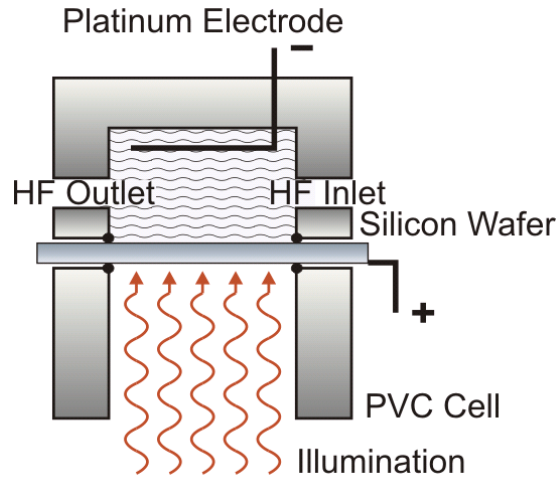


Figure 3.1: Schematic diagram of etching setup

aligned pores and high aspect ratio, and the backside of the self-supporting membrane after the removal of substrate. The fabricated macroporous silicon has cylinder array with pore diameter of $1 \mu\text{m}$ and a pore length of $200 \mu\text{m}$.

After being exposed to air for several hours, a native oxide layer of about 3 nm will form on the fresh macroporous silicon surface, and will remain stable with this thickness. This is crucial for humidity sensing. Schechter et al. [58] attributed their PS's humidity insensitivity to its hydrophobic nature. Anderson [50] developed a capacitance PS humidity sensor with high sensitivity which also had a thin oxide layer on the pores surface. The reason why pure or fresh PS shows negligible response to H_2O (although it has large dipole moment) is the hydrophobic nature of the PS surface. PS is usually fabricated in HF solution; therefore, pure PS has a hydrogen-terminated surface and water cannot wet this surface [59]. Surface modification with oxides can turn part of or the whole surface to be O-terminated, and thus hydrophilic, which allows the adsorption of water molecules.

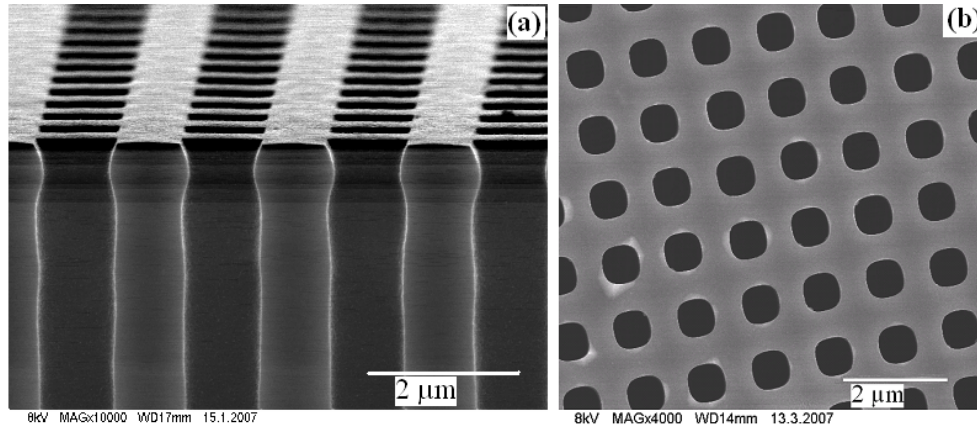


Figure 3.2: (a) Profile SEM image of a 3D ordered macroporous silicon with square pores; (b) A SEM image of the backside of a self-supporting membrane with ordered structures.

3.2 Measurement setup

3.2.1 Experiment setup

The samples are tested in a sealed chamber with controllable and stable RH and temperature. The chamber has two gas inlets and one outlet. One inlet connects to extra dry air directly, and the other connects to a water bottle where the extra dry air becomes water saturated by bubbling with water. The humidifier is placed in a water bath at the desired temperature. Two individual mass flow controllers are implemented to control the ratio of the dry and saturated air. As a result, the RH range within the chamber can be controlled from 0% to 100%. A commercial humidity/temperature sensor is put in the chamber as a reference to indicate the RH level and temperature in the testing chamber. Real-time resistance and capacitance measurements are performed with a LRC/ESR meter (PK PRECISION 889A). A micro-heater is also placed in the chamber to control the temperature. The micro-heater is controlled by an external power supply. A micro-thermocouple is attached to the backside of the sample to monitor the sample's temperature when testing

under high temperature. A LabVIEW program is used to control the mass flow controllers and collect data from the reference sensor, the LCR meter and the thermocouple. Figure 3.3(a) shows the detailed schematic of the experiment setup and Figure 3.3(b) shows a picture of the setup and the testing chamber (insert).

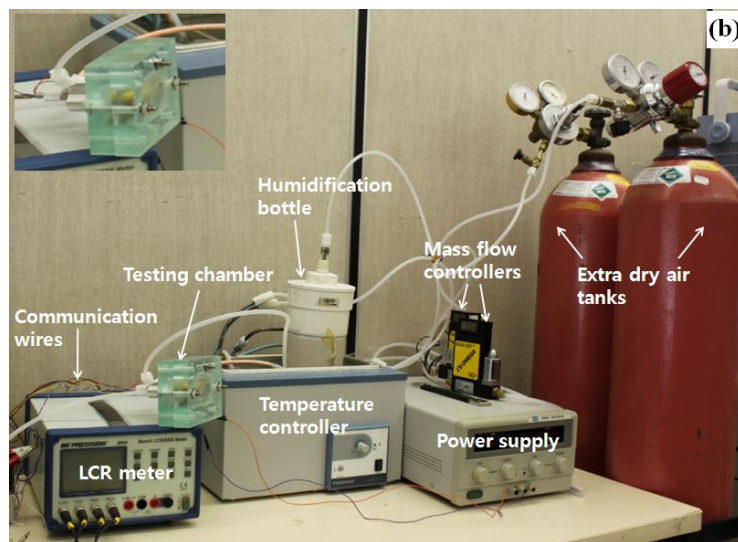
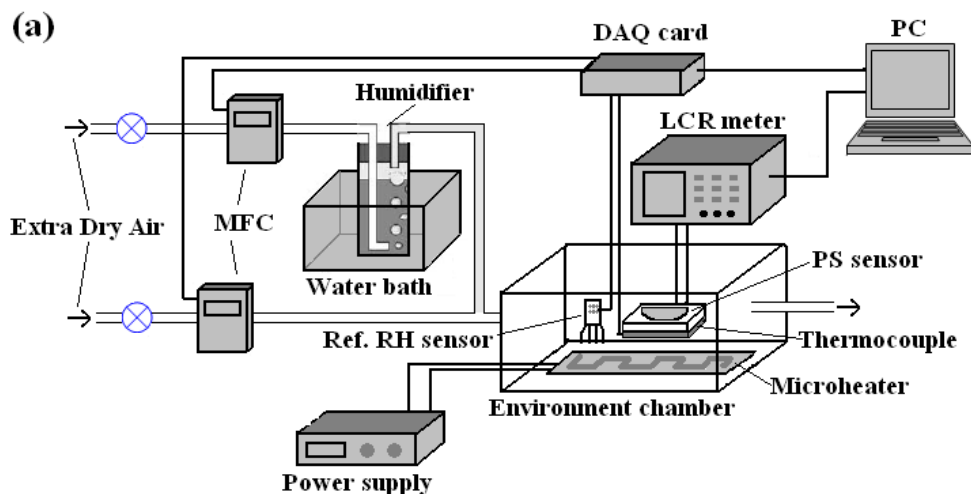


Figure 3.3: (a) A schematic, and (b) a picture of the experiment setup; the insert is a picture of the testing chamber.

3.2.2 Humidity generation and measurement at high temperature

The amount of atmospheric water vapor content in air can be defined in several ways. The most useful definitions are absolute humidity, vapor pressure and relative humidity [19]. Absolute humidity is the mass of water vapor carried by unit mass of dry air. Preferred units are lb/lb or kg/kg. Vapor pressure p is the partial pressure of vapor in gas-vapor mixture. It is proportional to the mole fraction of vapor and the environmental pressure as shown in equation 3.1.

$$p = \frac{n_v}{n_v + n_g} \times P \quad (3.1)$$

Relative humidity (RH) is the partial pressure of water vapor p_w divided by the saturation vapor pressure p_s at the given temperature.

$$RH = \frac{P_w}{p_s} \times 100\% \quad (3.2)$$

Saturate water vapor pressure p_s , as shown in Figure 3.4, is a function of temperature [60]. With the increase of temperature, the air can retain larger amount of moisture. Therefore, when generating a certain RH level in the testing chamber at a certain temperature, it is important to take into account the temperature difference between the chamber and humidifier. Figure 3.5 explains the effect of temperature change on the RH level of a certain amount of air. For example, when the temperature of a certain amount of saturate air increase from 23.3°C (75°F) to 40°C (104°F), the absolute humidity does not change. But the RH changes from 100% to approximately 40% (from A to B). To make sure the humidified air is still saturated when entering the testing chamber, the temperature of the

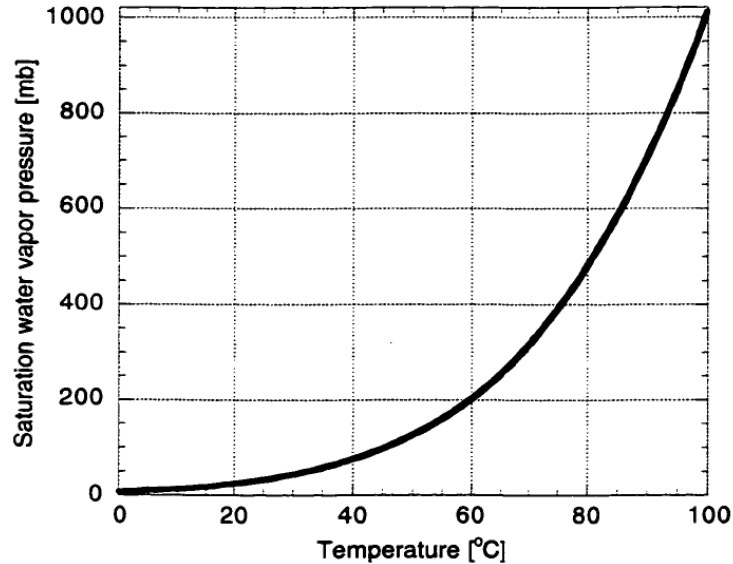


Figure 3.4: Saturation water vapor pressure as a function of temperature [60].

humidifier is set 5 – 10 °C higher than the testing temperature in the chamber.

3.3 Ordered macroporous silicon without surface coating

3.3.1 Testing structure and terminology

To measure the resistance response of the sensor to RH, two plastic insulators are bonded on top of the silicon frame around the porous area by instant glue. Conductive epoxy with a resistivity of 0.02 ohm·cm is used as electrodes and to make the wire connections. Figure 3.6 shows the schematic diagram of the testing structure. To eliminate the effect of the bulk silicon frame, all electric contacts are only on the porous silicon area.

In this report, we define the percentage resistance variation (PRV) at a certain RH

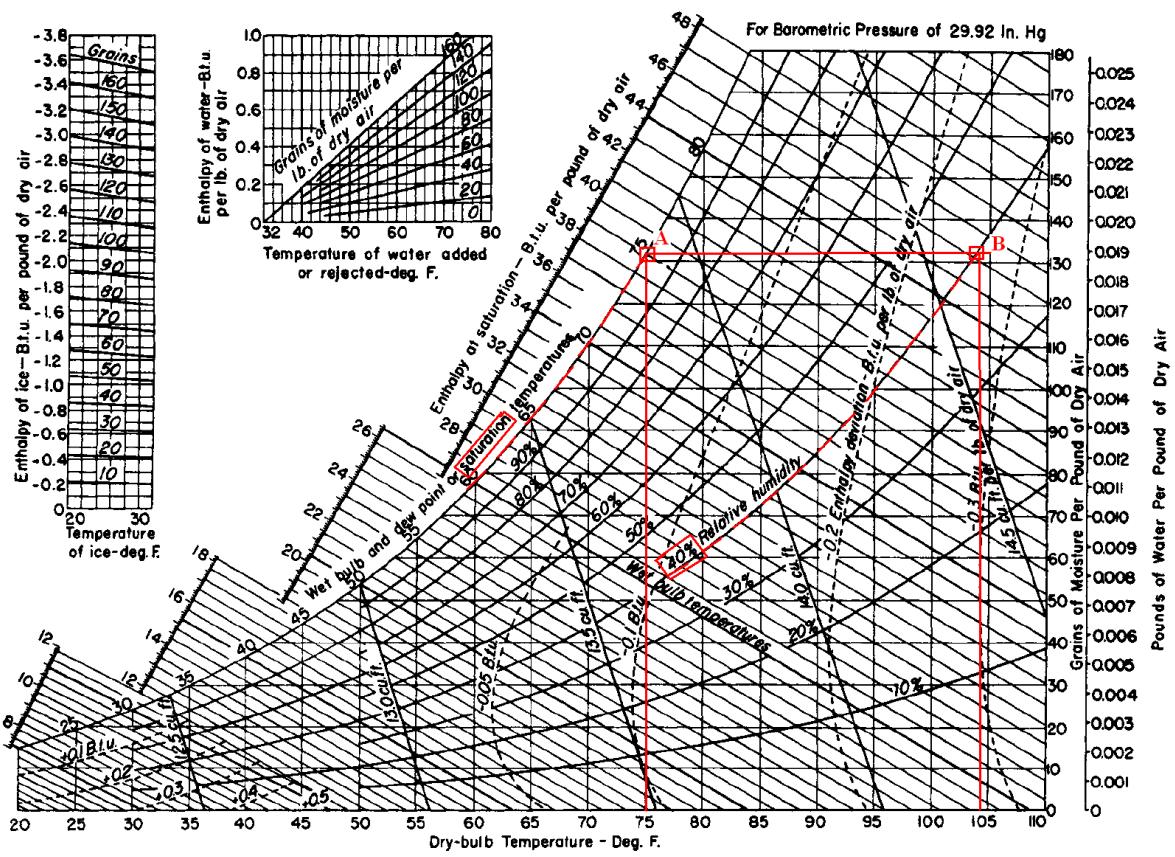


Figure 3.5: Grosvenor psychrometric chart (medium temperature) for the air-water system at standard atmospheric pressure [19]

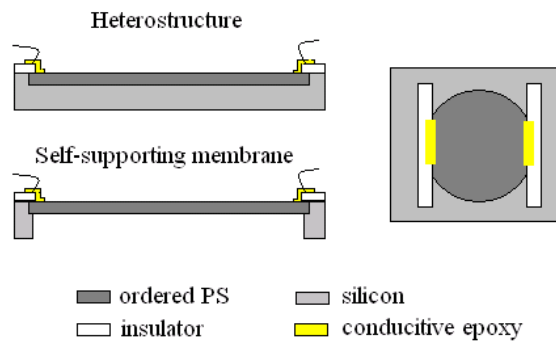


Figure 3.6: Schematic diagram of testing structure for ordered macroporous silicon heterostructure and self-supporting membrane: side view and top view

level as,

$$PRV_{@RH\%} = \frac{(R_{@RH\%} - R_0) \times 100\%}{C_{p0}} \quad (3.3)$$

We define the sensor's resistance sensitivity (S_R) as,

$$S_R = \frac{\delta R}{\delta RH} \quad (3.4)$$

Where $R_{@RH\%}$ is the resistance of the sensor at a certain RH level and R_0 is the original resistance reading of the sensor at 0% RH.

The same definition also applies to capacitance test. The percentage capacitance variation (PCV) at a certain RH level is,

$$PCV_{@RH\%} = \frac{(C_{@RH\%} - C_0) \times 100\%}{C_{p0}} \quad (3.5)$$

and the sensor's capacitance sensitivity (S_C) as,

$$S_C = \frac{\delta C}{\delta RH} \quad (3.6)$$

Where $C_{@RH\%}$ is the capacitance of the sensor at a certain RH level and C_0 is the original capacitance reading of the sensor at 0% RH.

3.3.2 Resistance response of ordered macroporous silicon without surface coating

The resistance responses of both structures are tested under increasing RH from 0% to 100% in incremental steps. Each step is maintained at a constant value for 10-12 minutes. When the RH is changed to a higher level, an immediate decrease of resistance is observed. Initially, the resistance decreases rapidly and then slows down before reaching a steady resistance value. Figure 3.7 shows the *PRV* to RH relationship of the ordered macroporous heterostructure and the self-supporting membrane. The self-supporting membrane demonstrates a higher *PRV* to RH than heterostructure at each step. Overall, its *PRV* is 28.3% and the *PRV* of heterostructure is 23.5%. This can be explained by two factors. The first one is that the membrane's pores open on both ends, which results in more efficient water molecule diffusion and adsorption to the pore surface. The second one is that the self-supporting membrane does not have the bulk silicon in the back acting as parasitic resistance, lowering the base resistance of the sensor. Therefore, it shows a higher sensitivity.

The sensitivity at RH <25% is relatively low for both structures, and becomes larger with the increase in RH. The low sensitivity at low RH indicates that, a minimum RH or longer time is required for the pore surface to be wetted and screened by water molecules on the surface. It also indicated that the vapor adsorption is faster at higher RH level. This has been previously observed [43].

We believe that the conductivity enhancement is due to the surface charge change induced by the adsorbed water molecules. Lehmann et al. [61] suggested the resistance of PS is a surface effect. The decrease of PS conductivity compared to bulk silicon is interpreted

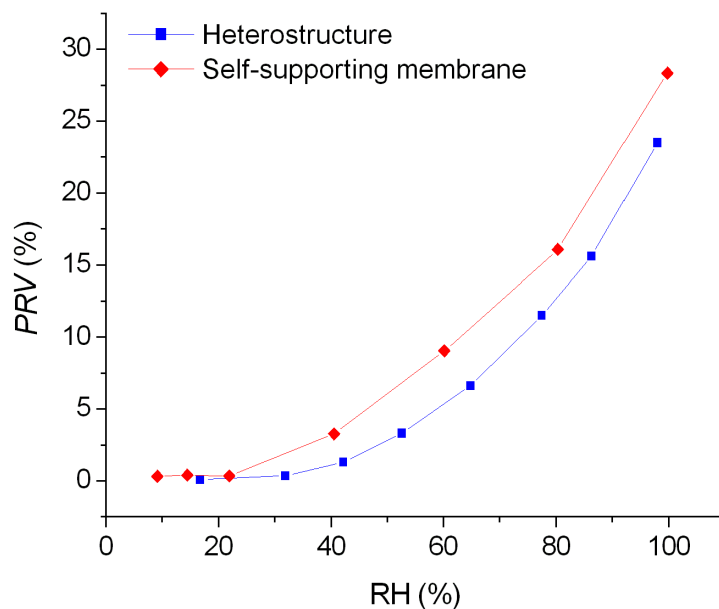


Figure 3.7: *PRV*-RH curves of the heterostructure and self-supporting membrane.

as the result of constrictions of conductive pathways by surface traps/surface states. Adsorption of polar vapor molecules can screen the surface charge traps, releasing trapped electrons back to the conducting band thus enhancing the PS conductivity. Electrochemical conducting process caused by the physisorbed layers of water molecules also contributes to the conductivity enhancement. We believe that the conductivity enhancement in this case does not involve conductance of condensed water liquid within the porous structure. Based on the Kelvin equation, capillary condensation requires the pore size to be in nanometer scale. For example, condensation of water occurs in a 3nm pore with hydrophilic surface at 70% relative humidity at 25 °C. For this ordered macroporous, all pores have the same diameter of 1 μm , which is not sufficient for capillary condensation of water.

The repeatability test is carried out for both structures between dry air and saturated air. Each step is maintained for 10-12 minutes, within which the RH in the chamber

can only recover to around 10% from 98% RH under extra dry air flow, as shown in Figure 3.8. Both structures show good repeatability. At the onset of saturated air, the resistance reading of both structures reaches 50% of the total change within 2-3 minutes and 90% within 6-7 minutes. At the onset of extra dry air, the self-supporting membrane reached 50% of the total change within 3 minutes and 90% within 7 minutes. It can completely recover in 10 minutes, while the heterostructure needs 12 minutes for recovery. The better stability and faster response/recovery time of the self-supporting membrane can be interpreted by the easier diffusion of water molecules into and out of the porous structures due to the opening of both ends.

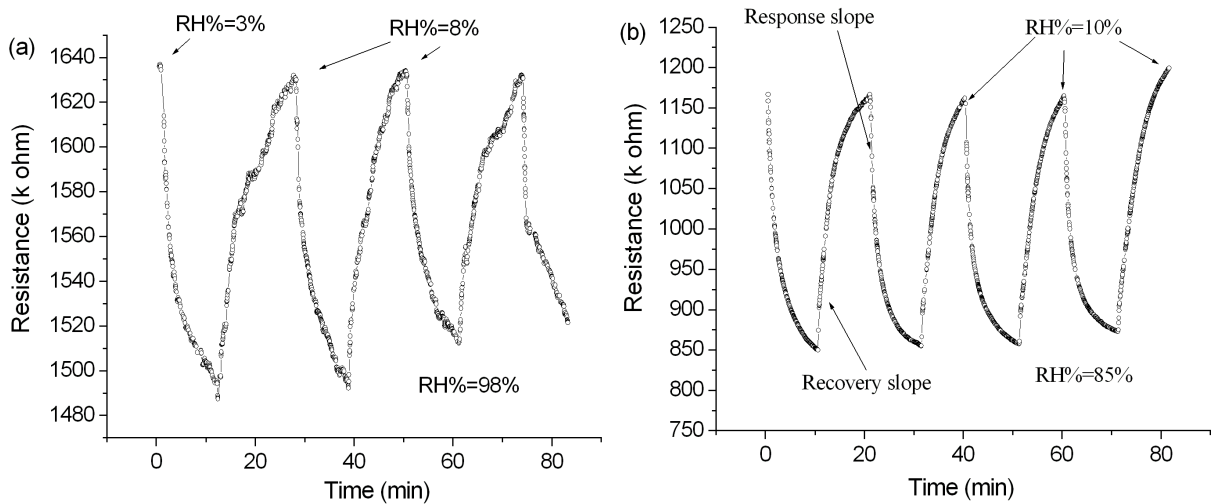


Figure 3.8: Repeatability test between dry air and saturated air, each step is maintained for 10-12 minutes: (a) heterostructure; (b) self-supporting membrane.

From these results, we can conclude that the heterostructure and self-supporting membrane of ordered macroporous silicon show very similar sensing characteristics. There is no significant difference in the response and recovery behavior between these two structures. Therefore, if higher sensitivity can be obtained by modifying the macroporous silicon, it is possible to build a humidity sensor with very simple fabrication process.

3.4 Surface modification of ordered macroporous silicon

As discussed in former sections, the gas/humidity sensing property of PS is highly dependent on the interface surface condition. For the second generation of sensors, the effect of SiO₂, ZnO and HfO₂ thin film coating on the sensing property are studied. SiO₂ can cause the hydrophobic nature of PS to become hydrophilic. Nanostructure ZnO as a metal oxide has been investigated widely for their gas sensing property. HfO₂ is a new material. So far, most of the research is on the application of HfO₂ thin film in CMOS as a promising alternative of SiO₂ [62, 63]. HfO₂ thin film is also investigated as a sensing dielectric for pH detection [64, 65]. Steele et al. [66] reported the humidity sensing response of nanostructured TiO₂. Since hafnium (Hf) and titanium (Ti) are from the same group of the Period Table and chemically similar, sensitivity enhancement of HfO₂ on PS can be expected.

Since we demonstrated the similar humidity sensing characteristics of the heterostructure and self-supporting membrane, the heterostructure is used to simplify the fabrication. Three different heterostructure samples are fabricated with different pore parameters as the substrate, as shown in Table 3.1. After pore formation, they are cleaved into quarters and each quarter has a different surface coating. The four different coatings are as follow: (i) original macroporous silicon from section IV; (ii) macroporous silicon with 100 nm SiO₂ grown through thermal oxidation; (iii) macroporous silicon with 100 nm ZnO thin film deposited by atomic layer deposition (ALD); and (iv) macroporous silicon with 100 nm HfO₂ thin film deposited by ALD.

To obtain a better electrode contact and electrical stability, Al electrodes dots with a diameter of 2 mm and thickness of 250 nm are deposited onto the surface of the macro-

porous silicon by evaporation. Wire connections are made by soldering and the chips are taped to a plastic holder to be protected from damage.

Table 3.1: Pore parameters of three different macroporous silicon heterostructure samples.

Sample*	Pore Diameter (μm)	Pore Distance (μm)	Lattice	Pore Depth	Porosity (%)	Surface Area (μm^2)
T200	4	6	Triangular	200	40.3	2513.27
S200	1	2	Square	200	19.6	628.32
S100	1	2	Square	100	19.6	314.16

* The sample names of T200, S100, and S200 will be all refer to HfO_2 coated ordered macroporous silicon in Section 4.5.

All samples are tested under the same condition as discussed. The resistance response to RH is measured. All three samples with thermally grown SiO_2 (100 nm) coating, irrespective of the pore parameters, show no noticeable response to RH change. The lack of response can be explained by the high resistance of SiO_2 coating samples, due to the thick insulating layer of SiO_2 on surface. Samples with ZnO coating show steady decrease of resistance when RH% increases from 1% to 100%, and recovery when RH decreased from 100%. However, the sensitivity is negligible (approximate 0.4%). This may be due to the inefficiency of ZnO thin film to absorb water molecules, resulting in insufficient amount of water molecules for surface charge change. Samples with native SiO_2 (3 nm) show similar sensing characteristics as the first generation of the sensor.

Among these four different coatings, ordered macroporous silicon with HfO_2 thin film shows improved sensing properties over the ones without coating, which will be discussed in detail in next section.

3.5 Humidity sensor with HfO_2 modified ordered macroporous silicon

3.5.1 Resistance response of HfO_2 modified ordered macroporous silicon

A resistance decrease of the HfO_2 thin film coated sensor under increased RH is observed. Figure 3.9(a) shows the resistance response of T200 to RH change by steps. For each step, RH is maintained at a steady level till the resistance change slowed down. As shown in the figure, the resistance response can be divided into two regions: (I) 0%-93% RH; (II) 93%-100% RH. In both regions, the sensor showed good linear responses to RH and the total *PRV* is 12.7%. In region (I), the sensitivity per 1% RH is 0.09%. In region (II), the sensitivity increase dramatically, but the response remains linear to RH.

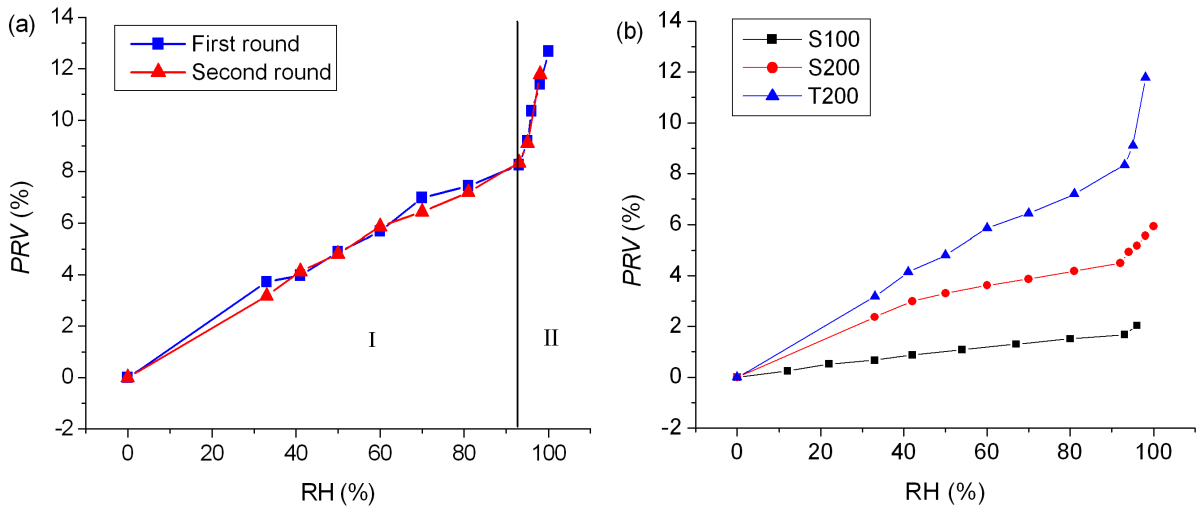


Figure 3.9: Resistance sensing characteristic of HfO_2 modified heterostructure : (a) T200; (b) S100, S200 and T200.

Compared to region (I), the sensitivity per 1% RH is 0.63%, which is 7 times that of region (I). A second round of tests are carried one month later on the same sample and the sensitivity curve coincide perfectly with the first round. The sensor shows good responses in a wide range of RH (0% to 100%). Figure 3.9(b) shows the *PRC*-RH curve of all three samples (S100, S200, T200). All sensors show the same resistance response pattern with two linear regions. The regions are divided at the same RH level.

We believe that the resistance sensing mechanism of HfO₂ Modified sensor is very similar to the unmodified ones. At low humidity level (region I), the resistance decrease is mainly caused by the screening of surface electron traps by adsorbed water molecules. At high RH level (region II), the sudden increase in sensitivity is caused by the formation of multi-layers of physisorbed water molecules, which dissociated into protons and hydroxyl groups under external electric field and results in electrochemical conduction.

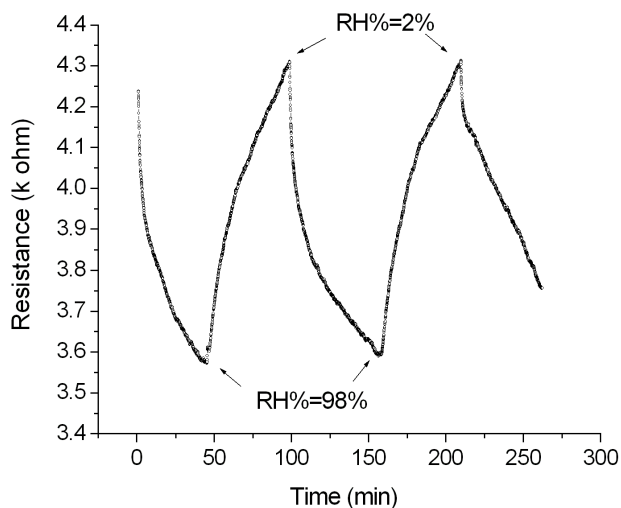


Figure 3.10: Dynamic response of T200 between dry air and saturated air

For repeatability testing, the gas inlet is switched between extra dry air and saturated

air. Figure 3.10 shows the dynamic response of T200 between dry air and saturated air. Each step is maintained for 50-60 minutes. The sensor displays good repeatability. However, the response and recovery time is much longer than the pure silicon samples.

3.5.2 Capacitive response of HfO₂ modified ordered macroporous silicon

The capacitance measurement is carried out under the same condition. The capacitance measurement voltage is 1V and the frequency is 200kHz. An immediate increase of capacitance is observed when RH increased to a higher level. Figure 3.11 (a) shows the capacitance sensitivity of S100 and S200 (different pore length: 100 μm for S100 and 200 μm for S200). 30% *PCV* is obtained for both samples. Their *PCV*-RH curves are perfectly aligned, indicating the same sensing behavior. The response can be considered as approximately linear within the whole RH range. Figure 3.11 (b) shows the linear fit of the *PCV*-RH curve of S200. Figure 3.12 shows the capacitance response of S200 when RH is changed between dry and saturated air. Good repeatability is obtained with capacitance sensing. As we discussed in earlier chapter, the capacitance change of a porous structure upon exposure to moisture is mainly caused by the higher dielectric constant of water than air. This is a difference sensing mechanism with resistance sensors.

Another noticeable phenomenon is the HfO₂ modified sensor's fast sensing of a RH change in the testing chamber. This is observed for both resistance and capacitance measurements. Although it takes longer time for HfO₂ sensors to reach a constant value for each RH change step, it is able to indicate the RH change as soon as it occurred without any delay. As shown in Figure 3.13, the sensing of a RH change of S100 to RH change is

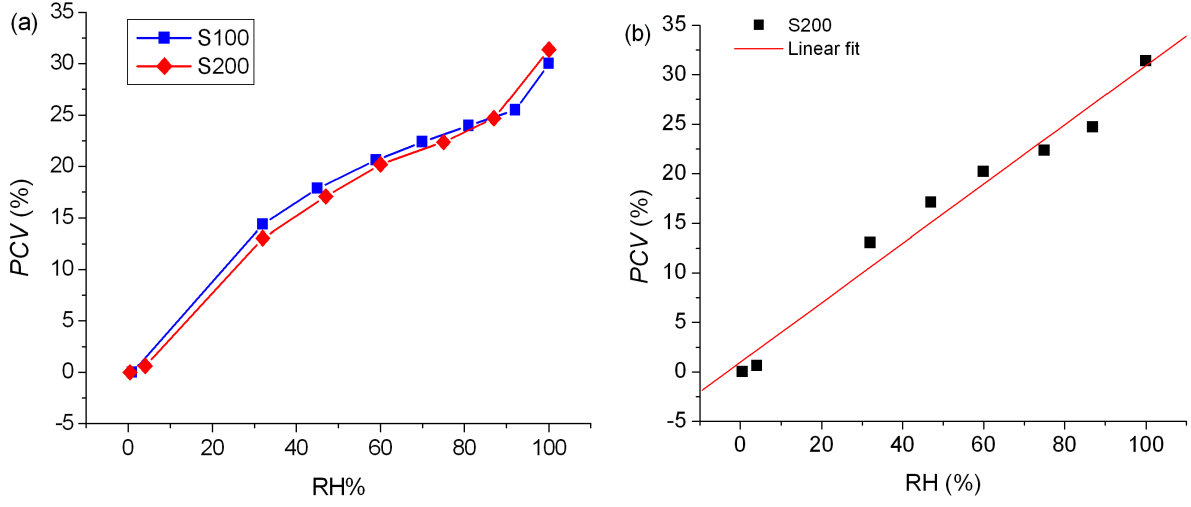


Figure 3.11: (a) Capacitance sensitivity characteristic of S100 (100 μm pore length) and S200 (200 μm pore length); (b) Linear fit of *PCV*-*RH* curve of S200.

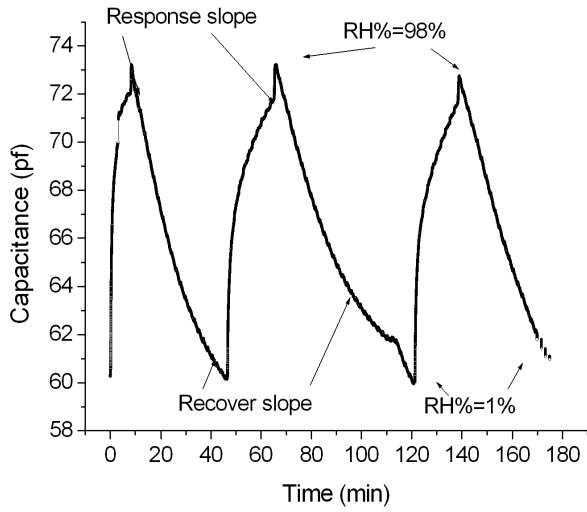


Figure 3.12: Dynamic response of S200 between dry air and saturated air.

obviously faster than that of the commercial reference sensor, for both the increase and decrease cycles. This indicates a promising future for sub-second humidity sensing.

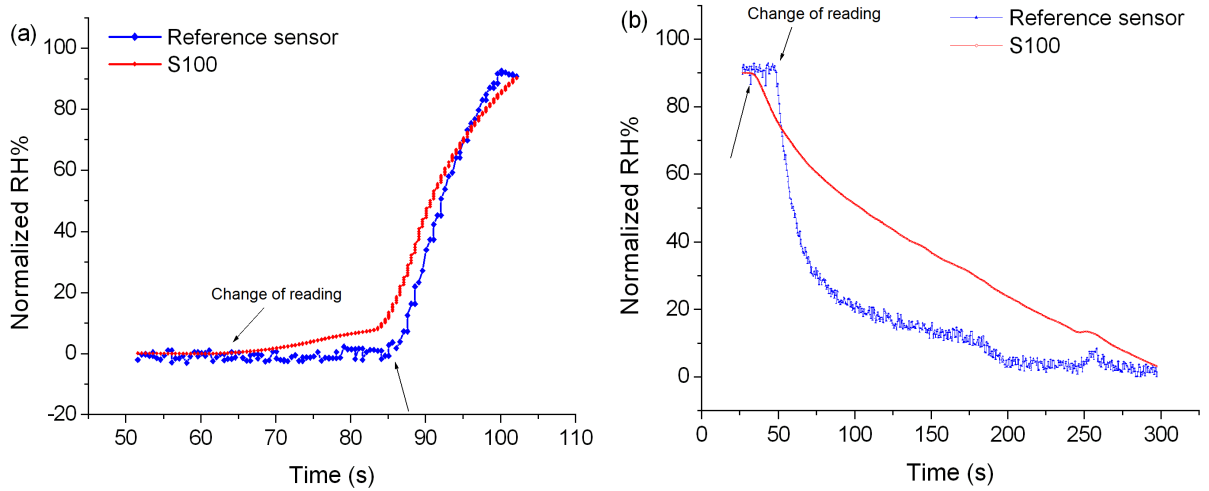


Figure 3.13: Comparison of response time to RH change between S100 and reference sensor: (a) increase of RH, (b) decrease of RH.

3.6 Conclusion

In this chapter, we demonstrate the humidity sensing characteristic of ordered n-type macroporous silicon, with and without surface coating modification. The ordered macroporous silicon has uniform pore size, shape and distribution. The resistance responses of the ordered macroporous silicon heterostructure and self-supporting membrane are tested. A 23-28% decrease in resistance is observed when RH changed from 0% to 100%. Good repeatability is obtained for both structures. The heterostructure showed similar sensing characteristics as the self-supporting membrane, suggesting that a simple fabrication of ordered macroporous silicon humidity sensor is possible.

The effect of the HfO_2 thin film coating on sensor's humidity sensing property is studied

and shows improvements on the sensing characteristic. The heterostructure with HfO₂ thin film coating shows a near-linear capacitance response to a wide range of RH. A high sensitivity and stable performance is obtained. Although it takes a longer time to reach the total reading change, the HfO₂ modified sensor is able to sense the RH change within the testing chamber much faster than the commercial reference sensor.

Chapter 4

Humidity Sensor Based on Ordered Macroporous Silicon with Ta₂O₅ Thin Film Coating

In this chapter, we will introduce the third generation of the devices. The ordered macroporous silicon has a Ta₂O₅ thin film coating and interdigitated electrodes (IDEs) pattern is fabricated on top of sensor by microfabrication techniques. The sensor's humidity sensor property is thoroughly studied. Detailed sensing mechanism and discussions is also provided in this chapter.

4.1 Sensor fabrication

The ordered macroporous silicon is prepared by the same method as introduced in last chapter. The pores have square shape and pore depth of 97 μm . Sensors with pore size of

both $4\ \mu\text{m}$ and $1\ \mu\text{m}$ are fabricated. The $23\ \text{mm}\times 23\ \text{mm}$ sample is cleaved into half. The Ta_2O_5 thin film is then uniformly deposited on the macroporous silicon surface by atomic layer deposition (ALD) and has a thickness of 95 nm. Figure 4.1(a) shows a 3D view of the ordered structure ($4\ \mu\text{m}$ pore size) with perfectly aligned pores and high aspect ratio.

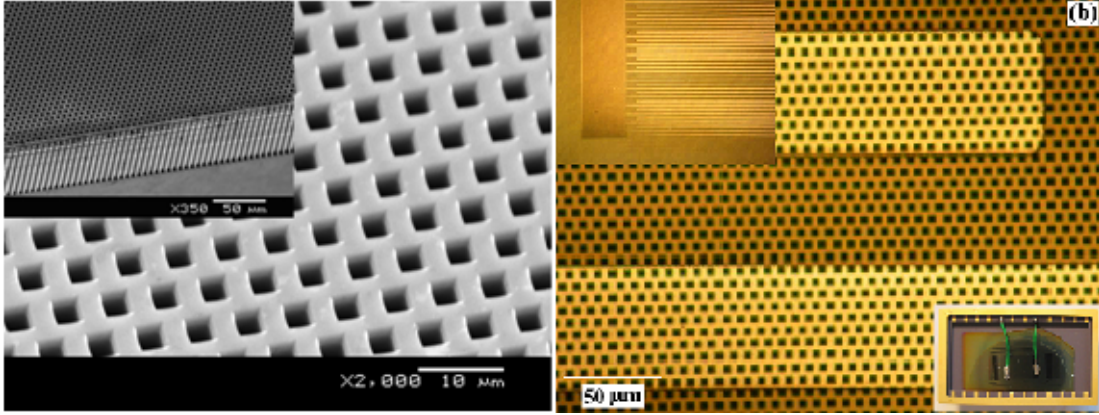


Figure 4.1: (a)SEM image of an ordered macroporous silicon with square pores ($4\ \mu\text{m}$ in diameter), the insert is a SEM image of the 3D structure on silicon substrate (with $97\ \mu\text{m}$ pore length); (b) A microscope image of the Al electrodes on top of the macroporous silicon; the insert (up-left) is a view of the interdigitated electrodes of the sensor; the insert (lower-right) is a image of the fabricated sensor.

The 200 nm Al IDEs are fabricated on top of the sensor by lift-off process. The sensors are then assembled into chip carriers. Figure 4.1(b) shows an image of the IDEs on top of the sensor and a image of the fabricated sensor. For the lift-off process, the thickness of photoresist (PR) needs to be three times of the desired electrodes thickness. Therefore, the PR needs to be at least 600 nm thick. Due to the open pores on the surface, at the same spin speed, the PR on top of the porous area is tens of times thinner that it is on a smooth surface. This is especially true for commonly used thin PR. Take S1818 for instance, at 4000 rpm, the PR is 70-90 nm thick on porous area while it is 1800 nm on smooth surface according to the data sheet. To make sure the porous area is fully covered,

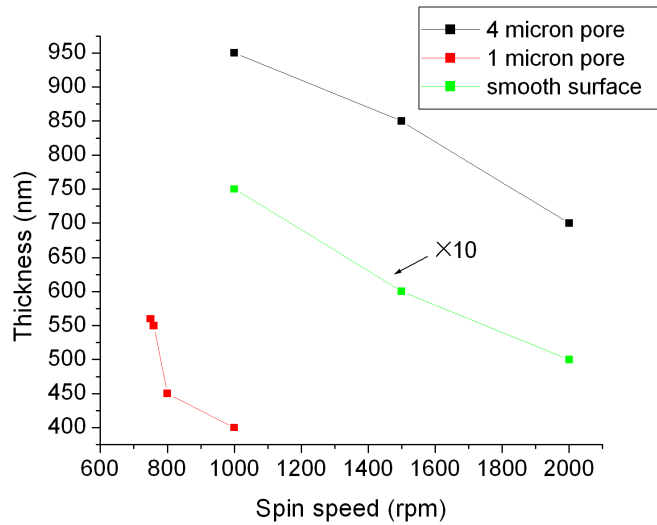


Figure 4.2: Comparison of the PR thickness-spin rate curves of AZP4330 on different surfaces, the data for smooth surface is from the product data sheet.

a thick PR -AZP4330- is used in this experiment. Figure 4.2 shows the comparison of the PR thickness-spin speed curves of AZP4330 on different surfaces. The macroporous silicon with 1 μm pore size has much larger porosity than the one with 4 μm pore size, therefore the PR is even thinner on the 1 μm pore surface.

After the spinning of PR, the coverage of the porous surface can be checked under microscope. Figure 4.3 shows both the partially covered and fully covered surface. Due to the variation of the sample size, the thickness of PR at the same spin rate may vary slightly. Therefore, it is important to constantly check the surface coverage of each sample. MF322 is used as the developer in this process.

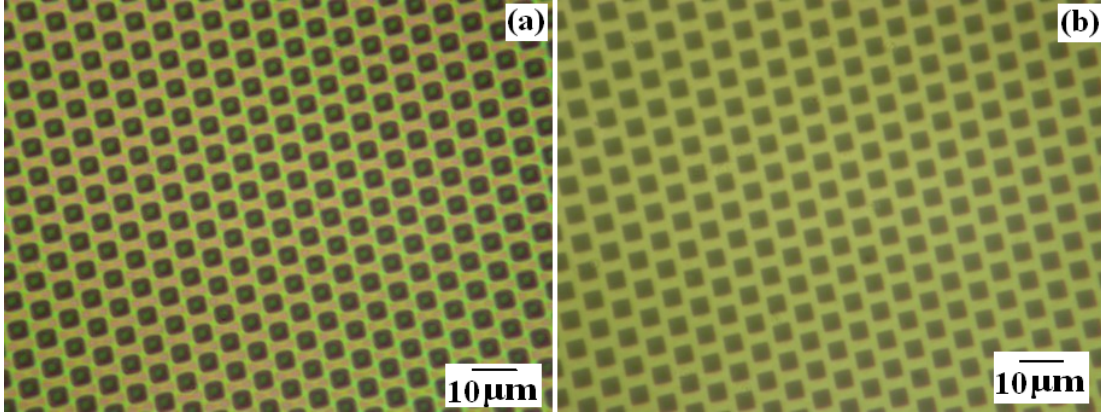


Figure 4.3: Comparison of the porous area coverage by PR under different spin rate: (a) partially covered surface, (b) fully covered surface.

4.2 Humidity sensing at room temperature

4.2.1 Sensitivity

Capacitance measurement is performed to evaluate the sensor's behavior to humidity changes. All the results are from the sensor with $4 \mu\text{m}$ pore size unless specified. The measurement voltage is 1 V. The measurement frequency ranges from 100 Hz to 200 kHz. The sensor's capacitance is measured by changing RH from 0% to 100% in incremental steps. Each step is maintained at a constant value till the capacitance reading reaches a steady value. Figure 4.4 shows the sensor's capacitance response to RH. Figure 4.4(a) shows the *PCV* response to RH changes, while Figure 4.4(b) shows the actual capacitance variations to RH changes. As observed in Figure 4.4, the sensor's capacitance increases significantly with increasing RH at all measuring frequencies, especially at high RH. When RH increases from 0% to 64%, the *PCV* is within the same range (17%-23%) for all frequencies. As the RH continues to increase, the sensor shows larger *PCV* under lower operation frequency. The sensor showed the highest overall *PCV* at 1kHz, which is 297.5% from 0%

to 100% RH. The lowest overall *PCV* is 59.6% at 200 kHz. The reason for the *PCV* differences at different operation frequencies is due to the existence of parasitic capacitance. This will be discussed in a later section.

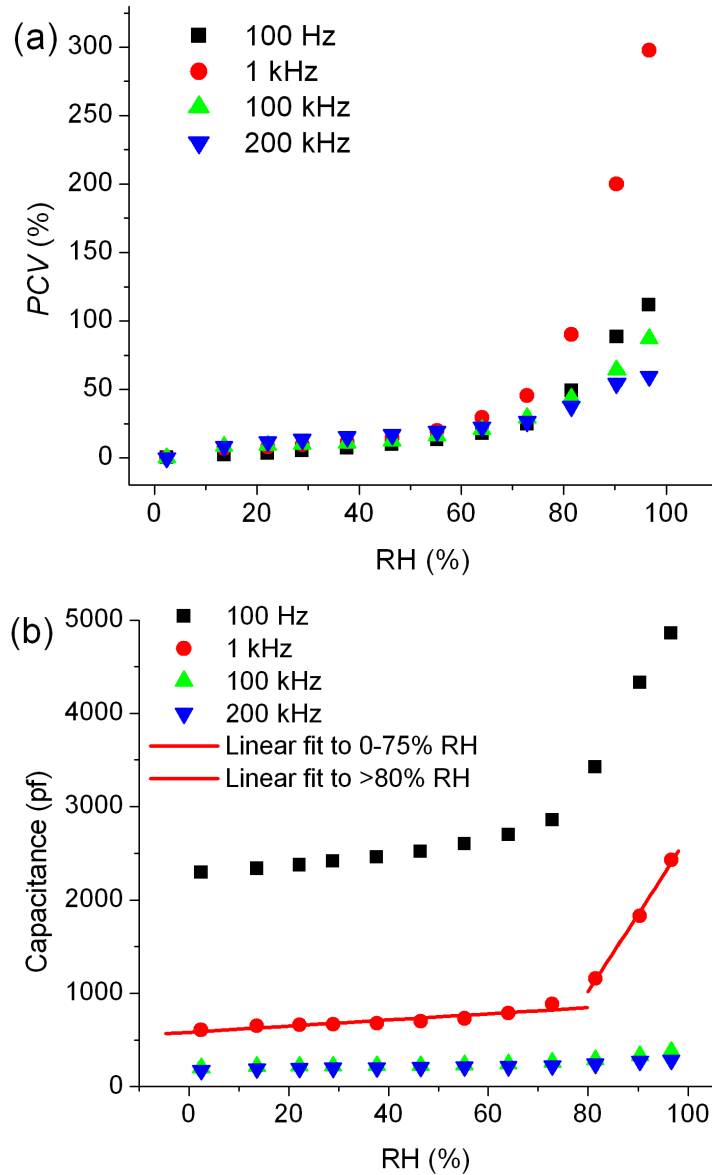


Figure 4.4: (a) *PCV*-RH curve and (b) *C*-RH curve at different measurement frequencies.

Although the *C*-RH curves are not linear in the full RH range from 0% to 100%, the

curves can be divided into two regions: 0%-75% RH and 80%-100% RH. In both regions, the sensor exhibits very good linearity. In Figure 4.4(b), it shows the linear fit curves of the experiment data measured at 1 kHz in these two regions. To perform the linear fit, we set the confidence interval to be 95%. The results show that the correlation coefficient (R) is 0.921 and 0.998 for region 0%-75% and region 80%-100% respectively. The p-value (probability that R is zero) is 4.2E-4 and 0.04 respectively, indicating very good linearity of the data. The sensor's sensitivity at 1 kHz is 3.3 pf/RH in the 0%-75% region and 83.2 pf/RH in the 80%-100% region.

4.2.2 Response time

One important parameter to assess humidity sensors or any other chemical sensors is the response time. Figure 4.5(a) demonstrates the sensor's dynamic responses to cycle changes of RH between extra dry air and saturated air at different measuring frequencies. To compare the performance of the sensor at different frequencies, each step is maintained for 20 minutes. The sensor showed very good repeatability from cycle to cycle at all frequencies. An immediate change of the capacitance is observed during both increasing and decreasing RH cycles. We observed that the sensor had different response time under different frequencies. Comparing Figure 4.4(a) and Figure 4.4(a), at a measuring frequency of 100 Hz, 100 kHz and 200 kHz, the sensor reaches its maximum *PCV* within the 20 minutes after the RH level increases from 0% to 100%. However, when operating at 1kHz, the sensor's *PCV* reaches 153.5% in 20 minutes while its maximum *PCV* at 100% RH is 297.5%. This means the sensor has a much longer response time when operating at 1 kHz.

It has been demonstrated that, capacitance/impedance measurements can truly reflect and monitor the actual state of the adsorption or desorption process in a porous

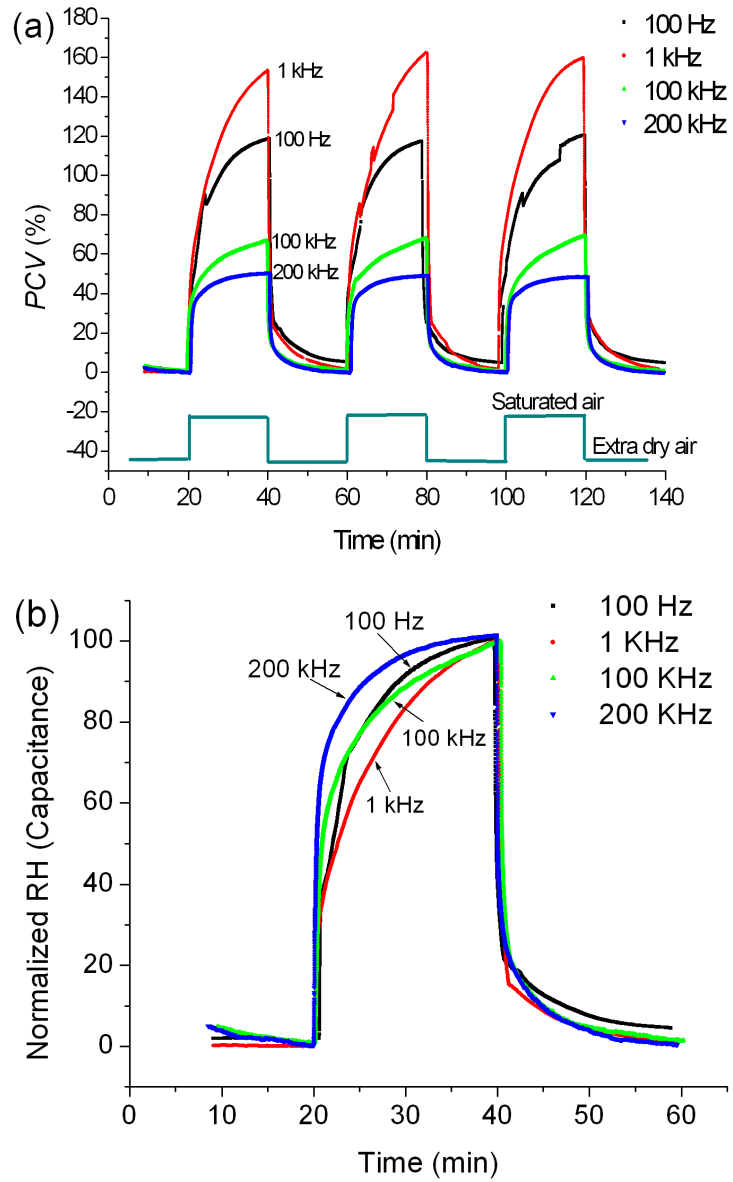


Figure 4.5: (a) Dynamic capacitance response between extra dry and saturated air at different test frequencies, (b) Normalized dynamic capacitance response between extra dry and saturated air at different test frequencies.

sorbent [67]. To compare the ad-/desorption process at different measuring frequencies more clearly, Figure 4.5(b) shows the normalized dynamic response of one of the cycles in Figure 4.5(a). While the desorption processes followed a very similar path at different frequencies, the adsorption processes varied significantly. The adsorption slows down much earlier at 1 kHz. This observation has been confirmed by repeated results. To better understand this phenomenon, the dynamic impedance response of the sensor is also measured with the same LRC meter at different frequencies. Figure 4.6(a) shows the normalized dynamic impedance response at different frequencies when RH increases from 0% to 100%. While the capacitance of the sensor increases with increasing RH levels, its impedance decreases [68]. However, the sensor showed a very similar adsorption path with the capacitance response at each frequency. The sensor always showed the fastest response time (the time that the sensor takes to achieve 90% of the total change) at 200 kHz. The sensor with a 1 μm pore size also showed the same frequency dependency of response time, as shown in Figure 4.6(b).

At the moment, the mechanism behind this response time-frequency dependency observation is not completely clear yet. It has been proven that external electric field can affect the molecule's (both polar and non-polar) adsorption on the sorbent surface [69, 70]. Kunishima et. al [71] found that Cl_2 adsorption on SnO_2 film is much faster under negative bias voltage than that under positive bias or no bias voltage. We also tested the capacitance response of the sensor at the same frequency but with different AC voltages, as shown in Figure 4.7. We can see that the sensor's capacitance variation and sensitivity is slightly different under different voltages, indicating the effect of external electric field on the sensing behavior. We believe that the alternating electric field not only affect the interactions between the water molecules and the sorbent surface, but also the interactions

between the adsorbed molecules. As a result, the sensor showed different adsorption behavior at different frequencies and AC voltage. Figure 4.8(a) and (b) shows the sensor's normalized capacitance response to RH changes between 0% and 38%, and between 0% and 73% at three different frequencies. It can be seen that the differences in the adsorption paths are much smaller at low RH level. Since the differences in adsorption path are more pronounced at high RH levels, where multiple layers of water molecules are formed, the effect on the interactions between adsorbed water molecules seems to be more dominating. Further investigation is needed to fully understand this phenomenon. It is noticeable that the dynamic curves to the changes between 0% RH and 73% RH in Figure 4.8(b) is slightly different from the other dynamic curves. The change of the capacitance slows in the middle and then accelerates again. We believe this is where the surface is fully covered with water molecules and multiple layers of molecules starts to form. This also results in the increase of the sensor's sensitivity at high RH region.

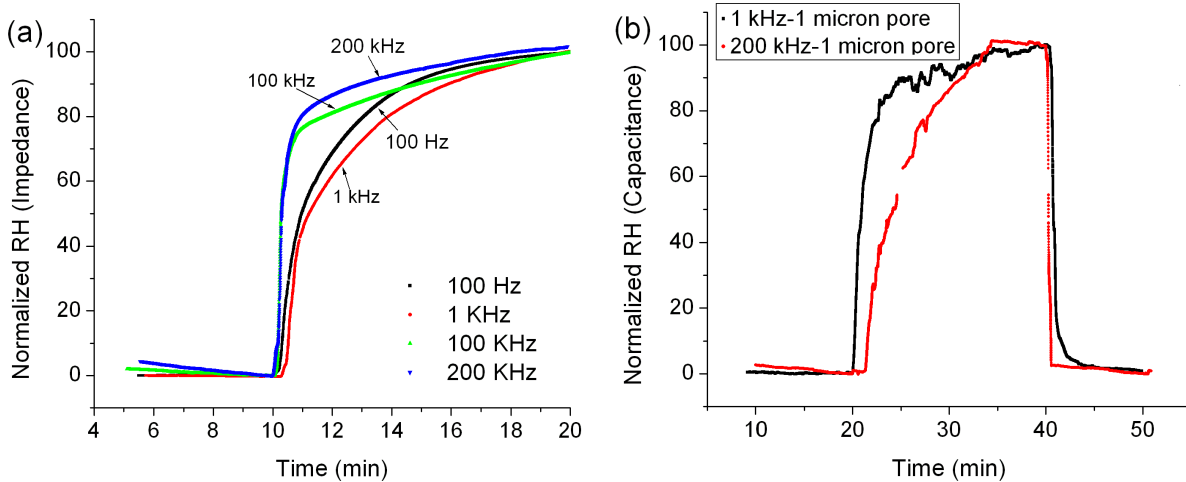


Figure 4.6: (a) Normalized dynamic impedance response between extra dry and saturated air at different measuring frequencies. (b) Normalized dynamic capacitance response between extra dry and saturated air at different test frequencies (sensor with 1 μm pore size).

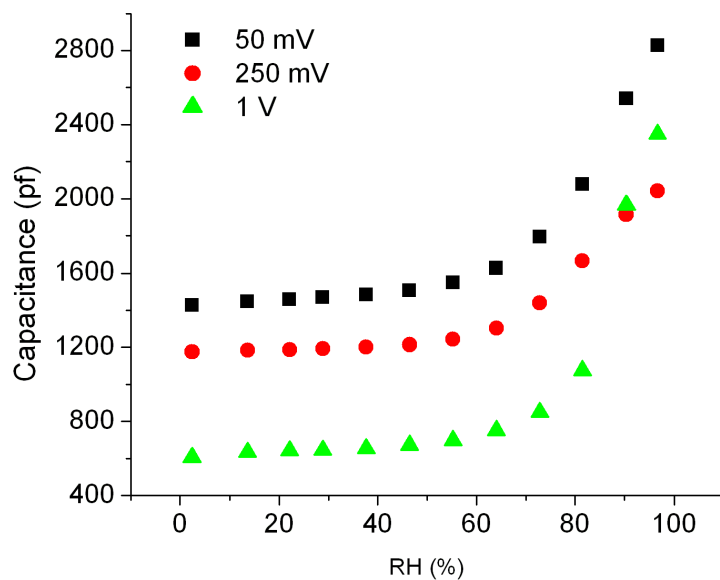


Figure 4.7: Capacitance response at different measurement voltage (1 V, 50 mV and 250 mV) at 1 kHz.

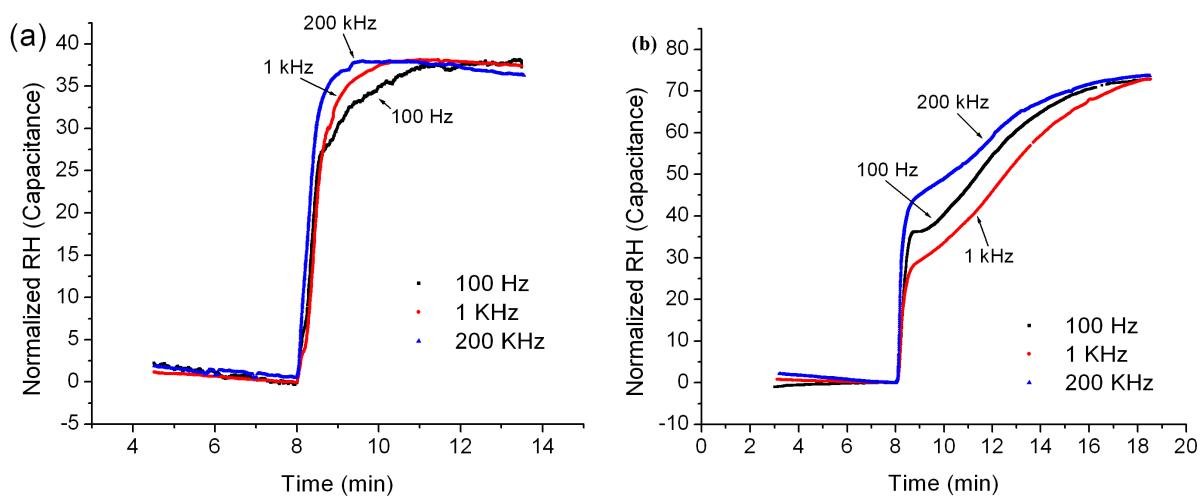


Figure 4.8: (a) Dynamic capacitive response to RH changes between 0% and 38%, (b) dynamic capacitive response to RH changes between 0% and 73%.

Figure 4.9(a) shows the dynamic capacitance response of the sensor between 0% RH and different RH levels at 200 kHz. When the RH increases from 0% to 22%, the sensor reaches 90% of the total change in 18 seconds. When RH increases from 0% to a higher RH, the response time slightly increases accordingly. Figure 4.9(b) shows the corresponding dynamic response of the reference sensor at the same time. The number above each RH level is its respective response time at each stage. It can be seen that the reference sensor also has a similar dependency. Figure 4.9(c) showed the linear relationship of the sensor's response time to the *PCV* corresponding to the RH level in Figure 4.9(a). We believe that there are two factors effecting the response time dependency on the RH change. The main factor is the time required to reach the desired RH level in the chamber. Since the RH in the environmental chamber is changed by flowing dry or wet air, the RH does not reach the desired level immediately. With higher change of the RH level, the chamber needs longer time to stabilize to the new RH level. Another factor is related to the nature of the diffusion and adsorption process. When the RH changes to a higher level, there are more water molecules to diffuse into the structure and adsorb onto the sensing surface. This results in both higher capacitance change and longer response time. This is especially true for our sensor, where the porous structure is 97 μm thick. In this case, the diffusion can be the critical process that cause the long response time. Since the sensor show similar response time with the commercial reference sensor at each stage, we can conclude that this macroporous silicon sensor is very competitive with the commercial sensor (response time is 15 second according to data sheet) in terms of response time.

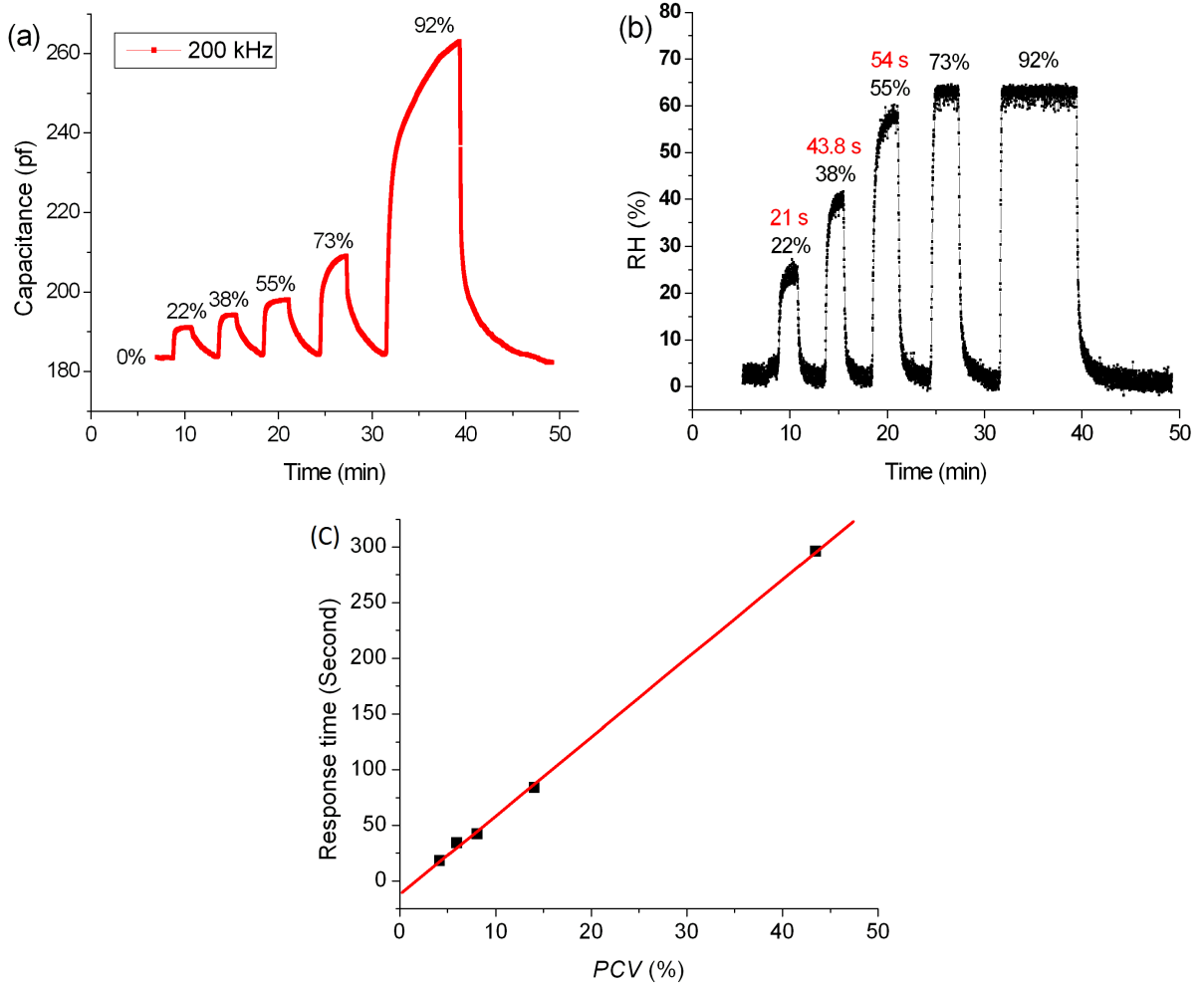


Figure 4.9: (a) Dynamic response of the sensor to different RH% levels at 200 kHz; (b) Corresponding dynamic response of the reference sensor; (c) the relationship of the response time from 0% to certain RH level to *PCV* under 200 kHz.

4.2.3 High humidity level and flooding sensing

While our sensor shows a competitive response time with the commercial sensor, it clearly shows significant advantage on high humidity level sensing. Comparing Figure 4.9 (a) and (b), we can see that the ordered macroporous sensor's capacitance keeps increasing with increasing the wet air to dry air ratio at high RH levels, while the reference sensor's reading stops changing at a fix level. For 73% and 92% RH, we can see the reference sensor showed 63% for both RH level. The reference commercial sensor is calibrated at its manufacturer's settings. We tested two of the commercial sensors and both showed the same response at high RH. This confirms the capability of our sensor for high humidity sensing.

The sensor's behavior is further tested with finer RH steps at high humidity level. Figure 4.10(a) shows the Capacitance-RH curve between 80%-100% RH with 6 steps at 200 kHz. The sensor showed perfect linearity and high resolution over this range. The sensitivity in this range is 3.2 pf/RH at 200 kHz.

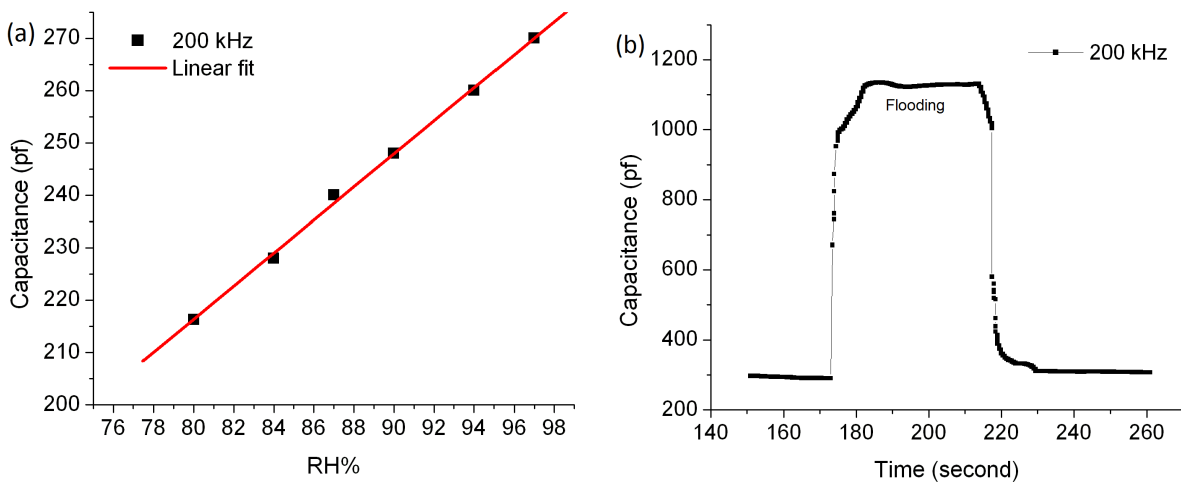


Figure 4.10: (a) The C-RH curve between 80%-100% RH at 200 kHz; (b) Dynamic response of the sensor to flooding condition.

As introduced in Chapter 1, flooding is a common issue in PEMFCs. Therefore, it is very important for the sensor to be able to survive liquid water flooding. To verify this, the sensor is tested outside the chamber where water is dropped on the sensor's surface manually to simulate the flooding situation. For drying cycle, a tissue is used to absorb the surface water and compressed air is used to blow dry the sensor. Figure 4.10(b) shows the sensor's dynamic capacitance response to flooding situations. The sensor showed over 400% percentage variation at flooding condition, which is 8 times larger than the *PCV* at 100% RH. At the same time, the sensor showed very fast response time (25 seconds) to flooding and completely recovered in 5 seconds once the sensor was dried. The sensor cannot only operate properly during and after the flooding, but it is also be able to indicate the existence of liquid water by its capacitance reading. The sensor demonstrates huge potential for fuel cell application in terms of high humidity level sensing.

4.2.4 Stability and hysteresis

The sensor was stored in air at room temperature for several months before the electrode fabrication and is tested repeatedly under different RH levels for more than ten months. The sensor was predominately tested at high RH levels. During the test, the sensor showed very good stability and repeatability. Figure 4.11 shows the C-RH curves at 200 kHz for two round tests which are performed on two different days. The data has very good consistency. This is also observed for the other frequencies.

Hysteresis is another common issue with gas sensors. The sensor was tested with increasing and decreasing RH steps and shows very small hysteresis as shown in both Figure 4.11 (a) and (b). The hysteresis is 0.3%-3.3% over the whole RH range at 200kHz.

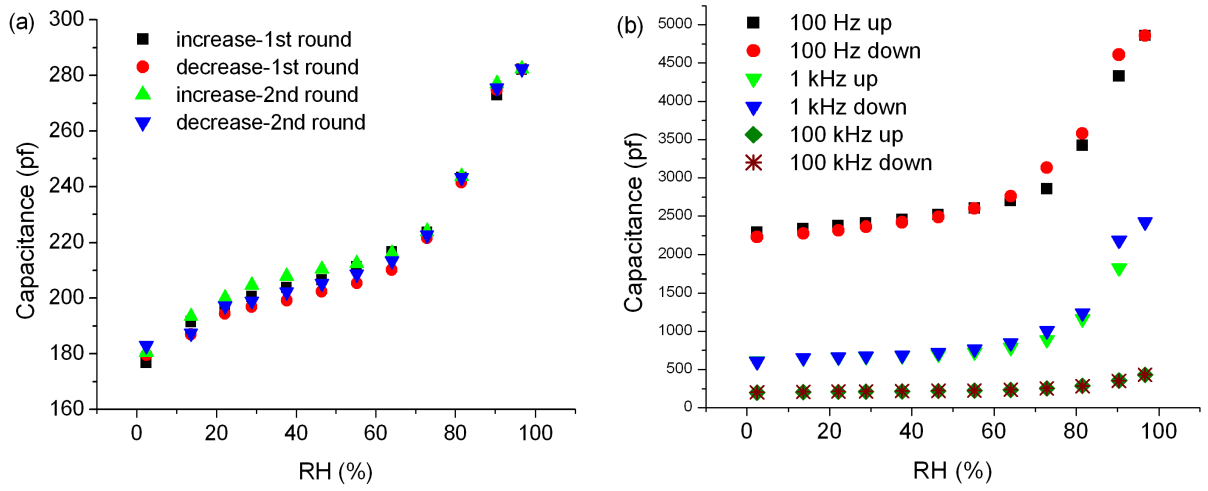


Figure 4.11: (a) The capacitance-RH curve with step up and step down RH changes at 200 kHz; (b) The capacitance-RH curve with step up and step down RH changes at 100 Hz, 1 kHz and 100 kHz.

4.3 High temperature sensing

Since the target application of our sensor is in PEMFC, it is very important to characterize the sensor's behavior at elevated temperature. Figure 4.12 shows the sensor's capacitance dependency on environment temperature (T) at 0% RH. The tests were done on two different days. The sensor's capacitance increased with increasing T. The response was fast and stable. This opens up the possibility of designing the humidity sensor and a temperature sensor with the same sensing material on the same chip.

The sensor's capacitance response to different RH levels at elevated T is shown in Figure 4.13. The sensor retains its high sensitivity at high T. The overall PCV at 200 kHz is still in the range of 42% to 50% while it is 59.6% at room temperature (RT). Compared to the sensing behavior at RT, there is not a sudden increase in sensitivity at high RH in the C-RH curves at high T. When operating at RT, the sudden increase in sensitivity is

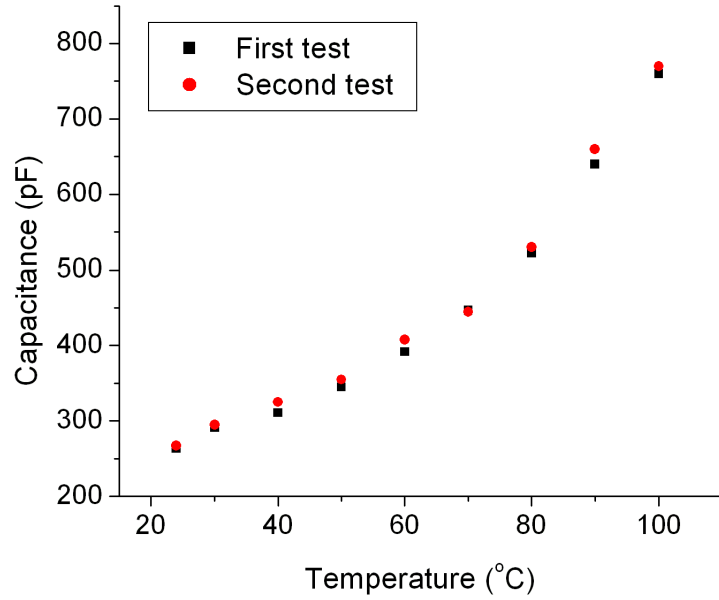


Figure 4.12: The sensor's capacitance dependency on temperature at 0% RH at 200 kHz.

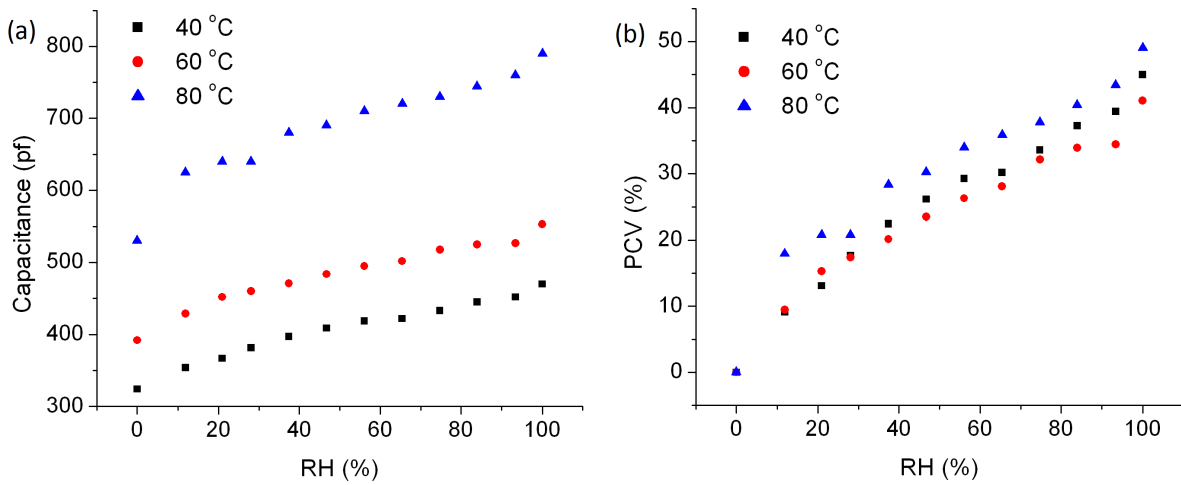


Figure 4.13: (a) Capacitance-RH curve at 40 °C, 60 °C, 80 °C at 200 kHz; (b) *PCV*-RH curve at 40 °C, 60 °C, 80 °C at 200 kHz.

caused by the formation of multilayers of adsorbed water molecules. However, at elevated T, the water content in air is higher at each RH level, resulting in higher sensitivity at low RH. Also, the desorption rate of water molecules is accelerated, leading to difficulty in multiple layers formation. This explains the good linearity over the full RH range at high T.

4.4 Discussions

4.4.1 The sensing mechanisms

The capacitance response of porous structures is often attributed to the replacement of air with adsorbed water molecules in the pores [72]. For conventional random aligned PS, it is difficult to build an exact model to represent the structure. Rittersma and Benecke [73] used a simple model that considers random PS layers as a uniform network of partly oxidized Si nanowires and voids, as shown in Figure 4.14. This is very similar to the order macroporous structure that is used in this experiment, except for the pores which are not connected with each other.

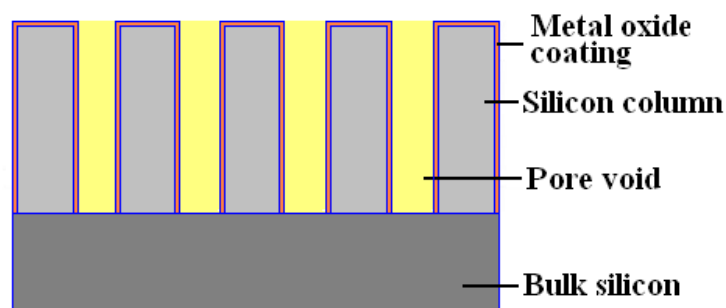


Figure 4.14: The structure of ordered macroporous silicon with metal oxides thin film coating on the surface.

The effective dielectric constant of this n-phase mixture can be described by the generalized effective medium approximation (GEMA) as [74]

$$\sum_{i=1}^n \frac{\epsilon_i^{\frac{1}{t}} - \epsilon_m^{\frac{1}{t}}}{\epsilon_i^{\frac{1}{t}} + \left(\frac{\varphi_P}{1-\varphi_P}\right)\epsilon_m^{\frac{1}{t}}} = 0 \quad (4.1)$$

Where ϵ_m is the dielectric constant of the mixture, ϵ_i is the dielectric constant of the phase i which has a volume fraction of v_i , φ_P is the percolation volume fraction and t is the non-linearity correction factor. Applying GEMA to the order PS dielectric layer as shown in Figure 4.14, its effective dielectric constant (ϵ_{ps}) can be expressed as

$$v_{Si} \frac{\epsilon_{Si}^{\frac{1}{t}} - \epsilon_{PS}^{\frac{1}{t}}}{\epsilon_{Si}^{\frac{1}{t}} + \left(\frac{\varphi_P}{1-\varphi_P}\right)\epsilon_{PS}^{\frac{1}{t}}} + v_{MO} \frac{\epsilon_{MO}^{\frac{1}{t}} - \epsilon_{PS}^{\frac{1}{t}}}{\epsilon_{MO}^{\frac{1}{t}} + \left(\frac{\varphi_P}{1-\varphi_P}\right)\epsilon_{PS}^{\frac{1}{t}}} + v_A \frac{\epsilon_A^{\frac{1}{t}} - \epsilon_{PS}^{\frac{1}{t}}}{\epsilon_A^{\frac{1}{t}} + \left(\frac{\varphi_P}{1-\varphi_P}\right)\epsilon_{PS}^{\frac{1}{t}}} = 0 \quad (4.2)$$

Where ϵ_{Si} , ϵ_{MO} , and ϵ_A are the respective dielectric constants of the silicon, metal oxide and air that fills the pore voids; while v_{Si} , v_{MO} , and v_A are the fractional volumes respectively.

When the PS is exposed to water vapor, water molecules will be adsorbed on the metal oxide surface. For most metal oxides, both chemisorption and physical adsorption occur upon exposure to moisture [75]. At low RH, a monolayer of water molecules is initially chemisorbed due to the electron vacancies on the surface. As the RH increases, layers of physical adsorbed water molecule continue to build up on the chemisorbed layer. Since the pore size of the PS in this experiment is much larger than the Kelvin radius [76], no capillary condensation will occur at high RH levels. Therefore, when RH decreases, desorption of water molecules does not require much extra energy. This explains the sensor's very small hysteresis and fast recovery time.

If P is the porosity of the structure, r is the volume ratio of the metal oxide and Si, and φ_w is the fractional volume of the adsorbed water vapor layers on the surface in the pore space, the effective dielectric constant of the ordered macroporous silicon with adsorbed water molecule layers can be expressed as,

$$\frac{1-P}{1+r} \frac{\epsilon_{Si}^{\frac{1}{t}} - \epsilon_{PSw}^{\frac{1}{t}}}{\epsilon_{Si}^{\frac{1}{t}} + \left(\frac{\varphi_p}{1-\varphi_p}\right)\epsilon_{PSw}^{\frac{1}{t}}} + \frac{r(1-P)}{1+r} \frac{\epsilon_{MOw}^{\frac{1}{t}} - \epsilon_{PSw}^{\frac{1}{t}}}{\epsilon_{MOw}^{\frac{1}{t}} + \left(\frac{\varphi_p}{1-\varphi_p}\right)\epsilon_{PSw}^{\frac{1}{t}}} + \quad (4.3)$$

$$\epsilon_w P \frac{\epsilon_w^{\frac{1}{t}} - \epsilon_{PSw}^{\frac{1}{t}}}{\epsilon_w^{\frac{1}{t}} + \left(\frac{\varphi_p}{1-\varphi_p}\right)\epsilon_{PSw}^{\frac{1}{t}}} + (1-\varphi_w) \frac{\epsilon_A^{\frac{1}{t}} - \epsilon_{PSw}^{\frac{1}{t}}}{\epsilon_A^{\frac{1}{t}} + \left(\frac{\varphi_p}{1-\varphi_p}\right)\epsilon_{PSw}^{\frac{1}{t}}} = 0$$

Where ϵ_{MOw} and ϵ_{PSw} are the dielectric constant of the metal oxides and the thin film coated macroporous silicon in moisture environment, and ϵ_w is the dielectric constant of water. When there are layers of adsorbed water vapor in the pore space, φ_w will increase from 0 to 1. Since water has very high dielectric constant at room temperature (80) compare to air (1), the effective dielectric constant of the PS will increase accordingly. Notice here that the dielectric constant of the metal oxide thin film also changes upon exposure to moisture due to their semiconducting nature. This change is related to the resistance change of the material and has a small contribution to the response. It is also shown in equation 4.3 that the dependence of capacitance on RH can be controlled by adjusting the porosity of the ordered macroporous silicon and the thickness of the metal oxide layer.

4.4.2 Parasitic resistance and capacitance

The dependence of the capacitance variation on the measurement frequency can be explained by the existence of parasitic capacitance and resistance. The parasitic capacitance is generally from the bulk silicon and the interfaces between different layers. It is not affected by the RH change. By lumped modeling, J. Das et al. [72] demonstrated the relationship among the measured capacitance/resistance, the effective capacitance/resistance and the parasitic capacitance/resistance as follows:

$$C_{eq} = \frac{G_1^2 C_2 + G_2^2 C_1 + \omega^2 C_1 C_2 (C_1 + C_2)}{(G_1 + G_2)^2 + \omega^2 (C_1 + C_2)^2} \quad (4.4)$$

$$G_{eq} = \frac{G_1 G_2 (G_1 + G_2) + \omega^2 (C_1^2 G_2 + C_2^2 G_1)}{(G_1 + G_2)^2 + \omega^2 (C_1 + C_2)^2} \quad (4.5)$$

where C_1 , C_2 and C_{eq} represent the effective capacitance, parasitic capacitance and measured capacitance respectively; G_1 , G_2 and G_{eq} represent the effective admittance, parasitic admittance and measured admittance; and ω is the measurement frequency.

At very high frequencies, the measured capacitance is mainly determined by the parasitic capacitance. On the other hand, at low frequencies, the measured capacitance truly represents the active capacitance for humidity sensing. Therefore, the measured capacitance variation is higher at lower operation frequency. This is consistent with our experiment results. The sensor showed the highest capacitance variation at 100 Hz. It is 2563pf at 100 Hz, while the capacitance variation is 1815pf, 176pf, and 105pf at 1 kHz, 100 kHz and 200 kHz respectively.

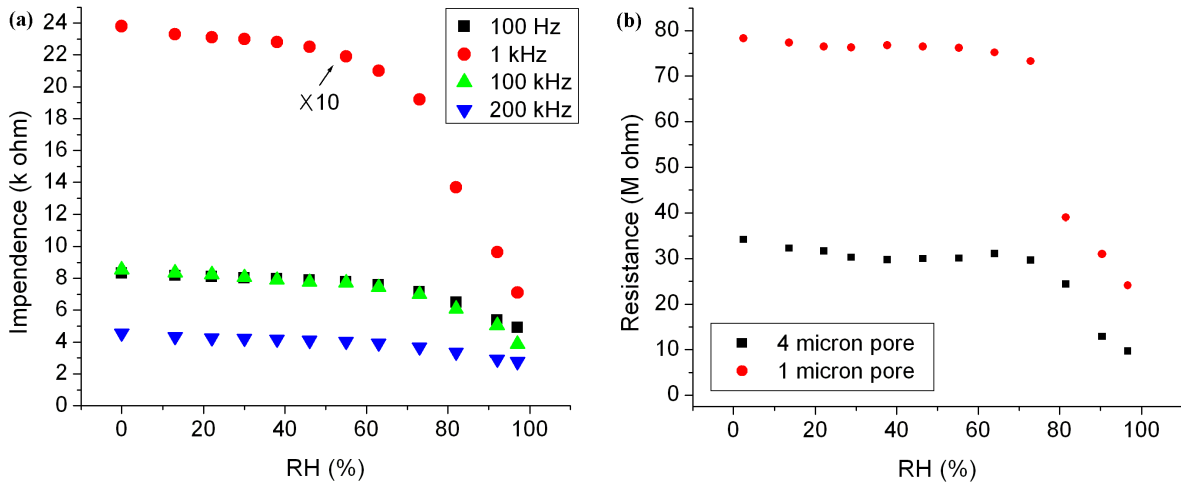


Figure 4.15: (a) Impedance-RH curve at different testing frequency at 1 V; (b) Resistance-RH curve of both 4 μm and 1 μm pore size sensor at 1 V DC.

The same frequency dependency applies to the sensor's impedance response as well, as shown in Figure 4.15(a). Therefore, it is very hard to compare the capacitance/impedance sensing properties of samples with different parameters, unless one can separate the effective capacitance/impedance from the parasitic value. To do this, a measuring instrument that can operate at extremely low and extremely high frequencies is required. However, in the case of impedance response, when the frequency is very low (approaching zero), we have $R_{eq} \approx R_1 + R_2$. Therefore for DC measurements, the measured resistance (R_{eq}) is the sum of the effective resistance (R_1) and parasitic resistance (R_2), hence the change in R_{eq} truly reflects the change in R_1 . This can be used for comparison of sensing properties where parasitic capacitance/resistance is unknown. Figure 4.15(b) shows the resistance vs. RH curves of both 4 μm and 1 μm pore size sensors at 1 V DC. We can see that the sensors showed very similar responses, while the 1 μm pore size showed a much higher resistance change due to its higher porosity and surface area.

4.4.3 Sensing enhancement by thin film coating

The enhancement effect of the Ta_2O_5 thin film coating on the sensor's performance is mainly due to its ultra-hydrophilic property. Figure 4.16(a) and (b) shows the water contact angle of Ta_2O_5 thin film coated silicon surface compare to bare silicon surface (with 3 nm native SiO_2). The Ta_2O_5 thin film coated surface shows a very small contact angle. In last chapter, we reported the sensing properties of ordered macroporous silicon with different surface coatings, including bare Si, thermally grown SiO_2 (100 nm), ALD deposited ZnO (100 nm) and HfO_2 (100 nm) [76]. Table 4.1 gives the comparison of their water contact angle and maximum *PCV* (obtained under different measuring frequencies since there are differences in their parasitic capacitance). It shows that the sensor with coatings that are more hydrophilic have better sensitivities. We believe that the interactions between the adsorbed water molecules and the Ta_2O_5 or HfO_2 coatings also partially contribute to the higher sensitivity. This explains the higher *PCV* of HfO_2 coated sensor than the *PCV* of bare Si sensor, although it has slightly larger contact angle.

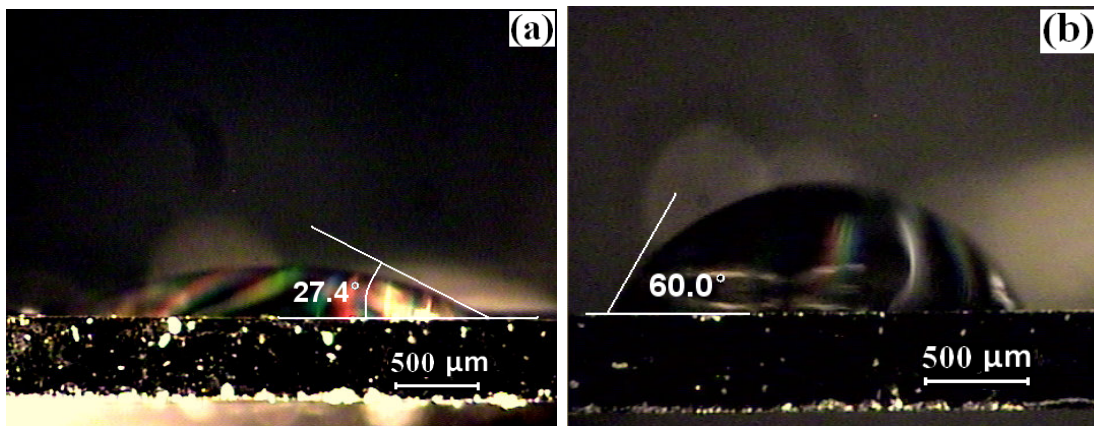


Figure 4.16: Measurement of water contact angle of (a) Ta_2O_5 thin film coated silicon surface, (b) bare silicon surface. The measurement is taken at non-porous area of the sensors in a 3D micro-stage system with horizontally aligned microscope

Table 4.1: Comparison of the water contact angle and *PCV* (%) of ordered macroporous silicon humidity sensor with different surface coatings.

Surface Coating	Contact Angle (°)	PCV (%)
Ta ₂ O ₅	27.4	300
Si	60.0	13.9
HfO ₂	66.5	55
ZnO	80.1	1.8
SiO ₂	88.6	0.36

4.5 Conclusions

We demonstrated the humidity sensing characteristic of a Ta₂O₅ thin film enhanced ordered macroporous silicon humidity sensor at both room temperature and elevated temperature. The sensor shows high sensitivity, fast response, very small hysteresis and long term stability over the whole RH range and up to 80 °C. At room temperature, the sensor’s C-RH relationship shows perfect linearity in two regions respectively over the whole RH range, while the linearity extents to the full RH region at elevated temperature. The sensor’s response time is competitive with commercial humidity sensors, and shows high sensitivity and resolution at high RH level and even flooding condition. Overall, the sensor shows great potential for the application in PEMFCs.

The capacitance change upon exposure to moisture is mainly caused by the replacement of air with adsorbed water molecules in the pore space. Due to the existence of parasitic capacitance, the sensor exhibits a higher capacitance variation values at low frequencies. The sensor shows the fastest response time at 200 kHz. It is believed that this dependency of response time on measuring frequency is caused by the effect of external electric field on

the adsorption process. However, future investigation is need to verify this point.

Chapter 5

Vertically Aligned ZnO Nanorods for Humidity Sensing

In addition to ordered macroporous silicon, well aligned 1D ZnO nanorods/nanowires - another widely used ordered nanostructure in gas sensing- is also investigated as potential humidity sensing materials. With the development of synthesis technique, more and more attention has been attracted to the alignment of 1D structures, which can fully take the advantage of their geometric anisotropy and allows better control of the parameters. In this work, both vertically and laterally aligned ZnO nanorods/nanowires are fabricated and their humidity sensing properties are characterized. To the best of our knowledge, this is the first attempt to use well aligned ZnO nanorods/nanowires for humidity sensing.

5.1 Introduction

Recently, intensive efforts have been put into the exploration of the humidity/gas sensors based on nanostructured materials such as carbon nanotubes [77, 78, 79], porous silica [80], metal oxide nanoparticles [81, 82, 83, 84, 85, 86] and nanowires [87, 88, 89, 90, 91, 92]. Compared to bulk materials, nanostructured materials have ultra-high surface-to-volume ratio, hollow structures, small grain size, very large grain boundary areas and a Debye length comparable to the nanowire radius, which significantly promotes the gas sensing properties.

Metal oxides have been widely used as a main gas sensing material due to its low cost, simplicity and ability to detect a large number of gases [93, 94]. Metal oxide semiconductors, such as SnO_2 , [90] TiO_2 , [89] ZnO , [85, 91, 95] CoFe_2O_4 [92] are all widely used in humidity sensors. The sensing mechanism is mainly based on their resistance dependency on the ambient RH level, which is caused by the modification of the material's surface states upon exposure to water vapor [85, 87, 89, 90, 92].

Among these metal oxides, zinc oxide (ZnO) has attracted substantial research interest due to their distinctive optical, electronic and chemical properties. ZnO is a well-know n-type wide band gap semiconductor that has a wurtzite structure with a band gap of about 3.37 eV and large exciton binding energy of 60 meV [96]. It has a wide range application in various fields, including optoelectronic devices, piezoelectric transducers, transparent conducting film, dye-sensitized solar cell, and solid-state gas sensors [97, 98, 99, 100]. D. C. Look [101] and Ü. Özgür [102] have comprehensively reviewed the properties and applications of ZnO as both bulk and nanostructured materials. By different synthesis techniques, ZnO can be grown into various nanostructures such as nanowires, nanorods,

nanotubes, nanobelts, nanotetrapod and hollow spheres [103, 104, 105, 106, 107, 108]. The nanostructured ZnO have already shown advantages in the electronic, optoelectronic, and optical applications [109, 110]. It also demonstrates its gas sensing capability in a wide range of gases including NO_2 , NH_3 , H_2 , CO , and organic vapors [111, 112, 113]. In some reports, humidity sensors based on ZnO nanostructures such as nanowires and nanorods have shown good sensitivity owing to its high mobility of conduction electrons and good chemical and thermal stability [91, 95, 114].

With the development of synthesis technologies, materials with ordered nanostructures can be realized. In this chapter, we will firstly give some brief background introduction. And then we will explore the synthesis of vertically aligned ZnO nanorods and its potential as a humidity sensing material. The effect of the synthesis parameters on the nanorods' morphology and humidity sensing behavior are studied. During the preparation, the parameters including synthesis source, time, with or without poly(ethyleneimine) (PEI) and post annealing varied to find the optimal process for humidity sensing.

5.1.1 Synthesis methods of aligned nanostructures

The growth methods of 1D nanostructures can be cataloged into vapor phase growth and solution phase growth [115, 116, 117]. The vapor phase growth are performed in a furnace with temperature gradient and the source material is evaporated to the growth site. It can base on two mechanisms: vapor-liquid-solid (VLS) mechanism and vapor-solid (VS) mechanism. The VLS involves the vapor phase precursor, the liquid catalyst droplet and the solid crystalline product, while the VS takes place when the nanostructure originates from the direct condensation of the vapor phase without the use of a catalyst. The solution phase growth is usually carried out at ambient temperature, which significantly reduces

the complexity. This method can be grouped into the template-assisted and template-free method. One of the most common template-free methods is the hydrothermal process, which has been used to produce crystalline structures since the 1970s and is used in this experiment.

To fully take the advantage of the geometric anisotropy of 1D structures, different strategies, such as catalyst patterning, substrate lattice matching by epitaxial growth, template assisted alignment and electric field alignment, are developed to grow vertically or horizontally aligned nanorods/nanowires. In the case of ZnO, both vapor phase growth [118, 119, 120] and solution phase growth [121, 122, 123] have demonstrated the ability for the synthesis of ordered nanostructures. G.Z. Wang et al [124] synthesized aligned hexagonal ZnO nanorods on Si substrate by chemical vapor deposition (CVD). Aligned ZnO nanowires with 100 μm length are achieved by a seed layer catalyzed vapor phase transport method [125]. Hua et al. [121] synthesized 8 μm vertical aligned ZnO nanowires on seed layers used cycle solution method, which is very similar with the technique we use here in this report.

For horizontally alignment of 1D nanostructures, dielectrophoresis (DEP) is the mostly used method [126, 127, 128]. DEP is the electrokinetic motion of dielectric polarized materials in non-uniform electric fields, and is an ideal technique to align and manipulate one-dimensional nanostructures for micro/nanosensors and circuits. Mahmoodi et al. [129] prepared ZnO nanorods by the hydrothermal method in an aqueous solution and then aligned the nanorods between IDEs by DEP for CO sensing. The nanorods link together between the electrodes and bridge the gap. ZnO nanowire based UV photosensor has also been fabricated by DEP [130]. The nanowires were synthesized by vapor deposition and then were suspended in ethanol for DEP assembling. The ZnO nanowires aligned along

the electric field direction and then the solution was evaporated.

5.1.2 Gas sensing mechanisms with metal oxide nanostructures

For semiconducting metal oxide gas sensors, there are many mechanisms that have been proposed to explain the conductivity change of the material in gaseous ambient. For example there is the reduction or oxidation of the sample, anion exchange by a gaseous species, and bonding to the bare surface or bonding to a previously adsorbed species [131].

Most metal oxides gas sensors requires high operation temperature. The change in conductivity attributes to the oxidizing or reducing reactions. For room temperature sensing, the mechanism is generally related to the existence of surface states. It can be defects, excess cations or anions which are the result of the sudden termination of the periodic structure, or adsorbed oxygen [115, 116, 131]. For n-type semiconductors, such as ZnO, upon adsorption of charge accepting molecules, such as NO_2 , O_2 and O_3 , electrons are withdrawn and effectively depleted from the conduction band, leading to a reduction of conductivity. On the other hand, when it is a reducing agent, as CO and H_2 , it injects electrons into the semiconductor, thus increases the conductivity. There is also argument that [116], the conductivity increase is due to the bonding of the gas molecules with the surface adsorbed oxygen and consequently release the captured electrons back to the channel, resulting in an increase in conductance.

A special case is the adsorption of water molecules on metal oxides. So far, most n-type metal oxides show increased conductivity when exposed to humidity. There are several proposed possible mechanisms. The most commonly used one is the dissociation of adsorbed water molecules. When water molecules are adsorbed onto the cation sites of

dry oxides surface, the water will most likely dissociate as hydroxyl groups and form the first chemisorbed layer as the base for further physisorption. When there are no additional layers, proton hopping under applied electrical field is believed to be the main factor for surface conduction. As more layers form, dissociated proton or hydronium ions migrate within the layer. At high humidity level, it's proposed that Grotthuss chain reaction is the dominant mechanism, where some of the H_2O molecules are ionized as H_3O^+ and the extra proton hops from molecule to molecule [132]. When there is condensed water in capillary structures, electrolyte conduction will occur. This succession of mechanisms are believed to be the cause of a rapid increase of conductance with increasing humidity level.

In this work, we investigated the humidity sensing response of well aligned ZnO nanorods and nanowires. Based on our observation, both of the vertically and laterally aligned ZnO 1D structures show decreasing conductivity with increasing humidity level. This is contrary to the other reported works. We will discuss possible mechanism in later sections.

5.2 Synthesis of ZnO nanorods

Aligned ZnO nanorods are synthesized using a hydrothermal method on indium tin oxide (ITO) coated glass substrate [133]. Before the seed layer preparation, ITO substrates were cleaned by detergent, deionized (DI) water, iso-propanol and ethanol. In order to enhance the wetting of the seed layer on ITO substrates, the substrates were irradiated by UV lamp. The contact angle was 8° after UV irradiation. The formation of the seed layer on ITO substrate was conducted using precipitation deposition in ZnO colloid solution. The ZnO colloid solution is synthesized by method proposed by Hoffmann [134]. The size of the ZnO nanoparticles is approximately 5 nm. After ZnO nanoparticles were precipitated on

the ITO substrates, the substrates are annealed in air at 550 °C for 30 minutes in a furnace to enhance the adhesion and crystallization of the ZnO seed layer on ITO substrates. ZnO nanorods are grown on the seed layer using the hydrothermal method in 0.02 M aqueous solution containing the growing source -zinc acetate ($\text{Zn}(\text{Ac})_2$) or zinc nitrate ($\text{Zn}(\text{NO}_3)_2$)- and ammonium hydroxide (28 wt% NH_3 in water, 99.99%) at 95 °C for certain time. PEI can be added to assist growing longer nanorods. After growth, the substrate is removed from the solution, followed by rinsing with DI water, and then dried in air. The length of the ZnO nanorods are controlled by the growth time and long nanorods can be achieved by multi-step growth in the aqueous solution. The as-grown ZnO nanorods can be annealed further in air at 400 – 550 °C for 30-60 minutes to improve the crystallinity of the ZnO nanorods and the interfacial structures. In order to study the effect of post annealing on the humidity sensing property, nanorods with and without post annealing are prepared. Table 5.1 lists the six different kinds of ZnO nanorods that are prepared varying the growing parameters for this experiment, with the sample 1 as the standard process.

Table 5.1: ZnO nanorods samples prepared with varying the growing parameters

Sample	Source	Growth Time (hr)	Adding PEI	Post Annealing
Sample 1	$\text{Zn}(\text{Ac})_2$	4	Yes	Yes
Sample 2	$\text{Zn}(\text{Ac})_2$	10	No	Yes
Sample 3	$\text{Zn}(\text{NO}_3)_2$	10	No	Yes
Sample 4	$\text{Zn}(\text{Ac})_2$	24	Yes	Yes
Sample 5	$\text{Zn}(\text{Ac})_2$	24	No	Yes
Sample 6	$\text{Zn}(\text{Ac})_2$	24	Yes	No

5.3 Characterization of the ZnO nanorods

The ZnO seed layer deposited on UV-treated ITO/glass substrate was shown in Figure 5.1(a). After the precipitation deposition, the substrates were put into the furnace to anneal for enhancing the crystallinity of ZnO seed layer. During the annealing, the temperature ramp is an important factor to control the surface morphology. If anneal temperature rises rapidly, the seed layer will crack due to thermal strain under any firing regime, as shown in Figure 5.1(b).

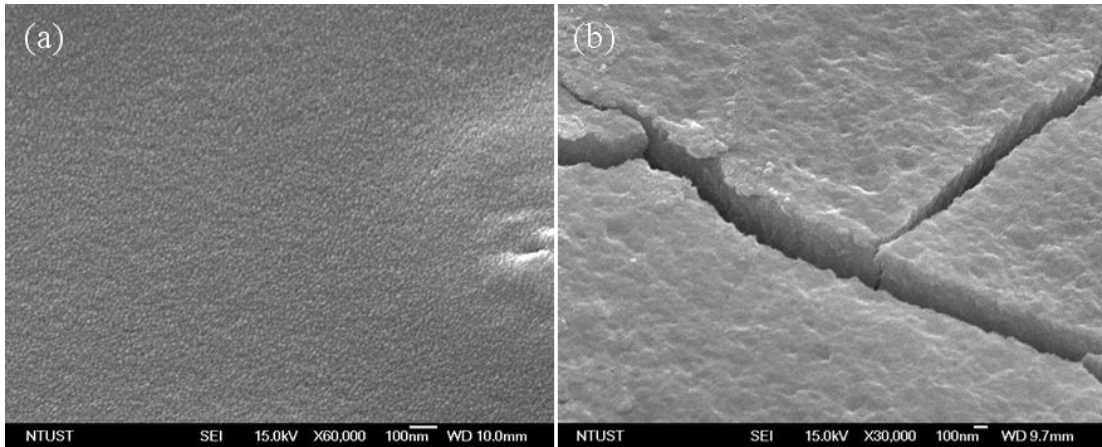


Figure 5.1: ZnO seed layer deposited on ITO/glass substrate with (a) dense surface morphology, and (b) cracked surface morphology. The cracked surface was caused by rapidly temperature ramp in anneal process.

The crystallinity of the annealed ZnO nanorods is investigated using X-ray diffraction (XRD). As shown in Figure 5.2, the aligned ZnO nanorods array that is grown on an annealed seed layer substrate shows a very strong (002) peak, while the other two typical peaks for ZnO (the (100) one and (101) one) are very weak. These results indicate that individual ZnO nanorods only crystallized along the ZnO [0001] direction, which are vertically aligned on the substrate.

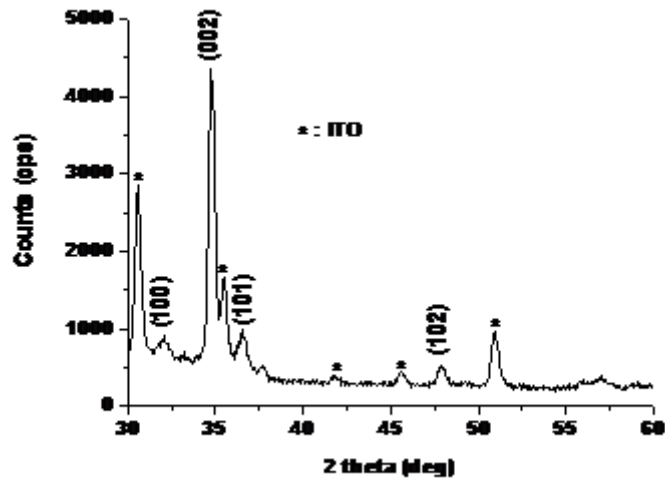


Figure 5.2: X-ray diffraction spectroscopy of the ZnO nanorods that are grown on an annealed seed layer substrate

Figure 5.3 shows the scanning electron microscopy (SEM) images of the ZnO nanorods prepared on ITO/glass with different parameters. A high density of ZnO nanorods grew vertically on the substrate. Depending on the growth condition, the diameters of the nanorods range from 150 nanometers to several hundreds nanometers and the length range from 1 μm to 6.5 μm . Figure 5.3(a), (b) shows the image of sample 1, with $\text{Zn}(\text{Ac})_2$ as zinc source, PEI in the aqueous solution, 4 hours synthesis time and post annealing at 400°C for 30min. The nanorods show uniform helix structure and an average length of 1 micron. Sample 2 (Figure 5.3(c)) and sample 3 (Figure 5.3(d)) are grown for 10 hours with different zinc sources and without PEI. Compared with sample 2, which is grown with $\text{Zn}(\text{Ac})_2$ as source, sample 3 shows a smaller diameter on average when grown with $\text{Zn}(\text{NO}_3)_2$ as a source. PEI is an organic ligand to assist the growing of longer ZnO rods. It will inhibit the radial growth thus the diameter of the ZnO rods will be smaller. This can be seen when comparing sample 1 (Figure 5.3(b)) and sample 2 (Figure 5.3(c)).

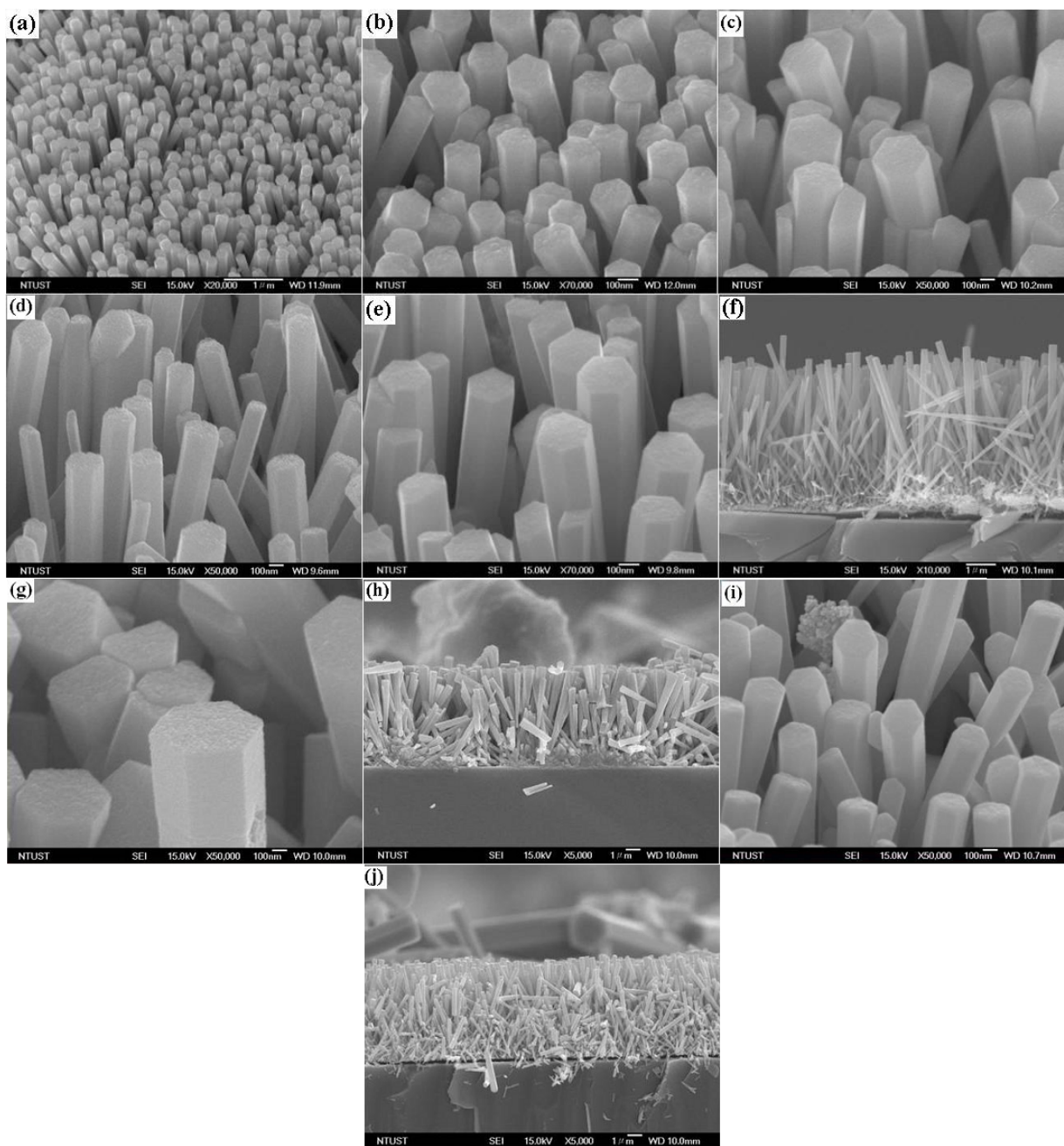


Figure 5.3: SEM images of prepared ZnO nanorods, (a) and (b) sample 1; (c) sample 2; (d) sample 3; (e) and (f) sample 4; (g) and (h) sample 5; (i) and (j) sample 6 e

Sample 2 grown without PEI shows a larger diameter than sample 1. Sample 4 and sample 5 also show the same effect. Comparing sample 4 (Figure 5.3(e)) and sample 5 (Figure 5.3(g)), sample 5 shows a significant increase in the nanorods diameter since no PEI is added during the preparation. Sample 4, 5 and 6 are all grown in $\text{Zn}(\text{Ac})_2$ for 24 hours, which results in longer nanorods (6.5 micron for sample 4 as shown in Figure 5.3 (f)). There is no obvious morphology difference shown in the SEM image between sample 4 and 6. This is because the post annealing process only affects the surface states of the nanorods but not their size and shape. Due to this change in surface state, the humidity sensitivity can be improved significantly, which will be discussed in detail in the next session.

5.4 Humidity sensing results and discussions

The resistance response of the ZnO nanorods mat array to relative humidity change is measured in this experiment. Two electrodes contacts are made at each end of the rectangle nanorods area with Al thin film by conducting epoxy.

To study the influence of the growing condition on the samples' sensing characteristic, their percentage resistance variation (*PRV*) between 0% RH and 100% RH at room temperature are measured and compared. Figure 5.4 shows the comparison of the six samples' resistance variations. From the experiment, it can be concluded from the results that:

- With the increase of humidity level, all samples show increasing resistance.
- The longer nanorods show smaller resistance variation (comparing sample 1, 2 and 4). The reason is not completely clear at this point. There are two possible explanations. One is the lower diffusion efficiency of the water molecules into the nanorods bundle

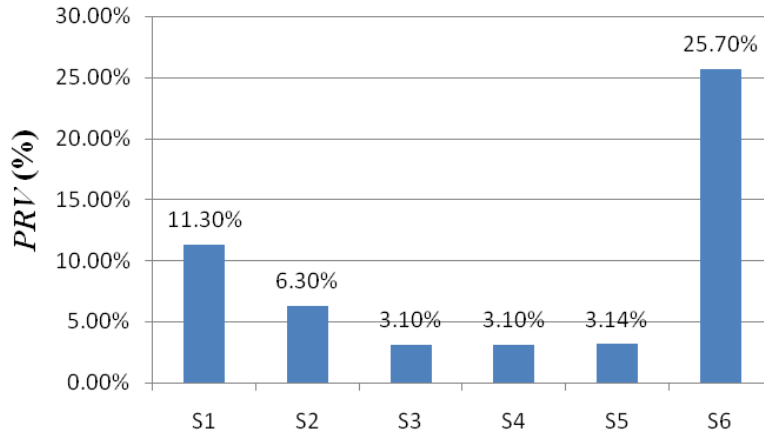


Figure 5.4: Comparison of the different samples' resistance variation between 0% and 100% RH (the results are from fresh samples in the first round test of each sample)

due to the increasing length. Especially when the as-grown aligned nanorods are packed together with a high density, water molecule adsorption may only happen at the top part of the nanorods and thus results in the lower sensitivity. Another possible reason is the longer growth time. The longer growth time not only increases the nanorods' length, but also results in lateral growth. Comparing Figure 5.3(b) and Figure 5.3(e), sample 4 with 24 hours growth time shows a much larger average diameter than sample 2 with 4 hours growth time. This can possibly cause the change in surface states, which is highly related to the humidity sensing capability.

- Comparing sample 2 and 3, it shows that nanorods grown with $\text{Zn}(\text{Ac})_2$ as a zinc source have larger responses to humidity change than those with $\text{Zn}(\text{NO}_3)_2$ as zinc source. The difference between the samples is the counter ions in the aqueous solution during preparation: one is CH_3COO^- (for $\text{Zn}(\text{Ac})_2$) and the other is NO_3^- (for $\text{Zn}(\text{NO}_3)_2$). However, more study is needed to explain the effect of the counter ions on the surface state and humidity sensing property at this point.

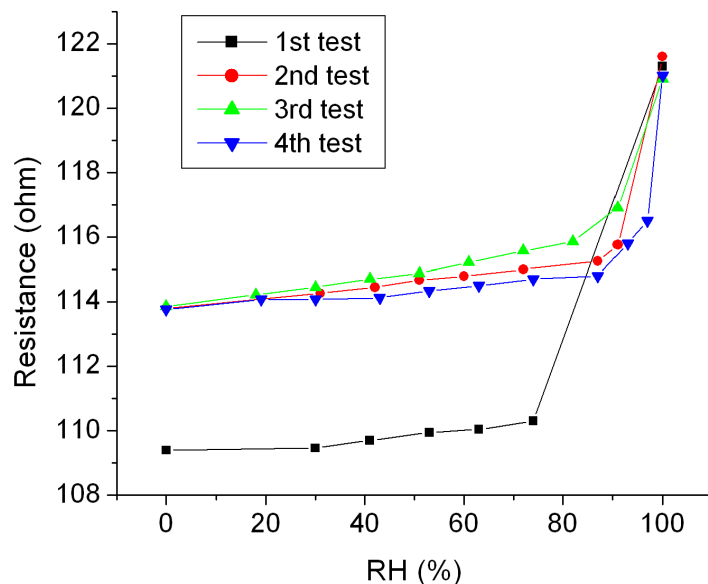


Figure 5.5: Resistance variation-RH of sample 1 at first several round of test

- Comparing sample 4 and 5, we can see that adding PEI during the preparation does not affect the surface state thus the humidity sensitivity of the nanorods.
- The post annealing process has significant effect on the humidity sensing characteristic of the nanorods. Nanorods without post annealing show more than 8 times resistance variation than the annealed nanorods (comparing sample 6 and sample 4).

From the results, we can see that samples 1 and 6 show better and more interesting results. Therefore, more measurements were performed on these two samples. As we tested the sample repeatedly, we observed obvious degradation of the sample. The RH in the chamber is changed step-by-step. For each step, the RH level is kept constant until the resistance reading reached a steady level. Figure 5.5 shows the resistance variation-RH of sample 1 at first several round of test. It can be seen that the sample's resistance is stable at 100% RH, while the resistance at 0% RH increases after the first test and start

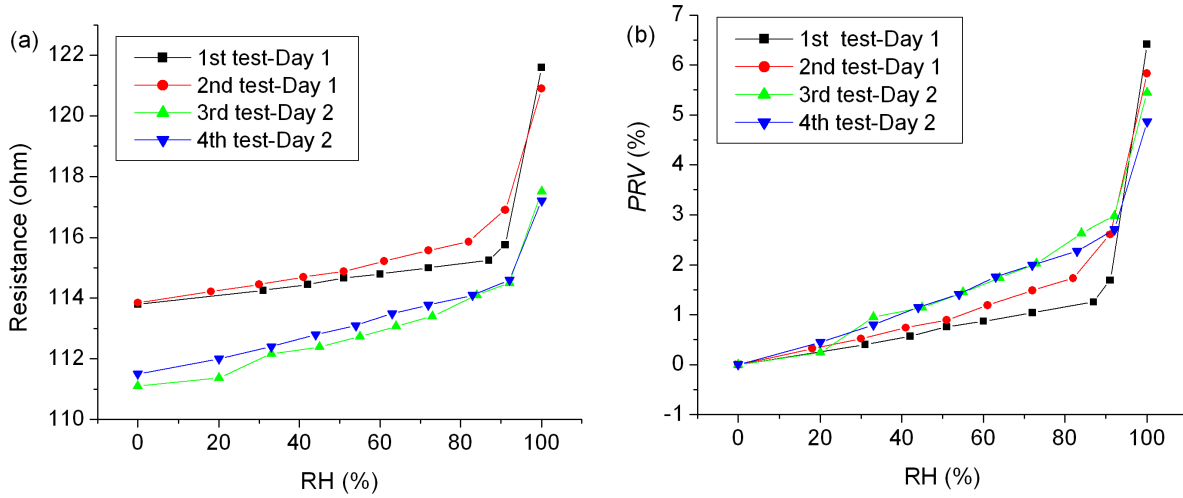


Figure 5.6: (a) the Resistance-RH curve of sample 1 for several rounds of test, (b) the corresponding PRV -RH curve.

to approach a steady state.

Figure 5.6 (a) shows the Resistance-RH curve for sample 1 in two different days after the first test. It is observed that the baseline resistance reading (R_0) of the sample changes slightly from day to day. However, for the same day, during a different round of test, the baseline resistance reading is relatively stable. The sensor shows steady resistance change over a wide range of relative humidity (from 0% to 100%). The sensing curve can be divided into two regions: Region I, 0% RH- 90% RH and Region II, 90% RH - 100% RH. For both regions, the sensor shows a very linear R-RH relationship. Although the resistance here increases compared to the the decrease in the metal oxide thin film coated macroporous samples we dicussed before, their response patterns are very similar. Both of them show a sudden increase in sensitivity at a certain high RH level. Samples with ZnO and HfO₂ surface show the sudden change at 90%-95% RH level, while Ta₂O₅ coated samples show the change around 70% RH level. This can be explained by the lower contact angle of Ta₂O₅ surface, where the chemisorbed layer forms more easily and allows the formation of

multi-layers by physisorption at a lower RH level.

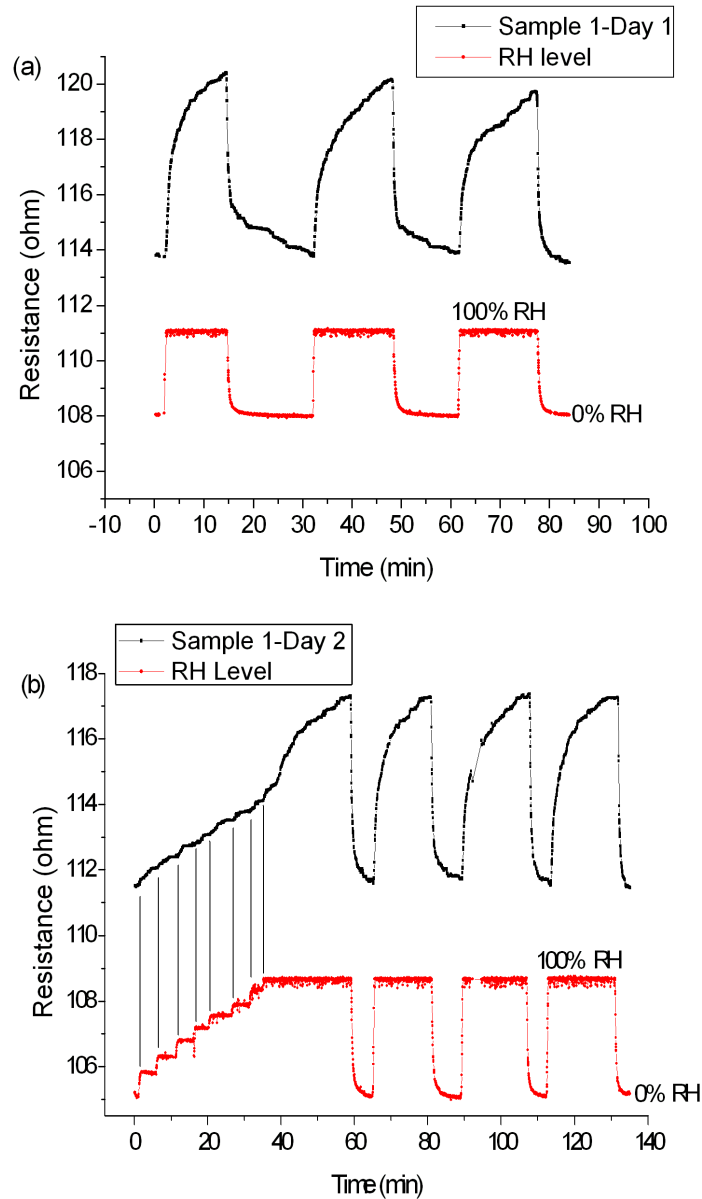


Figure 5.7: (Dynamic resistance response to change RH of sample 1's for test in different days, (a) day 1, (b) day 2.

Figure 5.6 (b) shows the corresponding *PRV*-RH curves of sample 1. Compared to the

original resistance variation at 100% RH for the first test (11.3%), the resistance variation at 100% RH slowly decreases from test to test. This slow change is probably caused by the incomplete oxidation of the nanorods surface. Although the sample has been post annealed, there are still unstable adsorption sites on the surface. After several rounds of test under high humidity level, these unstable sites are slowly oxidized and come to stable state. Therefore, the sensor's response to RH slowly becomes less sensitive but more stable. This also explains the better repeatability of the sensor's dynamic response on day 2 of the tests.

Figure 5.7 shows the dynamic resistance response of sample 1 to the changing RH in different days. Comparing these two curves, it can be seen that the dynamic response of the sensor is much more stable on the day 2. After several rounds of tests, the sensor reaches the steady state and shows very good repeatability with a fast response. Figure 5.7 (b) also shows the dynamic resistance response to step change of RH. In Region I (0% RH-90% RH), the sensor's response time (defined as the time to reach 90% of the total change) is 2 to 3 minutes. In Region II (90% RH to 100% RH) the response time is about 20 min, and when RH changes from 0% to 100%, the sensor's response time is 7 min with increasing RH. However, the sensor shows very fast response on the recover cycle with a 2 min response time.

Compared to sample 1, the unannealed nanorods (sample 6) show very high resistance variation at the first test. However, due to the high density of incomplete oxidation and crystallization sites, the sample shows very fast degradation over time. Three units (#1, #2 and #3) are made under the same condition as sample 6 and are tested for the degradation effect. Figure 5.8 shows the resistance variation change over time of these three units. #1 and #2 are tested as fresh samples. In the first test, both of them show 25-26% resistance

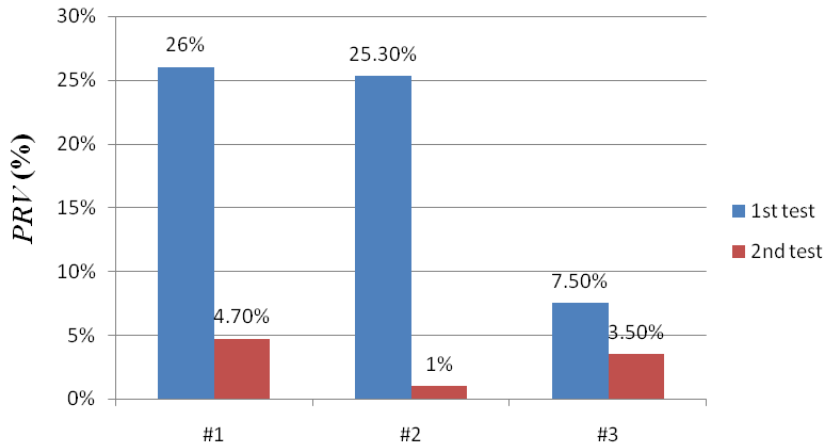


Figure 5.8: The percentage resistance variation degradation over time of three units from sample 6

variation at 100% RH. After 10 days, the resistance variation at 100% RH of #1 decreases dramatically to 4.7%. After 20 days from the first test, the resistance variation at 100% RH of #2 decreases to 1%. #3 is tested three months after the first test of #1 and #2. Due to the slow oxidation in air, the resistance variation of #3 is much lower than #1 and #2. The change of resistance variation at 100% RH between the first and second test is small. The sample's unstable response can also be observed from their dynamic response to changing RH, as shown in Figure 5.9. The resistance baseline (at 0%) is not as constant as sample 1 from cycle to cycle. However, the resistance at 100% RH is relatively stable. After a long time of testing, the response slowly becomes more stable (as shown in the last four cycles in Figure 5.9). Although sample 6 shows fast degradation over time and unstable responses to RH change, it shows much faster response time compared with sample 1. As seen in Figure 5.10, the response time for increasing RH from 0% to 100% is 140 seconds and 60 seconds for the recovery cycle.

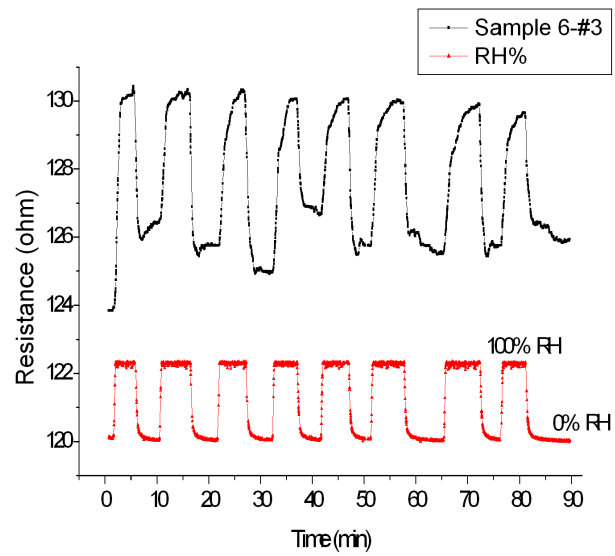


Figure 5.9: Dynamic response of Sample 6 (#3) to RH change cycles between 0% and 100%

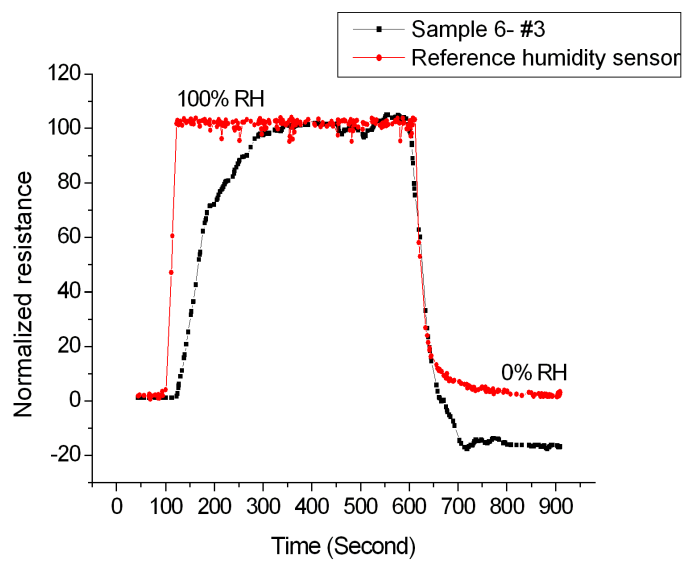


Figure 5.10: Comparison of the response time of sample 6 - #3 with the reference humidity sensor

5.5 Conclusions

In this chapter, we present the synthesis of vertically aligned ZnO nanorods with different conditions and their effect on the nanorods humidity sensing characteristics. Six different kinds of samples are prepared with different growing parameters, including the zinc source, growing time, with or without PEI and post annealing. It is demonstrated that ZnO nanorods grown from $\text{Zn}(\text{Ac})_2$ with shorter growing time and post annealing shows the best overall sensing characteristics. The sensor shows stable and linear resistance response to RH and a high sensitivity under high humidity level, which is very important for the application in fuel cells. Post annealing of the ZnO nanorods shows significant effects on the sensing properties in both positive and negative ways. Compared to nanorods with post annealing, the unannealed nanorods shows both much higher sensitivity and faster response. However, it also shows very fast degradation and unstable response to RH changes.

Chapter 6

Laterally Aligned ZnO Nanowires for Humidity Sensing

In the previous chapter, we reported the humidity sensing properties of vertically aligned ZnO nanorods. In this chapter, we explore the use of laterally aligned ZnO nanowires for humidity sensing. The detailed discussion of possible sensing mechanisms is also presented in this chapter.

6.1 Fabrication of the sensor

The ZnO nanowires were synthesized using the same method as the nanorods presented in the previous chapter. Here, we briefly state the process. ZnO nanowires are synthesized on indium tin oxide (ITO) substrate. To enhance the wetting of the seed layer on ITO substrates, the substrates were irradiated by UV lamp. The formation of the seed layer on ITO substrate was conducted using precipitation deposition in ZnO colloid solution. After

ZnO nanoparticles were precipitated on the ITO substrates, the substrates were annealed in air at 550 °C for 30 minutes in the furnace. Then ZnO nanowires were grown on the seed layer using hydrothermal method in 0.01 M aqueous solution of zinc acetate dehydrate ($\text{Zn}(\text{Ac})_2\cdot 2\text{H}_2\text{O}$, Showa, 99%) and hexamethyltetramine (HMTA, ACROS, 98.5%) at 95 °C for 3 hours. After growth, the substrate was removed from the solution, followed by rinsing with DI water, and then dried in air. To fabricate ZnO nanowires humidity sensors, the as-grown products were withdrawn by ultrasonication and suspended in a mixture solution of ethanol and DI-water with a ratio of 1:1. After the ZnO nanowires were suspended in ethanol aqueous solution, we can assemble ZnO nanowires on substrate with interdigital electrodes (IDEs) via dielectrophoretic (DEP) force. The Au IDEs were fabricated by lift-off process on SiO_2 substrate. The width of the electrodes is 5 μm and the gap between is 3 μm . For DEP assembling, the power supply is a function generator with a maximum frequency $f=10$ MHz. After switching on the frequency generator to the setting value of electrical field and frequency, a drop of ZnO nanowires suspension solution (~ 50 μL) is applied to the chip with a pipette. After a delay time, the drop is blown gently off the surface with air. Finally, the generator is turn off, and the sample is characterized by scanning electron microscopy (SEM). During the assembly of ZnO nanowires by DEP force, vaporization rate of the suspension solution, the applied electric field and frequencies will affect ZnO nanowires alignment situation and contact between ZnO nanowires and electrodes.

Morphologies of as-grown ZnO nanowires and the result of a simultaneous deposition of ZnO nanowires onto the IDEs pattern via DEP forces with various frequencies are shown in Figure 6.1(a)-(f). The diameter and length of ZnO nanowires used in this study are 150-200 nm and 15 μm . From X-ray diffraction analysis, the ZnO nanowires were grown

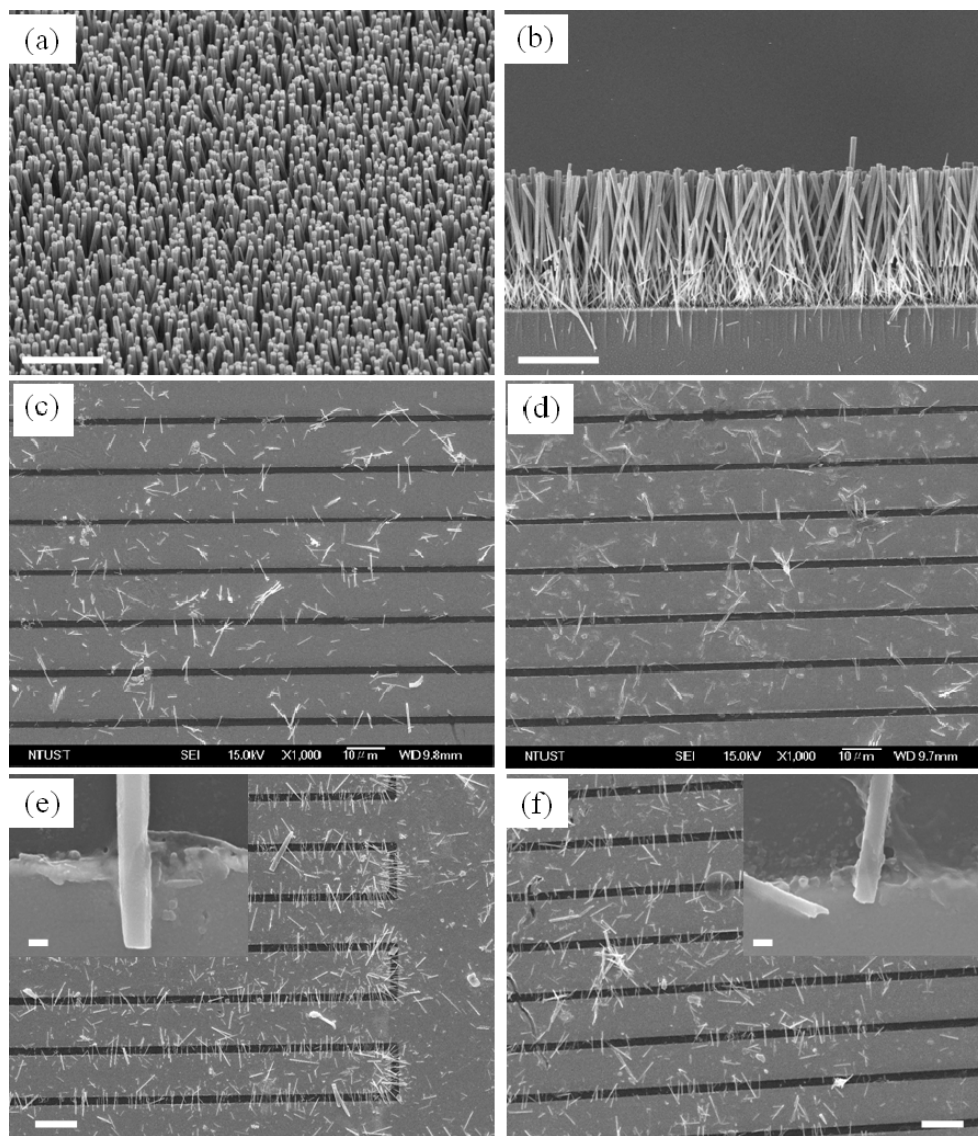


Figure 6.1: (a)-(b) tile-view and cross-sectional images of ZnO nanowires grown on ITO substrates with a seed layer; ZnO nanowires assembled via DEP force with (c) $f=100\text{kHz}$ and $V_{p-p} = 8\text{V}$, and (d) $f=1\text{ MHz}$ and $V_{p-p} = 8\text{V}$ in pure ethanol with 10 drops; (e) $f=100\text{kHz}$ and $V_{p-p} = 8\text{V}$, and (f) $f=1\text{ MHz}$ and $V_{p-p} = 8\text{V}$ in ethanol and water mixture with 50 drops. (Scale bars: (a)-(d), $10\ \mu\text{m}$; insets of (c)-(f), $200\ \text{nm}$).

along $[0001]$ direction. The geometry of ZnO nanowires can be controlled by reactant concentration and growth time. The ZnO nanowires assembly situation by DEP force

applies an electrical field of 8 V onto the IDE pattern and varied the drops and frequency to modulate the assembly. Figure 6.1(c) and (d) show the samples that are assembled in pure ethanol with 10 drops at 8 V and 100 kHz and 1 MHz respectively, while Figure 6.1(e) and (f) show the samples that are assembled in ethanol and water mixture with 50 drops. It can be seen that under the same condition, more drop times and the addition of water in the solution can significantly enhance the nanowires density and alignment. Comparing the Figure 6.1(e) and (f), the nanowires align better between the electrodes at middle range frequency (100 kHz). This is because the contact between ZnO nanowires and electrodes are destroyed when applying high frequencies, as shown in the insert of Figure 6.1(f).

6.2 Humidity sensing characterization

To test the sensor, the substrate is attached to a chip carrier and wire bonded to the electrodes. The sensor is 20 mm \times 10 mm and the chip is 33 mm \times 20 mm. Figure 6.2 shows a schematic and image of the sensor. The chip is then put into the testing chamber. The measurements is performed at room temperature.

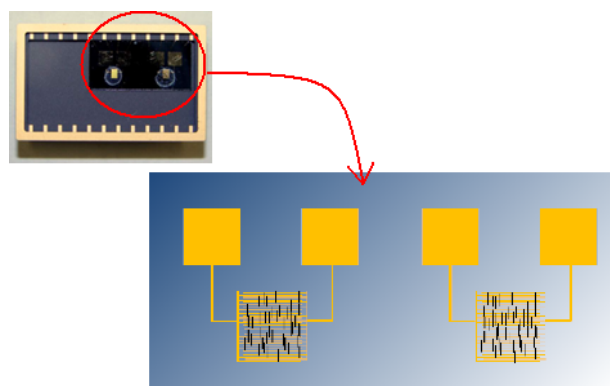


Figure 6.2: A picture of the as fabricated humidity sensor.

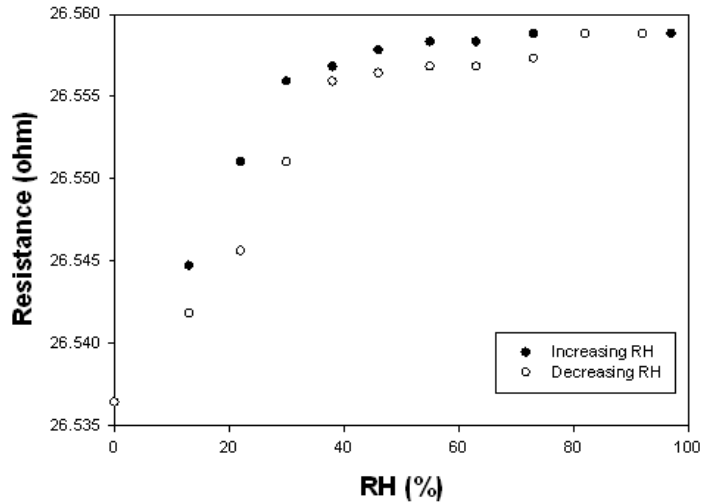


Figure 6.3: Resistance-RH curves with increasing and decreasing RH steps.

A resistance measurement was performed to evaluate the behavior of the sensor with humidity changes. The measurement voltage sets in 1V. The resistance of sensor is measured by changing RH from 0% to 100% in incremental steps. Each step is maintained at a constant value until the resistance reading reaches a steady state. Figure 6.3 shows the resistance response of the sensor to both increasing and decreasing RH steps. The resistance of sensor increases immediately when the RH level increases. Overall, the sensor showed very small capacitance variation. At low RH region, the variation is much larger than that of the high RH region. The change starts to slow down at 35% RH. We believe that this indicates the lack of the physisorbed multi-layers due to the single nanowire morphology. For most metal oxides sensors, the physisorption and high sensitivity at high RH level are usually caused by the nanoporous structure, which can significantly enhance the water adsorption and condensation. However, in this laterally aligned nanowire sensor, the single wires are far apart from each other - neither in a bundle nor interconnected. More over,

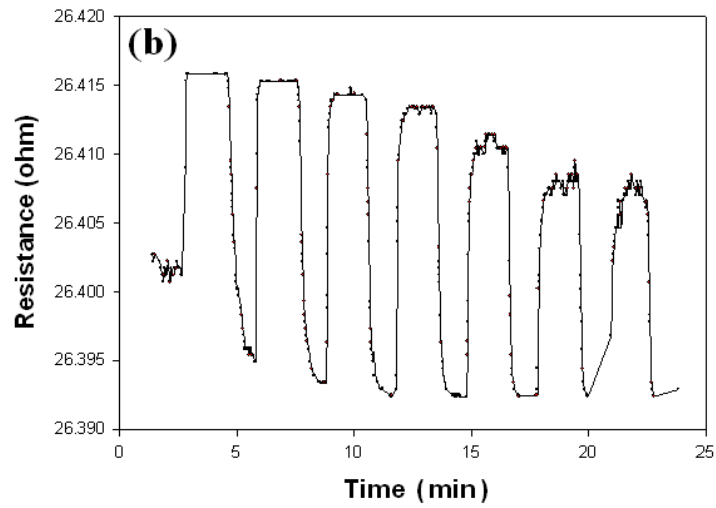
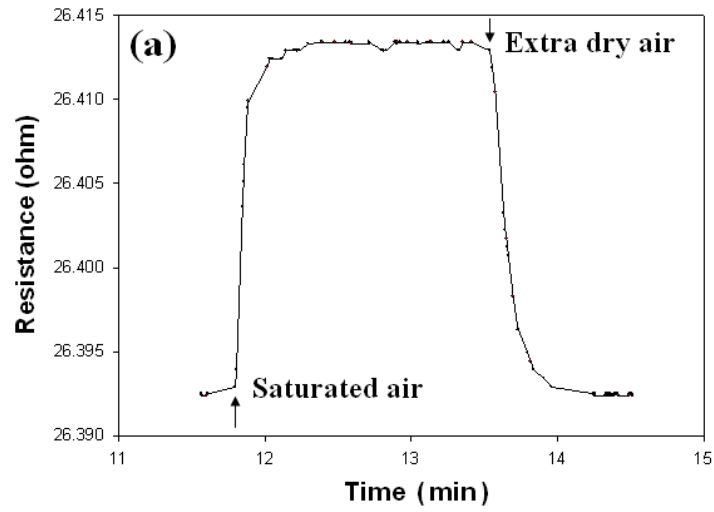


Figure 6.4: (a) Response time of the sensor at both increasing and decreasing RH ; (b) Dynamic response of the resistance of sensor to cycling changing RH between extra dry air and saturated air.

the convex shape of the nanowires surface may even prevent the complete formation of the first chemisorbed layer. This explains why a laterally aligned sample shows much smaller sensitivity than vertically aligned nanorods. When RH reaches 100% and the resistance reading reaches a steady state, we start to decrease the RH level in steps. The desorption curve follows the same path and show very small hysteresis.

Response and reproducibility are two important parameters to assess a humidity sensor as shown in Figure 6.4(a). The response time is 16 seconds when the RH increases from 0% to 100%, and recovery time is 25 seconds when the RH decreases from 100% to 0%. In Figure 6.4(b), we demonstrated the dynamic response of ZnO nanowires humidity sensor to cycle changes of RH between extra dry air and saturated air. The sensor shows slight degradation over time and gradually approach a steady state.

6.3 Discussions

In this section, we will discuss the possible mechanisms for the resistance increase with increasing humidity level observed in our experiment. As introduced earlier, most metal oxide semiconductor sensors show decrease in resistance (increasing conductivity) when exposed to water molecules. The most commonly used mechanism is the dissociation of the water molecule under electrical fields, causing surface conduction by proton hopping at low RH level and the Grotthuss chain reaction at higher RH level. Another mechanism that has been suggested is that the change in the conductance of the semiconductor itself is due to the surface fermi level shift in the presence of adsorbed water molecules [135, 136]. There is also the argument that it is the result of an indirect effect involving chemisorbed oxygen that has trapped electrons from the semiconductor. Adsorption of water molecules

replaces oxygen and leads to its desorption, causing the release of the electrons back to the material's conduction band [131, 137, 138]. However, in our experiment, the carrier gas is extra dry air, which means there is no change in the oxygen concentration. Sears [139] also demonstrate that this factor can be eliminated for their humidity sensor by a few measurement in oxygen-free nitrogen gas carrier. Therefore, this indirect mechanism does not seem to be a determining factor in our case.

In table 6.1, we summarize the conclusions from some references, including the sensing materials, their structure, operation temperature, baseline conductance, sensing response and proposed mechanisms. All of the these materials show decreasing resistance when exposed to moisture. Comparing these metal oxide nanostructures, the biggest difference in our sample is the very high conductivity with a resistance in the range of 20-150 ohm. This means that the nanorods/nanowires in this experiment have a high concentration of charge carriers in the conducting band at the original state. We believe this is due to high concentration of the anion vacancies in the nanorods/nanowires. As shown in Figure 6.5, to fulfill the electro neutrality, an oxygen vacancy must accompany the presence of two electrons. These types of metal oxides are usually denoted as MO_{1-x} , acting as n-type semiconductors. When there is external electrical field applied, the electrons can enter the conducting band and contribute to the electrical conductivity. When there are species that contain oxygen atoms in the environment, the oxygen atom first adsorbs on the surface adsorption sites (s). The site can be the metal anion or the oxygen vacancy. When it adsorbs onto the adsorption sites, the process is:



Table 6.1: Comparison Table

Sensing Material	Material Structure	Sensing T(°C)	Baseline Conductance (S)	Proposed Mechanism	Ref.
$\text{Bi}_3\text{FeO}_4(\text{MoO}_4)_2$	Sintered Powered	24 to 60	0.16×10^{-12} to 190×10^{-12}	Grotthuss Chain Reaction	[139]
ZnO	Nanopellet	RT	0.25×10^{-8} to 0.32×10^{-8}	Proton Hopping and GCR	[140]
ZnO	Nanowires	80	$< 0.17 \times 10^{-15}$	Reversibly Reaction with Lattice	[141]
ZnO – TiO ₂	Nano-composite	19 to 550	0.5×10^{-9} to 10×10^{-9}	GCR	[142]
Al-doped ZnO	Nano-crystalline Thin Film	330 to 350	1×10^{-10}	Proton Hopping	[143]
ZnCr ₂ O ₄ – ZnO	Sintered Disk	330 to 350	0.25×10^{-9} to 3.0×10^{-9}		[144]
MnO, ZnO, Fe ₂ O ₃	Composite	30 to 60	1.0×10^{-4}	Hopping and Capillary Condensation	[145]
ZnO – 5Al ₂ O ₃	Thick Film	RT		Electron Injection	[146]

Sensing Material	Material Structure	Sensing T(°C)	Baseline Conductance (S)	Proposed Mechanism	Ref.
ZnO	Nano-tetrapods	RT		Proton Hopping	[147]
ZnO	Nanorod and Nanobelt	RT	1.0×10^{-8} to 1.0×10^{-8}	Proton Hopping and Capillary Condensation	[148]
Al – doped ZnO with TiO ₂ thin film		RT	1.0×10^{-10} to 1.0×10^{-10}	Capillary Condensation	[149]
ZnO	Nanorod and Nanowire	RT	1.0×10^{-8}	Proton Hopping and Capillary Condensation	[150]
ZnO	Dense Pellets	RT		Variation of Barrier Height	[138]

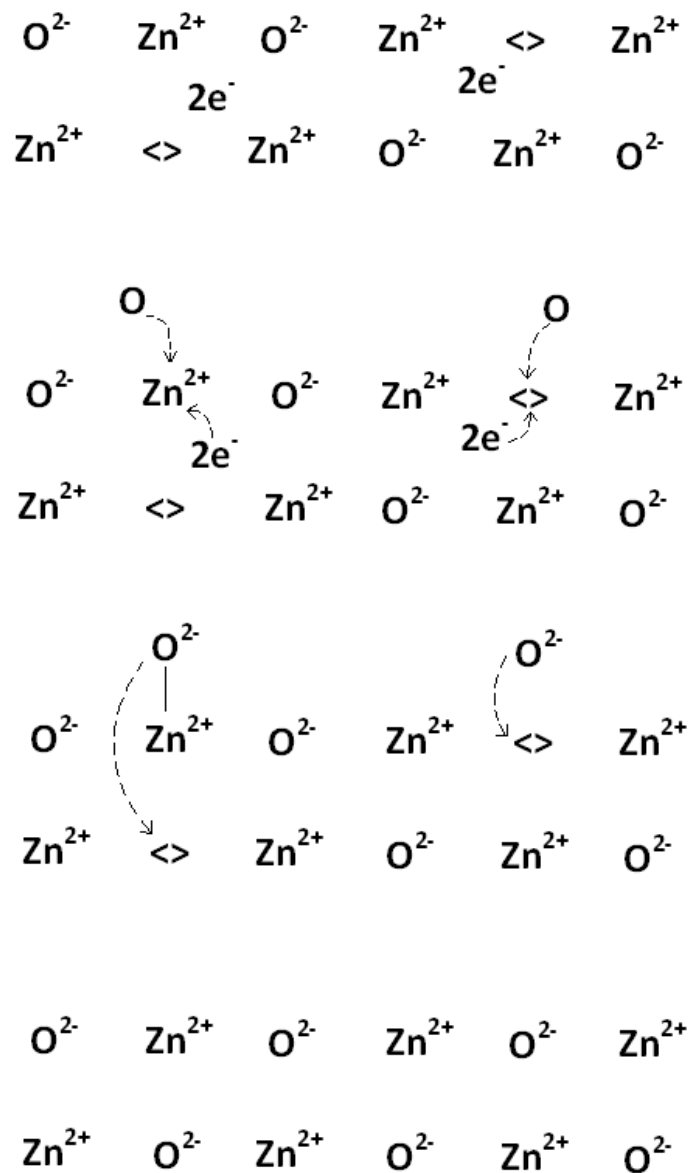


Figure 6.5: Insertion mechanism of oxygen atoms on the surface and inside the lattice of a MO_{1-x} type oxide

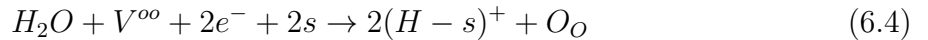
and:



The global process can be written as:



Where V^{oo} is the lattice cation vacancy. For these reactions to actually take place, either high temperature or ultra long term exposure is needed. If the sensor operates in room temperature, the processes above describe more of a trend, where oxygen molecules attract electrons to the surface area and creates a surface depletion layer. When the nanorods/nanowires are exposed to humid environment, we believe there are two mechanisms acting together to cause the decrease in conductivity. The first one is very similar to the situation in the adsorption of O_2 . The water molecules first adsorb onto the adsorption sites on the surface and then dissociated into protons and hydroxyl groups. The proton will adsorb onto surface oxygen atom, while the hydroxyl will adsorb onto either the surface anion site or the surface oxygen vacancy. The overall process can be written as:



The free electrons are trapped by the adsorbed water molecules. As a result, the sensor's conductance decreases with increasing RH. This explains the higher sensitivity of the unannealed nanorods than annealed ones, where there is much less oxygen vacancies due to the improvement of the lattice structure at high temperature. This also explains the

degradation in sensitivity of the nanorods in air. After long term exposure in dry or humid air, the oxygen vacancies in the lattice are permanently filled by adsorbed oxygen atoms, leading to the decrease of available oxygen vacancies and free electrons. For samples that have not been annealed in air at high temperature, the degradation is more obvious.

The second mechanism is due to the large dipole moment that water molecule possess. When there are layers of water molecules on the surface at electric field, the dipole will line up and capture the free electrons in the nanowires, creating a surface depletion layer. This mechanism is more dominant at high RH level and explains the sudden increase in sensitivity for the vertically aligned nanorods samples. Both of these two mechanisms will reduce the available charge carries and the width of the conducting band of the ZnO nanorods/nanowires, causing the increase in resistance. Figure 6.6 shows the influence of absorption water and oxygen molecules on the surface of ZnO nanowires.

We believe that the aligned 1D structure also affects the sensing properties. In table 6.1, all the materials have random structures. This morphology creates a large amount of interconnections and porous structures, which can significantly enhance the adsorption of water molecules and condensation. For most of the references that report very high sensitivity, capillary condensation is believed to be the main factor. However, for the vertically aligned nanorods in this experiment, there is very limited interconnection and capillary structures. This prevents the physisorption and condensation of the water molecules. This is even more obvious for the laterally aligned nanowires, where the nanowires are all separate from each other and form a single layer structure. This explains the near flat region at high RH level in the *PRC*-RH curve. More over, there are very small amounts of nanowires on the IDEs. Therefore, the sensor shows relative low overall sensitivity. For traditional sintered metal oxides, there are large amounts of grain boundaries, which are the main adsorption sites

for chemicals. However, the 1D nanorods/nanowires that are used here can be considered as a single crystal or a single grain. This also reduces the adsorption amount of water molecules and hence the sensitivity.

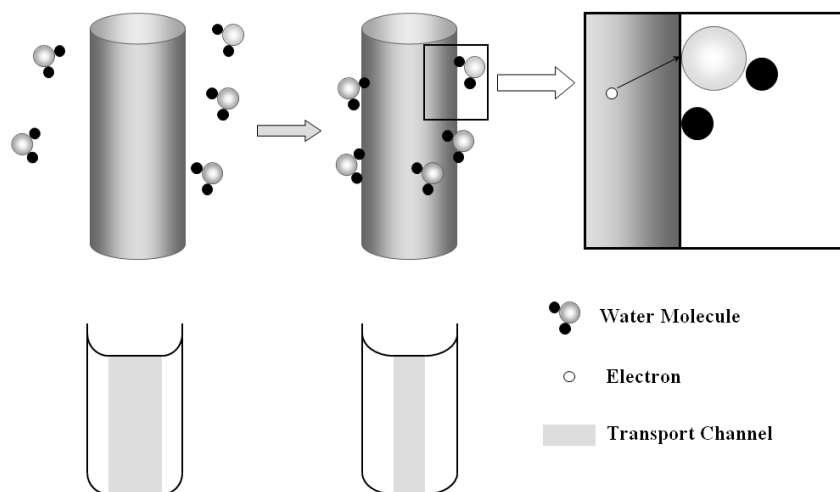


Figure 6.6: A simple picture showing the influence of absorption water and oxygen molecules on the surface of ZnO nanowires.

Another factor to be considered is the fabrication process of the sensor. The nanowires are aligned onto the IDEs in water and ethanol solutions and then air dried at room temperature. Therefore, there might have a certain amount of water and ethanol molecules residuals on the nanowires surface, which can reduce their humidity sensitivity. The weak contact between the nanowires and the electrodes needs to be improved as well for better sensitivity.

6.4 Conclusions

In the chapter, we synthesized vertically aligned ZnO nanowires on ITO substrate via hydrothermal method and assembled ZnO nanowires on IDEs via DEP force at low tempera-

ture. During the assembling, the suspension solution, electrical field and applied frequency all affect the alignment of ZnO nanowires and the electrode contact. Similar with the vertically aligned nanorods, the sensor shows increase resistance to increase RH level. The sensor has very small sensitivity, especially at high RH level. This is due to very small amount of nanowires on the device, the single layer and separated morphology. Possible mechanisms are proposed and discussed. To improve the sensor's sensing property, future works will be suggested in the next chapter.

Chapter 7

Contributions and Future work

7.1 Contributions

This work is motivated by the water management problem in PEMFCs and targeted to create a humidity sensor that can operate under high humidity level and high temperature. To achieve this, ordered micro-/nano-structured materials are chosen as the sensing layers for their unique advantages on property control and modification. The contributions of this work can be summarized as follow:

- Proposed and demonstrated the potential of ordered macroporous silicon humidity sensor for the first time. The main advantages of this material includes high resistance to high temperature and contamination, uniform pore size distribution, open ends with no interconnections, and possibility of surface modification. These factors match the requirement for operation in PEMFCs and allow better control of the sensing material.

- The resistance responses of the ordered macroporous silicon heterostructure and self-supporting membrane are tested. A 23-28% decrease in resistance is observed when RH changed from 0% to 100%. Good repeatability is obtained for both structures. The heterostructure showed similar sensing characteristics as the self-supporting membrane, suggesting that a simple fabrication of ordered macroporous silicon humidity sensor is possible.
- Heterostructure sensors with different thin film surface coatings including bare Si, thermally grown SiO₂, atom layer deposited ZnO, HfO₂, and Ta₂O₅ are characterized. The thin film coating of HfO₂, and Ta₂O₅ shows improvement to the sensor while the sensors with thermally grown SiO₂ and atom layer deposited ZnO show negligible response to RH changes. This is mainly caused by the differences in their surface contact angle.
- Ordered macroporous silicon sensors with HfO₂ thin film coating and different parameters are fabricated. Both of their resistance and capacitance responses are studied. The sensor showed a near-linear response compared to bare silicon samples. Although it takes a longer time to reach the total reading change, the HfO₂ modified sensor is able to sense the RH change within the testing chamber much faster than the commercial reference sensor.
- Post micro-fabrication is achieved on the cleaved pieces of ordered macroporous silicon. Proper PR and spin rate is characterized for a good pore coverage. The sensor can survive most of micro-fabrication processes, especially the commonly used chemicals (including water) without performance degradation.
- Ordered macroporous silicon sensors with Ta₂O₅ thin film coating and IDEs are thor-

oughly characterized at all aspects. The sensor shows high sensitivity, fast response time, very small hysteresis, extraordinary stability and repeatability, and ideal sensing properties at high temperatures and in condensing (even flooding) environment. It demonstrates great potential and advantages over existing commercial humidity sensors in the fuel cell application field.

- Sensing mechanisms of ordered macroporous silicon sensors are discussed. The phenomenon and mechanism for response time-frequency dependency is investigated in detail. It is believed that the external AC electric field has effects on the water molecule adsorption process. The existence of parasitic capacitance and resistance is proven and discussed.
- Both vertically and laterally aligned ZnO nanorods/nanowires are synthesized and their humidity sensing properties are characterized. To the best of our knowledge, this is the first attempt to use well aligned ZnO nanorods/nanowires for humidity sensing.
- Both of the vertically and laterally aligned ZnO 1D structures show decreasing conductivity with increasing humidity level. This is contrary to most of the other reported works. Possible sensing mechanisms and explanations are proposed and discussed. We believed that the sensing response is mainly due to the ultra high concentration of oxygen vacancies in the nanorods/nanowires.

7.2 Future work

7.2.1 Ordered macroporous silicon humidity sensor

We have proven the possibility and advantages of humidity monitoring of ordered macroporous silicon based sensors in fuel cell operation condition. To further develop this sensor for real world application, there are several directions that should be explored and improved. First, we will discuss it from the device level perspective.

- **Customization according to application:** The first question that needs to be addressed when integrating a humidity sensor into a fuel cell is where to put it. Ideally, there should be more than one sensor in the cell to monitor the humidity level in different areas. Figure 7.1 shows several locations that may be of interest. The sensors should be put as close as possible to the MEA area to monitor the RH level close to the PEM and gas diffusion layer. The RH level should be the highest at location A due to the production of water. The probability of flooding in this area is high. At location B, both drying and flooding is possible, depending on the operation condition. Drying is due to the consumption of moisture along the membrane, while flooding is the result of back diffusion from the cathode. Location C and D are to monitor the humidification level of the inlet gas. The sensors at these two locations are optional because the RH level can be measured outside the fuel cell as well. If more information about the RH level distribution is wanted, there can be more sensors between the inlets and outlets. The sensors can be fixed in the flow channels. To do this, either the channel or the sensor need to be customized for size matching and wire connections.

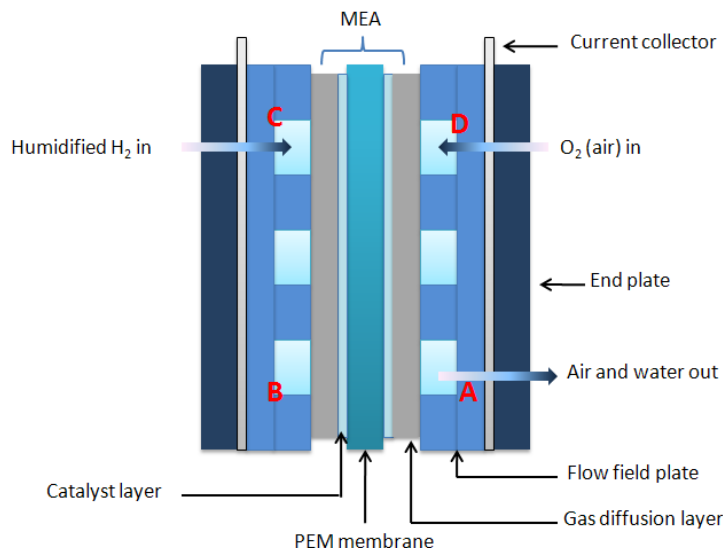


Figure 7.1: Preferable locations of humidity sensors in a single PEMFC.

- Sensor fabrication:** So far, all the sensors are fabricated in a standard etch cell, which can only handle small silicon pieces with size of 23mm * 23mm. When integrating into fuel cells, a new etch cell will be needed to match the size of the sensor's design requirement. Ideally, the etch cell's design should allow wafer level processing, which will allow more convenient and controllable fabrication for both pre- and post-processes. This will also allow a higher yield of the sensor fabrication.
- Humidity and temperature sensor:** Since we observed a very steady response of the sensor's capacitance/resistance response to temperature, it is possible to build a humidity sensor and temperature sensor from the same material on the same chip. The sensing layer and electrodes of these two sensors can be fabricated together by the same process. And then the temperature sensor can be covered by a additional layer while the humidity sensor is exposed to the environment during packaging.
- Wireless sensing:** Another interesting direction to go is a wireless humidity sensor.

There are several types of wireless sensors for humidity or chemical sensing, including surface acoustic wave (SAW), bulk acoustic wave (BAW), quartz crystal microbalance (QCM) and quartz tuning fork (QTF) [151, 152, 153, 154, 155, 156]. The mechanism of the wireless sensors is mainly the detection of the sensing materials mass change by oscillation. The advantage here is obvious. With the capability of wireless sensing, the integration of humidity sensor into fuel cell will be much easier.

- **Circuit integration:** One important advantage of using macroporous silicon as a sensing material is the possibility of circuit integration. Once the sensor is thoroughly characterized, a circuit could be built for power supply, data acquisition and calibration. It's been proven that, by data calibration, the reading drift and hysteresis can be eliminated, and the output data can be linearized. This circuit can be built into the same package of the sensor.

In addition of development on the device aspect, there are still several areas that can be future explored:

- **Ordered macroporous silicon with TiO_2 coatings:** TiO_2 is a very commonly used humidity sensing material. With ALD, it is possible to uniformly coat TiO_2 thin film on the ordered macroporous silicon. The same structure as the one used in this experiment can be used to characterize its humidity sensing properties.
- **Mechanism study on response time:** We have shown that the sensor's response time is dependent on the testing frequency. Although we gave some preliminary explanation, more investigation is needed. One way to determine whether the external electrical field will affect the water adsorption is to measure the dynamic mass change of the sample at different operation frequency.

- **Mechanism study on parasitic capacitance:** We have demonstrated that the difference in sensitivity at different operation frequencies is caused by the existence of parasitic capacitance. There are also equations showing the relationships among the measured capacitance, effective capacitance and parasitic capacitance. However, due to the limitation of the measuring instruments, the parasitic capacitance has not been separated. With LCR meters that can go to extremely low and high operation frequency and the provided equations, this may be achieved. The advantage of doing so is that the sensor can show higher sensitivity and the device can operate at any frequency without being re-calibrated.
- **Ordered macroporous silicon with nano-size pores:** With nanolithography, it is possible to pre-pattern nano-sized nucleation spots for the formation of ordered macroporous silicon with pore size in hundreds nanometers. This will significantly increase the porosity and surface area for higher sensitivity.

7.2.2 Aligned ZnO nanowires for humidity sensing

For the aligned ZnO nanorods/nanowires humidity sensor, the studies in near future should still focus on the mechanism and improvement aspect. It includes:

- **Sensing mechanisms** We have proposed that the increase in the material's resistance upon exposure to humidity is due to the existence of oxygen vacancies. To fully understand the mechanism and verify this assumption, more in depth study on the material is needed. So far, there are two analyses underway. One is Photoluminescence (PL) analysis, which can characterize the defect concentrations by visible

band intensity. The other is the carrier concentration analysis by impedance analysis. Combining these two techniques, we can prove the validity of the proposed mechanism.

- **Doping for sensing enhancement** One commonly used strategy to enhance metal oxides chemical sensitivity is doping. With another metal element in the structure, the energy band structure can be modified, which can lead to better sensitivity. Another approach is the dispersion of catalytic material among the nanorods/nanowires. Therefore, one of the future research topics will be the humidity sensing enhancement with different doping or catalytic material.
- **Sensor fabrication** There are still some parameters that can be adjusted for the sensor. For the laterally aligned sensor, the nanowires are dispersed in water and ethanol solution for DEP assembling. The water content in the solution might affect the sensor's behavior. Therefore, air drying at high temperatures may be preferred. As we discussed in the last chapter, low concentration of the nanowires on the sensor may be one of the factors for low sensitivity. So sensors with more solution drops can be fabricated in the future to maximize the nanowires concentration. Although DEP has been proven to be an effective method for nanowire alignment, the contact of the nanowires with the electrodes still needs to be improved.

Permissions

SPRINGER LICENSE TERMS AND CONDITIONS

Sep 29, 2010

This is a License Agreement between Yun Wang (You) and Springer (Springer) provided by Copyright Clearance Center (CCC). The license consists of your order details, the term and conditions provided by Springer, and the payment terms and conditions.

All payments must be made in full to CCC. For payment instructions, please see information listed at the bottom of this form. License Number: 2518260683275

License date: Sep 29, 2010

Licensed content publisher: Springer

Licensed content publication: Springer eBook

Licensed content title: Synthesis of Aligned ZnO Nanorods with Different Parameters and Their Effects on Humidity Sensing

Licensed content author: Yun Wang

Licensed content date: Jan 1, 2009

Type of Use: Thesis/Dissertation

Portion: Full text

Number of copies: 1

Author of this Springer article: Yes and you are the sole author of the new work

Order reference number:

Title of your thesis/dissertation: Ordered Micro-/Nanostructure Based Humidity Sensor for Fuel Cell Application

Expected completion date: Oct 2010

Estimated size(pages): 130

Total: 0.00 USD

Terms and Conditions

Introduction

The publisher for this copyrighted material is Springer Science + Business Media. By clicking accept in connection with completing this licensing transaction, you agree that the following terms and conditions apply to this transaction (along with the Billing and Payment terms and conditions established by Copyright Clearance Center, Inc. (CCC), at the time that you opened your Rightslink account and that are available at any time at <http://myaccount.copyright.com>).

Limited License

With reference to your request to reprint in your thesis material on which Springer Science and Business Media control the copyright, permission is granted, free of charge, for the use indicated in your enquiry. Licenses are for one-time use only with a maximum distribution equal to the number that you identified in the licensing process.

This License includes use in an electronic form, provided it is password protected or on the university's intranet, destined to microfilming by UMI and University repository. For any other electronic use, please contact Springer at (permissions.dordrecht@springer.com or permissions.heidelberg@springer.com)

The material can only be used for the purpose of defending your thesis, and with a maximum of 100 extra copies in paper.

Although Springer holds copyright to the material and is entitled to negotiate on rights, this license is only valid, provided permission is also obtained from the (co) author (address is given with the article/chapter) and provided it concerns original material which does not carry references to other sources (if material in question appears with credit to another source, authorization from that source is required as well). Permission free of charge on this occasion does not prejudice any rights we might have to charge for reproduction of our copyrighted material in the future.

Altering/Modifying Material: Not Permitted

However figures and illustrations may be altered minimally to serve your work. Any other abbreviations, additions, deletions and/or any other alterations shall be made only with prior written authorization of the author(s) and/or Springer Science + Business Media. (Please contact Springer at permissions.dordrecht@springer.com or permissions.heidelberg@springer.com)

Reservation of Rights

Springer Science + Business Media reserves all rights not specifically granted in the combination of (i) the license details provided by you and accepted in the course of this licensing transaction, (ii) these terms and conditions and (iii) CCC's Billing and Payment terms and conditions.

Copyright Notice:

Please include the following copyright citation referencing the publication in which the material was originally published. Where wording is within brackets, please include verbatim.

With kind permission from Springer Science+Business Media: book/journal title, chapter/article title, volume, year of publication, page, name(s) of author(s), figure number(s), and any original (first) copyright notice displayed with material. Warranties: Springer Science + Business Media makes no representations or warranties with respect to the licensed material.

Indemnity

You hereby indemnify and agree to hold harmless Springer Science + Business Media and CCC, and their respective officers, directors, employees and agents, from and against any and all claims arising out of your use of the licensed material other than as specifically authorized pursuant to this license.

No Transfer of License

This license is personal to you and may not be sublicensed, assigned, or transferred by you to any other person without Springer Science + Business Media's written permission.

No Amendment Except in Writing

This license may not be amended except in a writing signed by both parties (or, in the case of Springer Science + Business Media, by CCC on Springer Science + Business Media's behalf).

Objection to Contrary Terms

Springer Science + Business Media hereby objects to any terms contained in any purchase order, acknowledgment, check endorsement or other writing prepared by you, which terms are inconsistent with these terms and conditions or CCC's Billing and Payment terms and conditions. These terms and conditions, together with CCC's Billing and Payment terms and conditions (which are incorporated herein), comprise the entire agreement between you and Springer Science + Business Media (and CCC) concerning this licensing transaction. In the event of any conflict between your obligations established by these terms and conditions and those established by CCC's Billing and Payment terms and conditions, these terms and conditions shall control.

Jurisdiction

All disputes that may arise in connection with this present License, or the breach thereof, shall be settled exclusively by the country's law in which the work was originally published.

Other terms and conditions:

v1.2

Gratis licenses (referencing \$0 in the Total field) are free. Please retain this printable license for your reference. No payment is required.

If you would like to pay for this license now, please remit this license along with your payment made payable to "COPYRIGHT CLEARANCE CENTER" otherwise you will be invoiced within 48 hours of the license date. Payment should be in the form of a check or money order referencing your account number and this invoice number RLNK10857115.

Once you receive your invoice for this order, you may pay your invoice by credit card.

Please follow instructions provided at that time.

Make Payment To:

Copyright Clearance Center

Dept 001

P.O. Box 843006

Boston, MA 02284-3006

If you find copyrighted material related to this license will not be used and wish to cancel, please contact us referencing this license number 2518260683275 and noting the reason for cancellation.

Questions? customercare@copyright.com or +1-877-622-5543 (toll free in the US) or +1-978-646-2777.

**ELSEVIER LICENSE
TERMS AND CONDITIONS**

Sep 28, 2010

This is a License Agreement between Yun Wang (Yöu) and Elsevier (Eösevier) provided by Copyright Clearance Center (CöCC). The license consists of your order details, the terms and conditions provided by Elsevier, and the payment terms and conditions. All payments must be made in full to CCC. For payment instructions, please see information listed at the bottom of this form.

Supplier: Elsevier Limited

The Boulevard, Langford Lane

Kidlington, Oxford, OX5 1GB, UK

Registered Company Number: 1982084

Customer name: Yun Wang

License number: 2517710826263

License date: Sep 28, 2010

Licensed content publisher: Elsevier

Licensed content publication: Sensors and Actuators B: Chemical

Licensed content title: A capacitive humidity sensor based on ordered macroporous silicon with thin film surface coating

Licensed content author: Yun Wang, Seungwoo Park, John T.W. Yeow, Andreas Langner, Frank Mller

Licensed content date: 6 August 2010

Licensed content volume number: 149

Licensed content issue number: 1

Number of pages: 7

Type of Use: reuse in a thesis/dissertation

Portion: full article

Format: both print and electronic

Are you the author of this Elsevier article?: Yes

Will you be translating?: No

Order reference number

Title of your thesis/dissertation: Ordered Micro-/Nanostructure Based Humidity Sensor for Fuel Cell Application

Expected completion date: Oct 2010

Estimated size (number of pages): 130

Elsevier VAT number: GB 494 6272 12

Terms and Conditions

INTRODUCTION

1. The publisher for this copyrighted material is Elsevier. By clicking accept in connection with completing this licensing transaction, you agree that the following terms and conditions apply to this transaction (along with the Billing and Payment terms and conditions established by Copyright Clearance Center, Inc. (CCC), at the time that you opened your Rightslink account and that are available at any time at <http://myaccount.copyright.com>).

GENERAL TERMS

2. Elsevier hereby grants you permission to reproduce the aforementioned material subject to the terms and conditions indicated.

3. Acknowledgement: If any part of the material to be used (for example, figures) has appeared in our publication with credit or acknowledgement to another source, permission must also be sought from that source. If such permission is not obtained then that material may not be included in your publication/copies. Suitable acknowledgement to the source must be made, either as a footnote or in a reference list at the end of your publication, as follows:

Reprinted from Publication title, Vol /edition number, Author(s), Title of article / title of chapter, Pages No., Copyright (Year), with permission from Elsevier [OR APPLICABLE SOCIETY COPYRIGHT OWNER]. Also Lancet special credit - Reprinted from The Lancet, Vol. number, Author(s), Title of article, Pages No., Copyright (Year), with permission from Elsevier."

4. Reproduction of this material is confined to the purpose and/or media for which permission is hereby given.

5. Altering/Modifying Material: Not Permitted. However figures and illustrations may be altered/adapted minimally to serve your work. Any other abbreviations, additions, deletions and/or any other alterations shall be made only with prior written authorization of Elsevier Ltd. (Please contact Elsevier at permissions@elsevier.com)

6. If the permission fee for the requested use of our material is waived in this instance, please be advised that your future requests for Elsevier materials may attract a fee.

7. Reservation of Rights: Publisher reserves all rights not specifically granted in the combination of (i) the license details provided by you and accepted in the course of this licensing transaction, (ii) these terms and conditions and (iii) CCC's Billing and Payment terms and conditions.

8. License Contingent Upon Payment: While you may exercise the rights licensed immediately upon issuance of the license at the end of the licensing process for the transaction, provided that you have disclosed complete and accurate details of your proposed use, no license is finally effective unless and until full payment is received from you (either by

publisher or by CCC) as provided in CCC's Billing and Payment terms and conditions. If full payment is not received on a timely basis, then any license preliminarily granted shall be deemed automatically revoked and shall be void as if never granted. Further, in the event that you breach any of these terms and conditions or any of CCC's Billing and Payment terms and conditions, the license is automatically revoked and shall be void as if never granted. Use of materials as described in a revoked license, as well as any use of the materials beyond the scope of an unrevoked license, may constitute copyright infringement and publisher reserves the right to take any and all action to protect its copyright in the materials.

9. Warranties: Publisher makes no representations or warranties with respect to the licensed material.

10. Indemnity: You hereby indemnify and agree to hold harmless publisher and CCC, and their respective officers, directors, employees and agents, from and against any and all claims arising out of your use of the licensed material other than as specifically authorized pursuant to this license.

11. No Transfer of License: This license is personal to you and may not be sublicensed, assigned, or transferred by you to any other person without publisher's written permission.

12. No Amendment Except in Writing: This license may not be amended except in a writing signed by both parties (or, in the case of publisher, by CCC on publisher's behalf). 13. Objection to Contrary Terms: Publisher hereby objects to any terms contained in any purchase order, acknowledgment, check endorsement or other writing prepared by you, which terms are inconsistent with these terms and conditions or CCC's Billing and Payment terms and conditions. These terms and conditions, together with CCC's Billing and Payment terms and conditions (which are incorporated herein), comprise the entire agreement between you and publisher (and CCC) concerning this licensing transaction. In the event of any conflict between your obligations established by these terms and conditions and those established by CCC's Billing and Payment terms and conditions, these terms and conditions shall control.

14. Revocation: Elsevier or Copyright Clearance Center may deny the permissions described in this License at their sole discretion, for any reason or no reason, with a full refund payable to you. Notice of such denial will be made using the contact information provided by you. Failure to receive such notice will not alter or invalidate the denial. In no event will Elsevier or Copyright Clearance Center be responsible or liable for any costs, expenses or damage incurred by you as a result of a denial of your permission request, other than a refund of the amount(s) paid by you to Elsevier and/or Copyright Clearance Center for denied permissions.

LIMITED LICENSE

The following terms and conditions apply only to specific license types:

15. Translation: This permission is granted for non-exclusive world English rights only

unless your license was granted for translation rights. If you licensed translation rights you may only translate this content into the languages you requested. A professional translator must perform all translations and reproduce the content word for word preserving the integrity of the article. If this license is to re-use 1 or 2 figures then permission is granted for non-exclusive world rights in all languages.

16. Website: The following terms and conditions apply to electronic reserve and author websites:

Electronic reserve: If licensed material is to be posted to website, the web site is to be password-protected and made available only to bona fide students registered on a relevant course if:

This license was made in connection with a course,

This permission is granted for 1 year only. You may obtain a license for future website posting,

All content posted to the web site must maintain the copyright information line on the bottom of each image,

A hyper-text must be included to the Homepage of the journal from which you are licensing at <http://www.sciencedirect.com/science/journal/xxxxx> or the Elsevier homepage for books at <http://www.elsevier.com> , and

Central Storage: This license does not include permission for a scanned version of the material to be stored in a central repository such as that provided by Heron/XanEdu.

17. Author website for journals with the following additional clauses:

All content posted to the web site must maintain the copyright information line on the bottom of each image, and the permission granted is limited to the personal version of your paper. You are not allowed to download and post the published electronic version of your article (whether PDF or HTML, proof or final version), nor may you scan the printed edition to create an electronic version,

A hyper-text must be included to the Homepage of the journal from which you are licensing at <http://www.sciencedirect.com/science/journal/xxxxx> , As part of our normal production process, you will receive an e-mail notice when your article appears on Elsevier's online service ScienceDirect (www.sciencedirect.com). That e-mail will include the article's Digital Object Identifier (DOI). This number provides the electronic link to the published article and should be included in the posting of your personal version. We ask that you wait until you receive this e-mail and have the DOI to do any posting.

Central Storage: This license does not include permission for a scanned version of the material to be stored in a central repository such as that provided by Heron/XanEdu.

18. Author website for books with the following additional clauses:

Authors are permitted to place a brief summary of their work online only. A hyper-text must be included to the Elsevier homepage at <http://www.elsevier.com> All content posted to the web site must maintain the copyright information line on the bottom of each image. You are not allowed to download and post the published electronic version of your chapter,

nor may you scan the printed edition to create an electronic version.

Central Storage: This license does not include permission for a scanned version of the material to be stored in a central repository such as that provided by Heron/XanEdu.

19. Website (regular and for author): A hyper-text must be included to the Homepage of the journal from which you are licensing at <http://www.sciencedirect.com/science/journal/xxxxx>. or for books to the Elsevier homepage at <http://www.elsevier.com>

20. Thesis/Dissertation: If your license is for use in a thesis/dissertation your thesis may be submitted to your institution in either print or electronic form. Should your thesis be published commercially, please reapply for permission. These requirements include permission for the Library and Archives of Canada to supply single copies, on demand, of the complete thesis and include permission for UMI to supply single copies, on demand, of the complete thesis. Should your thesis be published commercially, please reapply for permission.

21. Other Conditions:

v1.6

Gratis licenses (referencing \$0 in the Total field) are free. Please retain this printable license for your reference. No payment is required.

If you would like to pay for this license now, please remit this license along with your payment made payable to COPYRIGHT CLEARANCE CENTER otherwise you will be invoiced within 48 hours of the license date. Payment should be in the form of a check or money order referencing your account number and this invoice number RLNK10856531.

Once you receive your invoice for this order, you may pay your invoice by credit card. Please follow instructions provided at that time.

**Make Payment To:
Copyright Clearance Center
Dept 001
P.O. Box 843006
Boston, MA 02284-3006**

If you find copyrighted material related to this license will not be used and wish to cancel, please contact us referencing this license number 2517710826263 and noting the reason for cancellation.

Questions? customercare@copyright.com or +1-877-622-5543 (toll free in the US) or +1-978-646-2777.

Bibliography

- [1] Brian Cook. Introduction to fuel cells and hydrogen technology. *Engineering science and education journal*, 11:205–216, 2002. 1
- [2] J. J. Baschuk and X.Li. Modeling of polymer electrolyte membrane fuel cells with variable degrees of water flooding. *Journal of Power Sources*, 86:181–196, 2000. 2
- [3] Denise Mckay and Anna Stefanopoulou. Parameterization and validation of a lumped parameter diffusion model for fuel cell stack membrane humidity estimation. *Proceeding of the 2004 American Control Conference*, pages 816–821, 2004. 2
- [4] Dongmei Chen and Hueipei. Modeling and simulation of a pem fuel cell humidification system. *Proceeding of the 2004 American Control Conference*, pages 822–827, 2004. 2
- [5] Z.M. Rittersma. Recent achievements in miniaturised humidity sensors—a review of transduction techniques. *Sensors and Actuators A*, 96:196–210, 2002. 2, 16
- [6] Ralph Fenner and Edward Zdankiewicz. Micromachined water vapor sensors: a review of sensing technologies. *IEEE Sensors Journal*, 1:390–316, 2001. 3
- [7] A. Boudghene Stambouli and E. Traversa. Fuel cells, an alternative sources of energy. *Renewable and sustainable energy reviews*, 6:297–306, 2002. 5
- [8] Ali T-Raissi, Arundhati Banerjee, and Kenneth G. Sheinkopf. Current technology of fuel cell systems. *Energy Conversion Engineering Conference, Proceedings of the 32nd Intersociety*, 3:1953–1957, 1997. 7
- [9] Yong-Song Chen. *A segmented model for studying water transport in a PEM fuel cell*. PhD thesis, University of Michigan, 2009. 7
- [10] Mengbo Ji and Zidong Wei. A review of water management in polymer electrolyte membrane fuel cells. *Energies*, 2:1057–1106, 2009. 7
- [11] Xianguo Li. *Principles of fuel cells*. Taylor & Francis Group, New York, 2006. 7

- [12] A. Eisenberg and H.L. Yeager. *Perfluorinated Ionomer Membranes*. American Chemical Society, Washington DC, 1982. 7
- [13] S. Vergatesan, H.J. Kima, E.A. Cho, and et al. Operation of a proton-exchange membrane fuel cell under non-humidified conditions using thin cast nafion membranes with different gas-diffusion media. *Journal of Power Sources*, 156:294–299, 2006. 8
- [14] G. A. Somorjai. *Principles of surface chemistry*. Prentice-Hall, Inc., Englewood Cliffs, New Jersey, 1972. 9
- [15] René Lalauze. *Physical chemistry of solid-gas interfaces*. John Wiley & Sons, Inc., Hoboken, NJ, 2008. 11
- [16] L.D. Gelb, K.E. Gubbins, R. Radhakrishnan, and M. Sliwinska-Bartkowiak. Phase separation in confined systems. *Rep. Prog. Phys.*, 62:1573–1659, 1999. 11
- [17] C. Loughlin. Tutorial: Moisture content and humidity. *Sensor Review*, pages 137–140, 1990. 11
- [18] H. P. Penman. *Humidity*. Chapman and Hall, London, 1955. 12
- [19] Larry R. Genskow, Wayne E. Beimesch, John P. Hecht, and et.al. *Psychrometry, Evaporative Cooling, and Solids Drying*. McGraw-Hill, 2008. 12, 35, 37
- [20] Y. Sakai, Y. Sadaoka, and M. Matsuguchi. Humidity sensors based on polymer thin films. *Sensors and Actuators B*, 35–36:85–90, 1996. 13
- [21] P. Schubert and J. Nevin. A polymer-based capacitive humidity sensor. *IEEE TRans. Electron Devices*, 32:1220–1223, 1985. 13
- [22] Michael J. Haji-Sheikh, Joe Ervin, and Michael Andersen. Anodic nano-porous humidity sensing thin films for the commercial and industrial applications. *IEEE IAS*, pages 1207–1210, 2004. 14
- [23] Enrico Traversa. Ceramic sensors for humidity detection: the state-of-the-art and future developments. *Sensors and Actuators B*, 23:135–156, 1995. 14
- [24] Tsuneharu Nitta, Jiro Terada, and Fumio Fukushima. Multifunctional ceramic sensors: humidity gas sensor and temperature-humidity sensor. *IEEE Trans. Electron Devices*, 29:95–101, 1982. 14
- [25] Y. Yokomizo, M. Harata S. Uno, H. Hiraki, and K. Yuki. Microstructure and humidity-sensitive properties of $zncr_2o_4 - liznvo_4$ ceramic sensors. *Sensors and Actuators*, 4:599–606, 1983. 14

- [26] P. Kuban, J.M. Berg, P. K Dasgupta, and T. Dallas. Highly durable microfabricated sensors for humidity monitoring. *Analytical Chemistry*, 76:2561–2567, 2004. 16
- [27] Jesus M. Corres, Ignacio R. Matias, Miguel Hernaez, and et al. Optical fiber humidity sensors using nanostructured coatings of sio2 nanoparticles. *IEEE Sensors*, 8:281–285, 2008. 18
- [28] Ignacio R. Matias, Francisco J. Arregui, Jesus M. Corres, and Javier Bravo. Evanescent field fiber-optic sensors for humidity monitoring based on nanocoatings. *IEEE Sensors*, 7:89–95, 2007. 18
- [29] Alain Walcarius and Alexander Kuhn. Ordered porous thin films in electrochemical analysis. *Trends in Analytical Chemistry*, 27:593–603, 2008. 18
- [30] V.V. Guliants, M.A. Carreon, and Y.S. Lin. Ordered mesoporous and macroporous inorganic films and membranes. *Journal of Membrane Science*, 235:53–72, 2004. 18
- [31] Qi Qi, Tong Zhanga, and Xuejun Zheng. Preparation and humidity sensing properties of fe-doped mesoporous silica sba-15. *Sensors and Actuators B*, 135:255–261, 2008. 18
- [32] T. Wagner, T. Sauerwald, and C.-D. Kohl. Gas sensor based on ordered mesoporous In_2O_3 . *Thin Solid Films*, 517:6170–6175, 2009. 18
- [33] Liang Cui, Juan Peng, and Yan Ding. Ordered porous polymer films via phase separation in humidity environment. *Polymer*, 46:5334–5340, 2005. 18
- [34] Wangchang Geng, Rui Wang, and Xiaotian Li. Humidity sensitive property of li-doped mesoporous silica sba-15. *Sensors and Actuators B*, 127:323–329, 2007. 18
- [35] Jinchun Tu, Rui Wang, and Wangchang Geng. Humidity sensitive property of li-doped 3d periodic mesoporous silica sba-16. *Sensors and Actuators B*, 136:392–398, 2009. 19, 20
- [36] Lijie Wang, Di Li, and Rui Wang. Study on humidity sensing property based on li-doped mesoporous silica mcm-41. *Sensors and Actuators B*, 133:622–627, 2008. 19, 20
- [37] Richard A. Farrell, Nikolay Petkov, and Michael A. Morris. Self-assembled templates for the generation of arrays of 1-dimensional nanostructures: From molecules to devices. *Journal of Colloid and Interface Science*, in print, 2010. 19
- [38] Youngdeuk Kim, Bongbu Jung, and Hunkee Leea. Capacitive humidity sensor design based on anodic aluminum oxide. *Sensors and Actuators B*, 141:441–446, 2009. 19, 20

- [39] Fengjuan Miao, Bairui Tao, and Li Sun. Capacitive humidity sensing behavior of ordered ni/si microchannel plate nanocomposites. *Sensors and Actuators A*, 160:48–53, 2010. 19
- [40] Volker Lehmann. *Electrochemistry of silicon*. Wiley-VCH, Weinheim, Germany, 2002. 22
- [41] Nobuyoshi Koshida and Hideki Koyama. Photoluminescent and electroluminescent properties of porous silicon. *Nanotechnology 3*, pages 192–195, 1992. 23
- [42] Walter Jaimes Salcedo, Francisco Javier, Ramirez Fernandez, and Joel C. Rubim. Photoluminescence quenching effect on porous silicon films for gas sensors application. *Spectrochimica Acta Part A*, 60:1065–1070, 2002. 23
- [43] Jirí J. Mareš, Jozef Krištofik, and Eduard Hulicius. Influence of humidity on transport in porous silicon. *Thin Solid Films*, 255:272–275, 1995. 24, 39
- [44] Luca Boarino, C. Baratto, F. Geobaldo, and et al. NO₂ monitoring at room temperature by a porous silicon gas sensor. *Materials Science and Engineering*, B69-70:210–214, 2000. 24
- [45] G. Barillaro, A. Diligenti, A. Nannini, and L. M. Strambini. Gas sensors based on silicon devices with a porous layer. *Phys. Stat. Sol.*, c2, No. 9:3424–3428, 2005. 25
- [46] E. Galeazzo, H.E.M. Peres, G. Santos, N. Peixoto, and F. J. Ramirez-Fernandez. Gas sensitive porous silicon devices: responses to organic vapors. *Sensors and Actuators B*, 93:384–390, 2003. 25
- [47] G. Di Francia, A. Castaldo, E. Massera, I. Nasti, L. Quercia, and I. Rea. A very sensitive porous silicon based humidity sensor. *Sensors and Actuators B*, 111–112:135–139, 2005. 25
- [48] P. Frjes, A. Kovcs, Cs. Dcs, M. dm, B. Mller, and U. Mescheder. Porous silicon-based humidity sensor with interdigital electrodes and internal heaters. *Sensors and Actuators B*, 95:140–144, 2003. 25
- [49] D.G. Yarkin. Impedance of humidity sensitive metal/porous silicon/n-si structures. *Sensors and Actuators A*, 107:1–6, 2003. 25
- [50] R.C. Anderson, R.S. Muller, and C.W. Tobias. Investigations of porous silicon for vapor sensing. *Sensors and Actuators*, A21–A23:835–839, 1990. 25, 32
- [51] Mikko Bjrkqvist, Jaani Paski, Jarno Salonen, and Vesa-Pekka Lehto. Studies on hysteresis reduction in thermally carbonized porous silicon humidity sensor. *IEEE Sensors*, 6, No. 3:542–547, 2006. 25

- [52] M. Björkqvist, J. Paski, J. Salonen, and V.P. Lehto. Temperature dependence of thermally-carbonized porous silicon humidity sensor. *Phys. Stat. Sol.*, 202, No. 8:1653–1657, 2005. 25, 26
- [53] Jayoti Das, Sagnik Dey, Syed Minhaz Hossain, Z. M. Chris Rittersma, and Hiranmay Saha. A hygrometer comprising a porous silicon humidity sensor with phase-detection electronics. *IEEE Sensors*, 3, No. 4:414–420, 2003. 26, 27, 28
- [54] V. Lehmann and H. Fll. Formation mechanism and properties of electrochemically etched trenches in n-type silicon. *J. Electrochem. Soc.*, 137, No. 2:653–659, 1990. 27
- [55] Sven Matthias, Frank. Mller, Ccile Jamois, Ralf B. Wehrspohn, and Ulrich Gsele. Large-area three-dimensional structuring by electrochemical etching and lithography. *Adv. Mater.*, 16, No. 23–24:2166–2170, 2004. 27
- [56] Volker Lehmann. *Electrochemistry of silicon*. Wiley-VCH, Weinheim, Germany, 2002. 28
- [57] M. Archer, M. Christophersen, and P.M. Fauchet. Macroporous silicon electrical sensor for dna hybridization detection. *Biomedical Microdevices*, 6, No. 3:203–211, 2004. 28
- [58] Israel Schechter. Gas sensing properties of porous silicon. *Anal. Chem.*, 67:3727–3732, 1995. 32
- [59] Jeffrey M. Lauerhaas and Michael J. Sailor. Chemical modification of the photoluminescence quenching of porous silicon. *Science*, 261, No. 17:1567–1568, 1993. 32
- [60] Uk-Song Kang. *A high speed capacitive humidity sensor*. PhD thesis, University of Michigan, 1999. 35, 36
- [61] V. Lehmann, F. Hofmann, F. Mller, and U. Grning. Resistivity of porous silicon: a surface effect. *Thin Solid films*, 255:20–22, 1995. 39
- [62] Cherkaoui, A. Negara, S. McDonnell, G. Hughes, M. Modreanu, and P. K. Hurley. Electrical properties of hfo2 films formed by ion assisted deposition. *Proc. 25th Int. Conf. Microelectronics*, pages 14–17, 2006. 42
- [63] P.D. Kirsch, M.A. Quevedo, G. Pant, S. Krishnan, S.C. Song, and H.J. Li. Relationship of hfo2 material properties and transistor performance. *2006 Int. Sym. on VLSI Tech., Sys., and App.*, pages 1–4, 2006. 42
- [64] C. Moldovan, R. Iosub, M. Modreanu, D. Ulieru, B. Firtat, and M. Ion. Isfet micro-sensors hfo2 based for biomedical applications. *Int. Semiconductor Conf.*, 1:185–188, 2006. 42

- [65] Lai Chao-Sung, Yang Chia-Ming, and Lu Tseng-Fu. Thickness effects on ph response of hfo2 sensing dielectric improved by rapid thermal annealing. *Jpn J Appl Phys Part 1*, 45, No. 4B:3807–3810, 2006. 42
- [66] John J. Steele, Glen A. Fitzpatrick, and Michael J. Brett. Capacitive humidity sensors with high sensitivity and subsecond response times. *IEEE Sensor J.*, 6, No. 6:955–956, 2007. 42
- [67] J. Keller and R. Staudt. *Gas Adsorption Equilibria: Experimental methods and Adsorption Isotherms*. Springer, New York, 2005. 57
- [68] M. Björkqvist, J. Paski, J. Salonen, and et al. Temperature dependence of thermally-carbonized porous silicon humidity sensor. *Phys. Stat. sol. (a)*202, 8:1653–1657, 2005. 57
- [69] J. Keller and R. Staudt. *Gas Adsorption Equilibria: Experimental methods and Adsorption Isotherms*. Springer, New York, 2005. 57
- [70] A.B. Golovanchikov, M. Yu. Efremov, and E.V. Safonov. Gas adsorption in electric field. *Theoretical Foundations of Chemical Engineering*, 37, No.5:514–516, 2003. 57
- [71] Yoshiko Niki Kunishima, Masaru Miyayama, and Hiroaki Yanagida. Effects of the external electric field from a substrate on Cl₂ gas adsorption on SnO₂ thin films. *Appl. Phys. Lett.*, 69:632–634, 1996. 57
- [72] J. Das, S.M. Hossain, and S. Chahraborty. Role of parasitic in humidity sensing by porous silicon. *Sensors and Actuators A*, 94:44–52, 2001. 66, 69
- [73] Z.M. Rittersma and W. Benecke. A humidity sensor featuring a porous silicon capacitor with an integrated refresh resistor. *Sens. Mater.*, 12:35–55, 2000. 66
- [74] D.S. Mclachlan. The complex permittivity of emulsions: an effective media-percolation equation. *Solid State Commun.*, 72:831–834, 1989. 67
- [75] D.H. Kwon, B.W. Cho, C. S. Kim, and et al. Effects of heat treatment on Ta₂O₅ sensing membrane for low drift and high sensitivity ph-isfet. *Sensors and Actuators B*, 34:441–445, 1996. 67
- [76] Y. Wang and J.T.W. Yeow. Humidity sensing of ordered macroporous silicon with HfO₂ thin film surface coating. *IEEE Sens. J.*, 9:541–547, 2009. 67, 71
- [77] O.K. Varghese, P.D. Kichambre, D. Gong, K.G. Ong, E.C. Dickey, and C.A. Grimes. Gas sensing characteristics of multi-wall carbon nanotubes. *Sensors and Actuators B Chemical*, 81, No.1:32–41, 2001. 75

- [78] X. Huang, Y. Sun, L. Wang, F. Meng, and J. Liu. Carboxylation multi-walled carbon nanotubes modified with LiClO_4 for water vapour detection. *Nanotechnology*, 15, No.9:1284–1288, 2004. 75
- [79] J.T.W. Yeow and J.P.M. She. Carbon nanotube-enhanced capillary condensation for capacitive humidity sensor. *Nanotechnology*, 17:5441, 2006. 75
- [80] K.-S. Chou, T.-K. Lee, and F.-J. Liu. Sensing mechanism of a porous ceramic as humidity sensor. *Sensors and Actuators B Chemical*, 56, No.1:106–111, 1999. 75
- [81] S.P. Yawale, S.S. Yawale, and G.T. Lamdhade. Tin oxide and zinc oxide based doped humidity sensors. *Sensors and Actuators A Physical*, 135, No.2:388–393, 2007. 75
- [82] Q. Qi, T. Zhang, Q. Yu, R. Wang, Y. Zeng, L. Liu, and H. Yang. Properties of humidity sensing ZnO nanorods-base sensor fabricated by screen-printing. *Sensors and Actuators B Chemical*, 133, No.2:638–643, 2008. 75
- [83] B.C. Yadav, R. Srivastava, and C.D. Dwivedi. Synthesis and characterization of ZnO – TiO_2 nanocomposite and its application as a humidity sensor. *Philosophical Magazine*, 88, No.7:1113–1124, 2008. 75
- [84] B.C. Yadav, R. Srivastava, C.D. Dwivedi, and P.Pramanik. Moisture sensor based on ZnO nanomaterial synthesized through oxalate route. *Sensors and Actuators B Chemical*, 131, No.1:216–222, 2008. 75
- [85] N. Zhang, K. Yu, Z. Zhu, and D. Jiang. Synthesis and humidity sensing properties of feather-like ZnO nanostructures with macroscale in shape. *Sensors and Actuators A Physical*, 143, No.2:245–250, 2008. 75
- [86] F. Fang, J. Futter, A. Markwitz, and J. Kennedy. Uv and humidity sensing properties of ZnO nanorods prepared by the arc discharge method. *Nanotechnology*, 20, No.24:245502, 2009. 75
- [87] W. Wang, Z. Li, L. Liu, H. Zhang, W. Zheng, Y. Wang, H. Huang, Z. Wang, and C. Wang. Humidity sensor based on LiCl-doped ZnO electrospun nanofibers. *Sensors and Actuators B Chemical*, 141, No.2:404–409, 2009. 75
- [88] Q.H. Li, T. Gao, Y.G. Wang, and T.H. Wang. Adsorption and desorption of oxygen probed from ZnO nanowire films by photocurrent measurements. *Applied Physics Letters*, 86, No.12:123117, 2005. 75
- [89] G.Wang, Q. Wang, W. Lu, and J. Li. Photoelectrochemical study on charge transfer properties of TiO_2 nanowires with an application as humidity sensors. *Journal of Physical Chemistry B*, 110, No.43:22029–22034, 2006. 75

- [90] Q. Kuang, C. Lao, L.W. Zhong, Z. Xie, and L. Zheng. High-sensitivity humidity sensor based on a single SnO₂ nanowire. *Journal of American Chemical Society*, 129, No.19:6070–6071, 2007. 75
- [91] W. Yun, J.T.W. Yeow, and C. Liang-Yih. Synthesis of aligned zinc oxide nanorods for humidity sensing. *presented at the 3rd International Conference on Sensing Technology, ICST 2008*, 2:670–673, November 30, 2008. 75, 76
- [92] C.H. Kim, Y. Myung, Y.J. Cho, H.S. Kim, S.-H. Park, J. Park, J.-Y. Kim, and B. Kim. Electronic structure of vertically aligned Mn – dopedCoFe₂O₄ nanowires and their application as humidity sensors and photodetectors. *Journal of Physical Chemistry C*, 113, No.17:7085–7090, 2009. 75
- [93] E. Traversa. Cermaic sensors for humidity detection: the state-of-the-art and future developments. *Sensors and ACTuators B*, 23:135–156, 1995. 75
- [94] N. Barsan, D. Koziej, and U. Weimar. Metal oxide-based gas sensor research: How to? *Sensors and Actuators B*, 121:18–35, 2007. 75
- [95] Y. Zhang, K. Yu, D. Jiang, Z. Zhu, H. Geng, and L. Luo. Zinc oxide nanorod and nanowire for humidity sensor. *Applied Surface Science*, 242, No.1–2:212–217, 2005. 75, 76
- [96] L.Y. Chen, S.H. Wu, and Y.T. Ying. Catalyst-free growth of vertical alignment ZnO nanowire arrays by a two-stage process. *Journal of Physical Chemistry C*, 113, No.52:21572, 2009. 75
- [97] Y.D. Wang, J. Zhou, and J.H. Song. Piezoelectric field effect transistor and nanoforce sensor based on a single ZnO nanowire. *Nano Letters*, 6:2768–2772, 2006. 75
- [98] P.D. Yang, H.Q. Yan, and S. Mao. Controlled growth of ZnO nanowires and their optical properties. *Adv. Funct. Mater.*, 12:323–331, 2002. 75
- [99] M. Law, L.E. Greene, and J.C. Johnson. Nanowire dye-sensitized solar cells. *Nat. Mater.*, 4:445–459, 2005. 75
- [100] S.C. Navale, S.W. Gosavi, I.S. Mulla, and et al. Controlled synthesis of ZnO from nanospheres to micro-rods and its gas sensing studies. *Talanta*, 75:1315–1319, 2008. 75
- [101] D.C. Look. Recent advances in ZnO materials and devices. *Materials Science and Engineering B*, 80:383–387, 2001. 75

- [102] Ü. Özgür, Y.I. Alivov, C. Liu, and et al. A comprehensive review of ZnO materials and devices. *Applied Physics Reviews*, 98:041301, 2005. 75
- [103] Z.W. Pan, Z.R. Dai, and Z.L. Wang. Nanobelts of semiconducting oxides. *Science*, 291:1927–1949, 2001. 76
- [104] B. Liu and H.C. Zeng. Hydrothermal synthesis of ZnO nanorods in the diameter regime of 50 nm. *Journal of American chemical society*, 125:4430–4431, 2003. 76
- [105] Y.F. Qiu and S.H. Yang. ZnO nanotetrapods: Controlled vapor-phase synthesis and application for humidity sensing. *Adv. Funct. Mater.*, 17:1345–1352, 2007. 76
- [106] E. Traversa and A. Bearzotti. A novel humidity-detection mechanism for ZnO dense pellets. *Sensors and Actuators B*, 23:181–186, 1995. 76
- [107] Y.S. Zhang, K. Yu, D.S. Jiang, and et al. Zinc oxide nanorod and nanowire for humidity sensor. *Applied Surface Science*, 242:212–217, 2005. 76
- [108] X.F. Zhou, J. Zhang, T. Jiang, and et al. Humidity dection by nanostructured ZnO: A wireless quartz crystal microbalance investigation. *Sensors and Actuators A*, 137:209–214, 2007. 76
- [109] M.H. Huang, H.F.Y. Wu, N. Tran, E. Wever, and P. Yang. Catalytic growth of zinc oxide nanowires by vapor transport. *Adv. Mater*, 13:113, 2001. 76
- [110] X.Y. Kong and Z.L. Wang. Polar-surface dominated ZnO nanobelts and the electrostatic energy induced nanohelices, nanosprings, and nanospirals. *Applied Physics Letters*, 84:975, 2004. 76
- [111] P. Feng, Q. Wan, and T.H. Wang. Contact-controlled sensing properties of flowerlike ZnO nanostructures. *Applied Physics Letters*, 87:213111, 2005. 76
- [112] J. Zhang, S.R. Wang, Y. Wang, and et al. ZnO hollow spheres: Preparation, characterization and gas sensing properties. *Sensors and Actuators B Chemical*, 139, Issue 2:411–417, 2009. 76
- [113] C.S. Rout, A.R. Raju, A. Govindaraj, and et al. Hydrogen sensors based on ZnO nanoparticles. *Solid State Communications*, 138:136–138, 2006. 76
- [114] Y. Qui and S. Yang. ZnO nanotetrapods: Controlled vapor-phase synthesis and application for humidity sensing. *Advanced Functional Materials*, 17, No.8:1345–1352, 2007. 76

- [115] E. Comini, C. Baratto, G. Faglia, and et al. Quasi-one dimensional metal oxide semiconductors: Preparation, characterization and application as chemical sensors. *Progress in Materials Science*, 54:1–67, 2009. 76, 78
- [116] Jia Grace Lu, Paichun Chang, and Zhiyong Fan. Quasi-one-dimensional metal oxide materials—synthesis, properties and applications. *Materials Science and Engineering R*, 52:49–91, 2006. 76, 78
- [117] Y.W. Heoa, D.P. Nortona, L.C. Tien, and et al. Zno nanowire growth and devices. *Materials Science and Engineering R*, 47:1–47, 2004. 76
- [118] P.G. Li, X. Wang, and W.H. Tang. Facile synthesis of well-aligned zno nanowire arrays and their photoluminescence properties. *Journal of Alloys and Compounds*, 476:744–748, 2009. 77
- [119] Chih-Han Chen, Shoou-Jinn Chang, Sheng-Po Chang, and et al. Enhanced field emission of well-aligned zno nanowire arrays illuminated by uv. *Chemical Physics Letters*, 490:176–179, 2010. 77
- [120] Wenjie Mai, Puxian Gao, Changshi Lao, and et al. Vertically aligned zno nanowire arrays on gan and sic substrates. *Chemical Physics Letters*, 460:253–256, 2008. 77
- [121] Guomin Hua, Ye Zhang, Junxi Zhang, and et al. Fabrication of zno nanowire arrays by cycle growth in surfactantless aqueous solution and their applications on dye-sensitized solar cells. *Materials Letters*, 62:4109–4111, 2008. 77
- [122] S. Dalui, S.N. Das, R.K. Roy, and et al. Aligned zinc oxide nanorods by hybrid wet chemical route and their field emission properties. *Thin Solid Films*, 516:8219–8226, 2008. 77
- [123] O. Lupan, V.M. Guerina, I.M. Tiginyanub, and et al. Well-aligned arrays of vertically oriented zno nanowires electrodeposited on ito-coated glass and their integration in dye sensitized solar cells. *Journal of Photochemistry and Photobiology A: Chemistry*, 211:65–73, 2010. 77
- [124] G.Z. Wang, N.G. Ma, C.J. Deng, and et al. Large-scale synthesis of aligned hexagonal zno nanorods using chemical vapor deposition. *Materials Letters*, 58:2195–2198, 2004. 77
- [125] Gang Menga, Xiaodong Fanga, Weiwei Dong, and et al. One step synthesis of vertically aligned zno nanowire arrays with tunable length. *Applied Surface Science*, 256:6543–6549, 2010. 77

- [126] Kumar S, Rajaraman S, Gerhardt RA, and et al. Tin oxide nanosensor fabrication using ac dielectrophoretic manipulation of nanobelts. *Electrochim Acta*, 51:943–951, 2005. 77
- [127] Wang D, Zhu R, Zhou Zhaoying, and et al. Controlled assembly of zinc oxide nanowires using dielectrophoresis. *Appl Phys Lett*, 90:103–110, 2007. 77
- [128] Lao CS, Liu J, Gao P, and et al. ZnO nanobelt/nanowire schottky diodes formed by dielectrophoresis alignment across Au electrodes. *Nano Lett*, 6:263–266, 2006. 77
- [129] S.R. Mahmoodia, B. Raissia, E. Marzbanrad, and et al. Dielectrophoretic assembly of ZnO nanorods for gas sensing. *Procedia Chemistry*, 1:947–950, 2009. 77
- [130] Suehiro J, Nakagawa N, Hidaka S-I, and et al. Dielectrophoretic fabrication and characterization of a ZnO nanowire-based UV photosensor. *Nanotechnology*, 17:2567–2573, 2006. 77
- [131] S Roy Morrison. Semiconductor gas sensors. *Sensors and Actuators*, 2:329–341, 1982. 78, 100
- [132] J.H Anderson and G.A. Parks. The electrical conductivity of silica gel in the presence of adsorbed water. *J. Phys. Chem.*, 72:3662–3668, 1968. 79
- [133] Y. Wang, J. Yeow, and L.-Y. Chen. Synthesis of aligned zinc oxide nanorods for humidity sensing. In *3rd International conference on Sensing technology*, pages 670–673, Nov. 30–Dec. 3 2008. 79
- [134] D.W. Bahnemann, C. Jormann, and M.R. Hoffman. Preparation and characterization of quantum size zinc oxide: a detailed spectroscopic study. *Journal of Physics Chemistry*, 91:3789–3798, 1987. 79
- [135] J.L. Zhang. Electrical conduction of Ba_{0.5}Sr_{0.5}TiO₃ ceramics under d.c. voltage. *J. Mater. Sci. Lett.*, 11:294–295, 1992. 99
- [136] Y.C. Yeh and T.Y. Tseng. Humidity sensitive electrical properties of Ba_{0.5}Sr_{0.5}TiO₃ porous ceramics. *J. Mater. Sci. Lett.*, 7:766–768, 1988. 99
- [137] J.G. Fagan and V.R.W. Amarakoon. Reliability and reproducibility of ceramic sensors: Part iii. humidity sensors. *J. Mater. Sci. Lett.*, 7:766–768, 1988. 100
- [138] Y. Shimizu, M. Shimabukuro, and H. Arai. The sensing mechanism in a semiconducting humidity sensor with Pt electrodes. *J. Electrochem. Soc.*, 136:3868–3871, 1989. 100, 102

- [139] W.M. Sears. The effect of oxygen stoichiometry on the humidity sensing characteristics of bismuth iron molybdate. *Sensors and Actuators B*, 67:161–172, 2000. 100, 101
- [140] B.C. Yadav, Richa Srivatava, and C.D. Dwivedi. Synthesis and characterization of zno nanorods by the hydroxide route and their application as humidity sensors. *Synthesis and Reactivity in Inorganic, Metal-Organic, and Nano-Metal Chemistry*, 37:417–423, 2007. 101
- [141] Sheng-Po Changa, Shoou-Jinn Changa, and Chien-Yuan Lu. A zno nanowire-based humidity sensor. *Superlattices and Microstructures*, 47:772–778, 2010. 101
- [142] B.C. Yadav, Richa Srivatava, and C.D. Dwivedi. Synthesis and characterization of zno-tio₂ nanocomposite and its application as a humidity sensor. *Philosophical Magazine*, 88:1113–1124, 2008. 101
- [143] Weon-Pil Tai and Jae-Hee Oh. Humidity sensing behaviors of nanocrystalline al-doped zno thin films prepared by sol-gel process. *Journal of Materials Science: Materials in Electronics*, 13:391–394, 2002. 101
- [144] Suman Pokhrel, B. Jeyaraj, and K.S. Nagaraja. Humidity-sensing properties of $zncr_2o_4czno$ composites. *Materials Letters*, 57:3543–3548, 2003. 101
- [145] K.I. Arshak and K. Twomey. Investigation into a novel humidity sensor operating at room temperature. *Microelectronics Journal*, 33:213–220, 2002. 101
- [146] Shrikrishna Pandurangji Yawale, Sangita Shrikrishna Yawale, and Gajanan Trymbakapp Lamdhadeb. Tin oxide and zinc oxide based doped humidity sensors. *Sensor and Actuators A*, 135:388–393, 2007. 101
- [147] Yongfu Qiu and Shihe Yang. Zno nanotetrapods: Controlled vapor-phase synthesis and application for humidity sensing. *Advanced Functional Materials*, 17:1345–1352, 2007. 102
- [148] Yunxing Shu, Yongsheng Zhang, and Ke Yu. Humidity sensing properties of zinc oxide nanorod and nanobelt films. *Proceedings of the 2006 IEEE International Conference on Mechatronics and Automation*, June 25–28:Luoyang, China, 2006. 102
- [149] Weon-Pil Tai, Jun-Gyu Kima, and Jae-Hee Ohb. Humidity sensitive properties of nanostructured al-doped $zno : tio_2$ thin films. *Sensor and Actuators B*, 96:477–481, 2003. 102
- [150] Yongsheng Zhanga, Ke Yua, and Desheng Jiang. Zinc oxide nanorod and nanowire for humidity sensor. *Applied Surface Science*, 242:212–217, 2005. 102

- [151] Zvi Liron, Jeremy Greenblatt, Gad Frishman, and Netzach Gratziani. Temperature effect and chemical response of surface acoustic wave (saw) single-delay-line chemosensors. *Sensors and Actuators B*, 12:115–122, 1993. 113
- [152] Mingfang Ling and Haiguo Li. Saw temperature and humidity sensor with high resolution. *Sensors and Actuators B*, 12:53–56, 1993. 113
- [153] M. Penza and V.I. Anisimkin. Surface acoustic wave humidity sensor using polyvinyl-alcohol film. *Sensors and Actuators*, 76:162–166, 1999. 113
- [154] Yongsheng Zhang, Ke Yu, Shixi Quyang, and et al. Detection of humidity based on quartzcrystal microbalance coated with zno nanostructure films. *Physica B*, 368:94–99, 2005. 113
- [155] Xiaofeng Zhou, Jian Zhang, and Tao Jiang. Humidity detection by nanostructured zno: A wireless quartz crystal microbalance investigation. *Sensors and Actuators A*, 135:209–214, 2007. 113
- [156] Xiaofeng Zhou, Tao Jiang, Jian Zhang, and et al. A quartz tuning fork-based humidity sensor using nanocrystalline zinc oxide thin film coatings. *Proceedings of the 2006 IEEE International Conference on Information Acquisition*, pages August 20 – 23, Weihai, Shandong, China, 2006. 113